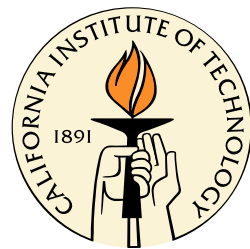


Resonant Metallic Nanostructures for Active Metamaterials and Photovoltaics

Thesis by
Imogen Mary Pryce

In Partial Fulfillment of the Requirements
for the Degree of
Doctor of Philosophy



California Institute of Technology
Pasadena, California

2011

(Defended June 7, 2011)

© 2011

Imogen Mary Pryce

All Rights Reserved

Acknowledgements

Perhaps the most naïve assumption that graduate students (myself included) make as they start their degrees is that this elusive final “thesis” document is something that has to be utterly and completely one’s own doing. In reality, a thesis is the culmination of years of work that has been motivated, challenged, funded, and/or supported by a rich cast of characters. This thesis, in particular, is a tapestry of projects, ideas, and there are many people to whom I owe thanks for their contributions.

First, I must thank Harry Atwater. His drive and passion for science convinced me to come to graduate school in the first place. Over the course of my time at Caltech, he has been a seemingly endless source of ideas and support. He has an incredible ability to always find the silver lining and I hope that one of the things that I take from graduate school is the ability to emulate this, at least partially. I must also thank Professors Konstantinos Giapis, Sossina Haile, and Axel Scherer for agreeing to serve on my thesis committee.

I have had the opportunity to work on a number of collaborative projects, which have made this thesis a much richer and more interesting body of work. I must first thank my metamaterial accomplices, Matthew Dicken and Koray Aydin. Matt taught me everything I know about semiconductor growth, how to sketch science on texwipes, and the shortest route to Peet’s. Koray has been a tremendous collaborator, supporter, and resident metamaterial guru. He has been an endless source of help with presentations, figures, and ideas. The other person to whom I owe a great deal of metamaterial thanks is Yousif Kelaita, who is the brightest and most hardworking undergrad that I know. It has been a pleasure to work with him and I can only hope that he finds an equally competent undergrad in his life as a grad student. More recently, Emily Warmann has been a great sounding board for ideas about metamaterial mechanics; she was also my frisbee buddy in the group. Raymond Weitekamp’s excitement and enthusiasm kept me in the lab making samples when I should have been working on my thesis. My adventures in plasmonic photovoltaics would not have been possible without the training of Keisuke Nakayama. He made

the most beautiful anodic alumina templates with a finesse that I was never able to completely master.

My time at Caltech would not have been the same without a number of people. Vivian Ferry is a phenomenal scientist and ally in lab. Over the past 5 years, she has edited numerous presentations and papers, given countless pep talks, and been the very best friend I could have hoped for. Her other half, David Valley, has not only been my spectroscopy go-to man, but has also fed me dinner and put up with me as a third wheel in his house on many evenings. Carrie Hofmann has also been endlessly supportive and served as my partner in crime in the office. I have also shared the office with Ryan Briggs, who never ceases to amaze me with his attention to detail and incredible work ethic. In addition to including me as a collaborator on a beautiful paper, he has provided the soundtrack to a number of late nights in the office. Luke Sweatlock was also a Watson 244 officemate and taught me about plasmonics, grad school survival, and how to most effectively blend sarcasm and science. Ken Diest, Krista Langeland, and Morgan Putnam were all amazingly helpful and welcoming when I started in the group and we have shared many birthdays and other celebrations outside of lab. Jen Dionne and Mike Kelzenberg both wrote beautiful theses that I can only hope to have modeled here. In addition to being a fantastic resource about all things in lab, Dan Turner-Evans dutifully captained our lab softball team for the past two years, bringing us all together for some out-of-lab summer fun. Outside of the Atwater group, I owe thanks to Sameer Walavalkar and Aditya Rajagopal for introducing me to Big Bertha (the etcher) and etching numerous samples for me.

There are many other people in the Atwater group who have helped make my years in graduate school more rewarding and fun. I will be forever grateful that I joined a group where people edit papers or posters for one another on a moment's notice or answer a desperate plea for moving help when the housing office says your lease is up at the end of the day. So, thank you to all of the Atwater Group that I overlapped with: Melissa Archer, Jeff Bosco, Stanley Burgos, Dennis Callahan, Chris Chen, Naomi Coronel, Davis Darvish, Mike Deceglie, Carissa Eisler, Hal Emmer, Jim Fakonas, Eyal Feigenbaum, Mike Filler, Kate Fountaine, Jonathan Grandidier,

Min Jang, Seokmin Jeon, Brendan Kayes, Seyoon Kim, Greg Kimball, Emily Kosten, Lise Lahourcade, Andrew Leenheer, Marina Leite, Henri Lezec, Manav Malhotra, Gerald Miller, Jeremy Munday, Deirdre O'Carroll, Domenico Pacifici, Peter Saeta, Matt Sheldon, Faisal Tajdar, Adele Tamboli, Katsu Tanabe, Yulia Tolstova, Rene de Waele, Robb Walters, and Sam Wilson. The group's administrative assistants - April Neidholdt, Lyra Haas, Tiffany Kimoto, and Jennifer Blankenship - have made everything run smoothly and Watson 256 has always been a place to regain a little sanity.

There are a number of other people who, in general, make sure that life at Caltech runs smoothly. Much of the fabrication and characterization of samples in this thesis would not have been possible without the tools in the KNI and I thank Guy deRose, Bophan Chhim and Melissa Melendes for training and advice. Nils Asplund was also incredibly helpful when I decided to revamp the PLD. He is an unparalleled storyteller and source of Caltech lore and perhaps before I leave I will have the courage to ask why his email is mrluckyatcaltech. I must also thank Professor George Rossman for being incredibly generous with all of the tools in his lab, in particular the FTIR microscope which I spent many hours with. I also thank Liz Boyd for the hours of work that she put into helping with FTIR measurements and training me on the equipment. Kathy Bubash has been incredibly supportive over the years as the Chemical Engineering option coordinator, helping with everything from arranging my visit as a prospective student to helping with signatures on my graduation forms. I am sure there are a number of other people at Caltech to whom I owe thanks and I apologize for missing particular names.

I would have never survived grad school without the love and encouragement of my family and friends. My parents - Wendy and Jean-Marc Soucy and David Pryce - have all been unconditionally supportive and have patiently listened to explanations of my research. My siblings - Anneka, Phil, Steve, Clarissa, and Alessandro - have kept me grounded and never let me take myself too seriously. Anneka has been an incredible cheerleader, calling and sending emails when I was the most panicked. I also thank the rest of my family that is scattered around the globe, especially my

grandad, George Ayles, who has always been my number one fan. I also feel obliged to express my gratitude to the friends I have made through ultimate frisbee in L.A. and thank them for keeping me sane when I needed an escape from lab. Last, but certainly not least, I thank Nicholas Larusso for his unwavering support and confidence in me, for making me laugh, and for letting me share the last 7 years with him.

Abstract

Electromagnetic metamaterials are composites consisting of sub-wavelength structures designed to exhibit particular responses to an incident electromagnetic wave. In general, the properties of a metamaterial are fixed at the time of fabrication by the dimensions of each unit cell and the materials used. By incorporating dynamic components to the metamaterial system, a new type of tunable design can be accessed.

This thesis describes the design and development of resonant metallic nanostructures for use in active metamaterials. We begin by examining passive systems and introduce concepts that are critical for the design of more complex, tunable structures. We show how a simple metamaterial design, a plasmonic nanoparticle array, can be used to enhance the photocurrent of an ultrathin InGaN quantum well photovoltaic cell. We then explore how more complex resonator shapes can be coupled together in a single unit cell in order to access more complex resonant behavior.

In the second half of this thesis, we use several material systems as the basis for the design of active metamaterials. We demonstrate the first tunable metamaterial at optical frequencies using vanadium dioxide, a phase transition material. We exploit this material's transition from a semiconducting to a metallic state and show how a novel fabrication scheme can be used to achieve a frequency tunable resonant response. We then abandon traditional hard and brittle substrates and develop a lithographic transfer process for adhering metallic nanostructures to highly compliant polymeric substrates. Mechanical deformation is then used to distort the resonator shapes and achieve resonant tunability of a full linewidth. This system is exploited to demonstrate interesting resonant hybridization phenomena, such as Fano resonance modulation and sets the stage for the more elusive goal of driving two resonant nanostructures into contact. Finally, we describe the use of compliant tunable metamaterials as both refractive index sensors and surface enhanced infrared absorption (SEIRA) substrates. The results highlight the promise of post-fabrication tunable compliant metamaterial sensors and the potential for integration with spectroscopic devices in remote sensing and microfluidic device applications.

Contents

List of Figures	xiii
List of Tables	xvii
List of Publications	xix
1 Introduction	1
1.1 What is a Metamaterial?	1
1.2 Properties of Natural Materials	2
1.3 Maxwell's Equations	3
1.4 Designing Artificial Material Properties	5
1.5 A Brief History of Metamaterials	8
1.6 Setting the Stage for Active Metamaterials	9
1.7 Thesis Scope	10
2 Plasmonic Enhancement of Photocurrent in an InGaN Quantum Well Solar Cell	13
2.1 Introduction	14
2.2 Experimental Design	16
2.2.1 Quantum Well Structures	16
2.2.2 Anodic Alumina Templates	17
2.3 External Quantum Efficiency Measurements	21
2.4 Current-Voltage Measurements	23

2.5	Device Physics Modeling	23
2.6	Modeling of Optical Generation Rates	25
2.7	Summary	28
3	Coupling in Metamaterials	33
3.1	Introduction	33
3.2	Experiment and Simulation Details	34
3.3	Changing Resonator Length to Introduce Asymmetry	36
3.4	Coupling Split-Ring Resonators	41
3.4.1	Distance Dependence	41
3.4.2	Uncoupled versus Coupled Resonators	42
3.4.3	Hybridization Picture for SRRs	42
3.5	Changing Resonator Shape for Extreme Asymmetry	45
3.6	Summary	47
4	Frequency Tunable Metamaterials Based on the VO_2 Phase Transition	49
4.1	Introduction	50
4.2	Vanadium Dioxide Growth	51
4.3	Unit Cell Design and Fabrication	51
4.4	Silver SRR Arrays on Planar Vanadium Dioxide Substrates	53
4.5	Silver and Vanadium Dioxide Hybrid SRRs	57
4.6	Coupled Asymmetric Hybrid SRRs	58
4.7	Summary	62
4.8	Opportunities	63
5	Compliant Optical Metamaterials	65
5.1	Introduction	66
5.2	Metamaterial Design and Fabrication	67
5.3	Basic Uncoupled Split-Ring Resonators	70
5.4	Elastic Response of Coupled Resonators	74

5.5	Inelastic Response of Coupled Resonators	76
5.6	Achieving Linewidth Tunability	80
5.6.1	Mechanical Modeling of Compliant Metamaterials	82
5.7	Sensing with Compliant Metamaterials	82
5.8	Modulating Fano Resonances with Compliant Metamaterials	85
5.9	Larger Strain and Changes in Elasticity	89
5.10	Summary	91
6	Compliant Metamaterials for Sensing	93
6.1	Introduction	93
6.2	Enhanced Local Electric Field for Metamaterial-Based Sensing	97
6.3	Refractive Index Sensing with Compliant Metamaterials	98
6.4	Compliant Metamaterials for Surface-Enhanced Spectroscopy	103
6.4.1	Static Structures for Surface-Enhanced Spectroscopy	104
6.4.2	Post-Fabrication Tuning of a Metamaterial Resonance for Surface-Enhanced Spectroscopy	109
6.5	Summary and opportunities	112
7	Summary and Outlook	115
A	Modeling Metamaterial Mechanics Using COMSOL	123
A.1	Review of Key Material Properties	124
A.2	Relevant Solid Mechanics Theory	125
A.2.1	The Coordinate Systems of Continuum Mechanics	125
A.2.2	Governing Equations	125
A.3	Steps for Creating a COMSOL Model	126
B	Fabrication of Metal Nanoparticle Arrays Using Anodic Alumina Templates	131
	Bibliography	134

List of Figures

1.1	The material landscape.	4
1.2	Basic split-ring resonator structure.	8
1.3	A brief history of metamaterials.	9
2.1	Tunable band gap of $\text{In}_x\text{Ga}_{1-x}\text{N}$ alloys.	16
2.2	Device design.	18
2.3	Anodic alumina template masks and nanoparticles.	19
2.4	Fabrication process steps.	20
2.5	External quantum efficiency.	22
2.6	Current-voltage measurements.	24
2.7	AFORS-Het modeling of the device physics.	26
2.8	Simulation points for calculating generation rates.	27
2.9	Electron generation rates.	29
2.10	Electron generation rates in InGaN quantum well.	30
3.1	Coupled asymmetric split-ring resonator unit cell.	36
3.2	SEM micrographs of various resonator designs.	37
3.3	Experimental and simulated transmission spectra for coupled SRR systems.	39
3.4	Transmission spectra for coupled SRR systems with varying coupling distance.	43
3.5	Experimental and simulated transmission spectra for coupled and uncoupled SRR systems.	44

3.6	Hybridization picture for coupled SRR systems.	46
3.7	Resonant response for SRR-nanowire system.	48
4.1	Vanadium dioxide characterization.	52
4.2	Hybrid split-ring resonator metamaterials based on vanadium oxide. .	54
4.3	Ag SRR metamaterial arrays on planar VO ₂	56
4.4	Active self-aligned hybrid-SRR arrays.	59
4.5	Coupled asymmetric Ag/VO ₂ hybrid-SRR metamaterials.	61
4.6	Vanadium oxide growth on Si.	64
5.1	Fabrication sequence for compliant metamaterials.	69
5.2	Custom-built stage.	70
5.3	Testing large SRRs on highly strained substrate.	71
5.4	Metamaterial structures.	72
5.5	Strain in compliant metamaterials.	73
5.6	Transmittance data for bare PDMS films.	76
5.7	Reflectance data for coupled resonators.	77
5.8	Reflectance data for coupled resonators.	78
5.9	Measuring gap sizes for each level of strain.	79
5.10	Figure of merit and strain density maps for each resonator.	81
5.11	Metamaterial-based sensing.	83
5.12	Reflectance data for coupled resonator pair.	86
5.13	Modulating the Fano resonance.	88
5.14	Loading behavior of compliant metamaterials.	90
6.1	Representative coupled and uncoupled SRR arrays	96
6.2	FTIR spectra of coupled and uncoupled SRR arrays in different index-matching fluids	99
6.3	Figure of merit values for various resonators	102
6.4	Sensitivity values for arrays of SRRs on PDMS	104

6.5	FTIR reflection spectra for arrays of SRRs on Si functionalized with <i>p</i> MA	105
6.6	SEIRA enhancement for arrays of SRRs on Si	106
6.7	FTIR reflection spectra for arrays of SRRs on PDMS	109
6.8	FTIR reflection spectra for tunable arrays of SRRs on PDMS	110
6.9	Tandem refractive index sensing and vibrational mode spectroscopy .	113
7.1	SRR with resonance at telecommunication frequency	117
7.2	Effect of air channel in PDMS.	119
7.3	Representative SRR Arrays	121
A.1	Defining geometry and material properties in COMSOL.	128
A.2	Defining mesh parameters in COMSOL.	129
A.3	Plotting results in COMSOL.	130

List of Tables

2.1	Solar cell characteristics from AFORS-Het calculations	25
6.1	Sensitivity and figure-of-merit values for different sizes of coupled and uncoupled resonators	103
6.2	IR Peak Assignments of <i>p</i> MA	107
B.1	Anodization conditions for various operating voltages	132

List of Publications

Portions of this thesis have been drawn from the following publications:

Compliant metamaterials for resonantly enhanced infrared absorption spectroscopy and refractive index sensing. I. M. Pryce, Y. A. Kelaita, K. Aydin, and H. A. Atwater, in preparation (2011).

Characterization of the Tunable Response of Highly Strained Compliant Optical Metamaterials. I. M. Pryce*, K. Aydin*, Y. A. Kelaita, R. M. Briggs, and H. A. Atwater, *Philosophical Transactions A*, accepted (2011).

Highly strained compliant optical metamaterials with large frequency tunability. I. M. Pryce*, K. Aydin*, Y. A. Kelaita, R. M. Briggs, and H. A. Atwater, *Nano Letters* 10, 4222 - 4227 (2010).

Symmetry breaking and strong coupling in planar optical metamaterials. K. Aydin, I. M. Pryce, and H. A. Atwater, *Optics Express* 18, 13407 - 13417 (2010).

Compact silicon photonic waveguide modulator based on the vanadium dioxide metal-insulator phase transition. R. M. Briggs, I. M. Pryce, and H. A. Atwater, *Optics Express* 18, 11192 - 11201 (2010).

Plasmonic nanoparticle enhanced photocurrent in GaN/InGaN/GaN quantum well solar cells. I. M. Pryce, D. D. Koleske, A. J. Fischer, and H. A. Atwater, *Applied Physics Letters* 96, 153501 (2010).

Frequency tunable near-infrared metamaterials based on VO₂ phase transition. M. J. Dicken*, K. Aydin*, I. M. Pryce*, L. A. Sweatlock, E. M. Boyd, S. Walavalkar, J. Ma, and H. A. Atwater, *Optics Express* 17, 18330 - 18339 (2009).

Chapter 1

Introduction

1.1 What is a Metamaterial?

Natural materials are made up of individual atoms and molecules separated by distances on the order of angstroms. When visible light interacts with natural materials, standard processes such as reflection, absorption, and transmission follow expected behavior, as the wavelength of visible light is several times larger than the constituent atoms and molecules. At an elementary level, reflection, absorption, and transmission are determined by the characteristic length of the unit cell of the atom. Metamaterials are artificially created structures where we design the unit cell length to our own specifications. In designing metamaterials, we carefully engineer a periodic array of unit cells to create an artificially structured composite material. Metamaterials free us from the constraints of naturally occurring materials and allow for full control over light flow through the design of artificial materials. These unit cells can be made up of constituent elements with periodicities ranging from tens of nanometers to millimeters depending on the target operating frequency and thus are much larger than the atomic or molecular scale features that are common in natural materials. Careful design of each unit cell and the periodicity of a metamaterial enables a wide variety of new material properties [1, 2, 3].

The ability to decouple the optical properties of an ensemble through careful assembly of its constituents leads to a wide variety of new device designs and applications. For optoelectronics and miniaturization of optical components, a number of groups have demonstrated novel types of optical modulators and filters [4, 5, 6, 7, 8, 9]. Negative refractive index materials could provide a route for the design of perfect

lenses eliminating the limits to resolution by diffraction [10, 11]. More recently, the ability to create optical cloaks has also attracted a significant amount of attention [12, 13]. This has been achieved at microwave frequencies using transformation optics, a particular branch of metamaterial research, and relies not on negative index materials but rather on the ability to individually engineer the optical properties of each unit cell across a surface [14, 15].

While metamaterials may be designed to modify numerous properties, we will focus on electromagnetic metamaterials that affect the properties of the incident electromagnetic waves. In particular, subwavelength metallic elements support sharp resonances, and we design composites based on metallic structures to tune the response of incident light. In order to more precisely understand what metamaterials are and how to design them, we will first consider the general optical properties that define all materials.

1.2 Properties of Natural Materials

One way that we can define and understand materials, in an electromagnetic sense, is based on their constitutive properties: permittivity, ϵ , and permeability, μ [16, 17]. These properties describe how the material interacts with and affects incident light. Permittivity is a measure of how the applied electric field interacts with the medium and permeability measures the response of a material to an applied magnetic field. In Fig. 1.1 we define the “material landscape” in terms of these electromagnetic properties, and we can group materials based on the sign of their ϵ and μ . The refractive index is closely related to both ϵ and μ , $n = \pm\sqrt{\epsilon\mu}$, and the signs of these properties determine many of the unusual responses that can be engineered. Most natural materials have positive ϵ and μ and thus fall into quadrant I of this graph. Materials with negative ϵ but positive μ fall into quadrant II and tend to be either metals, heavily doped semiconductors, or ferroelectric materials that can have negative values of ϵ below the plasma frequency. The third quadrant is where we find negative index materials, with both negative ϵ and negative μ . The idea of

a negative index material was first outlined by Veselago in 1968 [18]. These types of materials have been referred to conceptually as left-handed materials (LHM) as one of the effects of negative ϵ and μ is a reversal of the direction of propagation of the incident wave, thus breaking the right-hand rule of elementary physics. The last quadrant of this material landscape is where ϵ is positive, but μ is negative. There are also very few natural materials in this regime, although some ferrite materials exhibit these properties at microwave frequencies. Much of the exciting research in metamaterials and plasmonics is the extraordinary nature of the structures that can be designed when we ignore the constraints on ϵ and μ imposed by naturally occurring materials.

1.3 Maxwell's Equations

Before we begin to understand how to engineer particular designs with varying ϵ and μ , we must first develop a better understanding of how light interacts with a material. We first consider a monochromatic plane wave incident on a surface.

$$\vec{E}(\omega, \vec{k}) = \vec{E}_0 \exp(i\vec{k} \cdot \vec{r} - i\omega \cdot t) \quad (1.1a)$$

$$\vec{H}(\omega, \vec{k}) = \vec{H}_0 \exp(i\vec{k} \cdot \vec{r} - i\omega \cdot t) \quad (1.1b)$$

\vec{E} is the electric component of the plane wave, \vec{H} is the magnetic component of the plane wave, ω is the angular frequency, and \vec{k} is the wave vector. We can start with Maxwell's equations [17].

$$\nabla \cdot \vec{B} = 0, \nabla \times \vec{E} = -\frac{\partial \vec{B}}{\partial t} \quad (1.2a)$$

$$\nabla \cdot \vec{D} = \rho, \nabla \times \vec{H} = \vec{j} + \frac{\partial \vec{D}}{\partial t} \quad (1.2b)$$

\vec{B} is the magnetic flux density, \vec{D} is the electric flux density, ρ is the charge density, and \vec{j} is the current density.

Constitutive equations relate the electric and magnetic flux densities to the electric

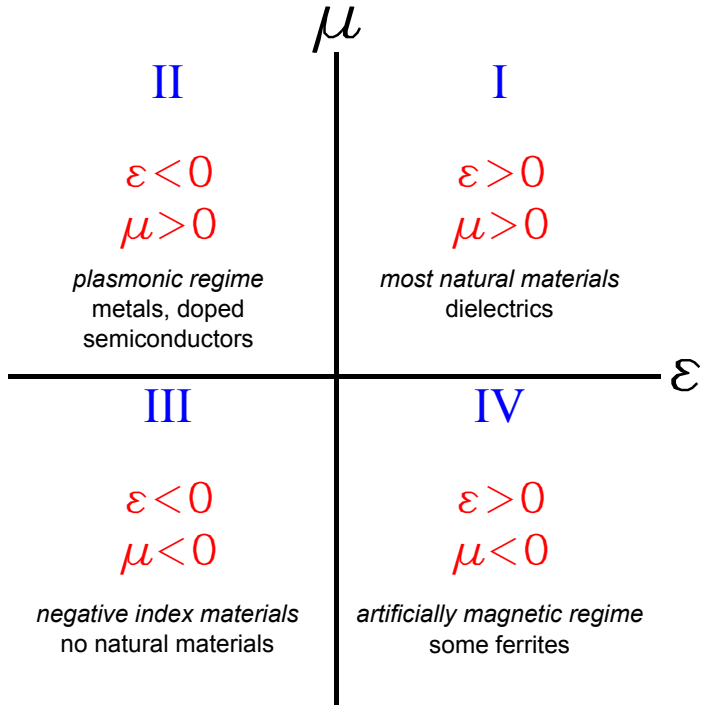


Figure 1.1. All materials can be classified and understood based on their permittivity, ϵ , and permeability, μ . Here materials are divided into four material “quadrants”: (I) most natural materials, where ϵ and μ are both positive; (II) the plasmonic regime, where ϵ is negative but μ is positive; (III) negative index materials, where both properties are negative; and (IV) the artificial magnetism regime, where ϵ is positive but μ is negative.

and magnetic fields.

$$\begin{cases} \vec{D} = \epsilon \vec{E} = \epsilon_0 \epsilon_r \vec{E} \\ \vec{B} = \mu \vec{H} = \mu_0 \mu_r \vec{E} \end{cases} \quad (1.3)$$

Here, ϵ_0 is the permittivity in vacuum, μ_0 is the permeability in vacuum, ϵ_r is the permittivity of a medium, and μ_r is the permeability of a medium.

In the absence of free charges (ρ) and currents (\vec{j}), we can simplify these equations.

$$\begin{cases} \vec{k} \times \vec{E} = \mu \omega \vec{H} \\ \vec{k} \times \vec{H} = -\epsilon \omega \vec{E} \end{cases} \quad (1.4)$$

In this set of equations, the permittivity can be expanded in terms of the complex dielectric function of a material, i.e. $\epsilon = \epsilon_1 + i\epsilon_2$. This is the form most commonly used with Maxwell's equations, however a more physical representation is in terms of the complex index of refraction, $\tilde{n} = n + i\kappa$. Here, n is the ratio of the speed of light in vacuum to the speed of light in the material, κ represents the extinction coefficient of light in the material. These properties are related (equation (1.5)) and both formalisms are used throughout this thesis.

$$\epsilon_1 = n^2 - \kappa^2 \quad (1.5a)$$

$$\epsilon_2 = 2n\kappa \quad (1.5b)$$

$$n = \sqrt{\frac{\epsilon}{2} + \frac{1}{2}\sqrt{\epsilon_1^2 + \epsilon_2^2}} \quad (1.5c)$$

$$\kappa = \frac{\epsilon_2}{2n} \quad (1.5d)$$

1.4 Designing Artificial Material Properties

Veselago's work remained somewhat unexplored until about a decade ago when Pendry et al. first proposed using artificial materials as an approach to open up the material landscape of Fig. 1.1 [19, 20]. It is here that we begin our discussion of metamaterials and describe an approach to design structures with particular values of ϵ_r and μ_r .

The permittivity and permeability can be determined using classical electromagnetic models of the optical microscopic structure. One of the most prevalent models in both plasmonics and metamaterials research is the Drude-Lorentz model, where carriers are treated as damped harmonic oscillators driven by incident light [17]. The symmetry of electromagnetic waves means that the permittivity and permeability follow similar formulae.

$$\begin{cases} \epsilon_r(\omega) = 1 - \frac{\omega_{p,e}^2}{\omega^2 - \omega_{0,e}^2 + i\gamma_e\omega} \\ \mu_r(\omega) = 1 - \frac{\omega_{p,m}^2}{\omega^2 - \omega_{0,m}^2 + i\gamma_m\omega} \end{cases} \quad (1.6)$$

Here, γ is the damping coefficient that describes any loss to the material, ω_0 is the resonant frequency, and ω_p is the plasma frequency. In this set of equations, e and m represent the electric and magnetic response of the material. For naturally occurring materials this imposes certain restrictions. For example, in the optical regime $\mu = 1$ for all natural materials. With artificially constructed metamaterials, where the constituents are subwavelength in size, the incident electromagnetic wave cannot sense the individual elements, but instead the material can be described by effective material parameters, $\epsilon_{r,eff}$ and $\mu_{r,eff}$. Using careful design, these values can be controlled at the macroscopic level.

In this thesis we focus on the artificial magnetic response that can be induced in a metamaterial. Although there are other designs that could be exploited, we concentrate on the split-ring resonator (SRR) as a basic element capable of achieving strong artificial magnetism. We describe these resonators using equivalent circuit theory, where a basic SRR is a small LC circuit with a natural resonant frequency of $\omega_0 = \sqrt{1/LC}$. Here, L is effective inductance and C is the effective capacitance of the structure. Returning to the mathematical description outlined in the Drude-Lorentz model (equation (1.6)), we notice that for a lossless material (where $\gamma = 0$), when the frequency of the incident wave equals the natural resonance, ω_0 , there is a dramatic change in the value of μ_r . Incident light at a frequency near ω_0 effectively drives a circulating current through the resonator, inducing a strong magnetic moment. We

follow the derivation for $\mu_{r,eff}$ of a basic SRR as outlined originally by Pendry et al. [3, 19] with the relevant dimensions shown schematically in Fig. 1.2, although here we take capacitance, C , to be the charge built up between the two resonators.

$$C = \frac{\epsilon_0}{d} = \frac{1}{dc^2\mu_0} \quad (1.7)$$

This leads to the following expression for $\mu_{r,eff}$.

$$\mu_{r,eff}(\omega) = 1 - \frac{F\omega^2}{\omega^2 - \omega_0^2 + i\Gamma\omega} \quad (1.8)$$

Here, F is the fractional coverage of the cell by each SRR.

$$F = \frac{\pi r^2}{a^2} \quad (1.9)$$

ω_0 is the resonant frequency.

$$\omega_0 = \sqrt{\frac{3dc^2}{\pi^2 r^3}} \quad (1.10)$$

Γ is the damping term.

$$\Gamma = \frac{2}{r\sigma\mu_0} \quad (1.11)$$

In this expression, σ is the conductivity of the metal. As an example, using dimensions that are relevant to the work in this thesis, for a split-ring resonator with dimensions $a = 1 \text{ }\mu\text{m}$, $r = 0.25 \text{ }\mu\text{m}$ and $d = 0.025 \text{ }\mu\text{m}$, we calculate a resonant frequency ($f_0 = \omega_0/2\pi$) of about 33 THz. This corresponds to a free space wavelength of 9 μm , which is about an order of magnitude larger than the lattice spacing, a , ensuring that the effective medium approximation holds for this system.

Although it is possible to derive ϵ_r and μ_r from the transmission and reflection properties of a system, in this thesis we report primarily transmittance and reflectance as determined from spectroscopic measurements or via simulation. We note that the particular values of ϵ_r and μ_r would change drastically at the resonance of the particular system, but are otherwise somewhat comparable to the average bulk properties of the composite. Thus we find that it is more instructive to explore how the resonance

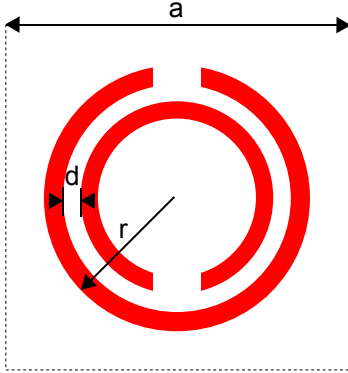


Figure 1.2. Original split-ring resonator design proposed by Pendry et al. with dimensions labeled. The red lines are the metallic resonators and the dotted black line indicates the edge of the unit cell.

of a system changes as opposed to determining the specific values of permittivity and permeability from the reflection and transmission coefficients.

1.5 A Brief History of Metamaterials

It is Veselago's seductive promise of negative index materials at optical frequencies that has driven a significant amount of work in the metamaterial field. Over the last decade the main drive in metamaterials research was to push the resonance of artificial materials to higher and higher frequencies with the ultimate goal of creating materials in the elusive visible portion of the spectrum [1, 4, 21, 22, 23, 24, 25]. It is a happy coincidence that this drive was mirrored by significant advances in nanofabrication tools. These tools made it possible not only to design but also to create and test structures with resonant properties from the microwave through the near IR. In 2007, Soukoulis et al. published an article describing how the resonant response of metamaterials had been pushed from microwave, where the unit cell is on the order of millimeters, to visible wavelengths, where to be subwavelength metamaterial unit cells had to be on the order of 100 nm in size (see Fig. 1.3) [23]. The drive to visible wavelengths, however, revealed the size limitation of the original split-ring resonator design. This limitation is a result of the fact that metals do not operate

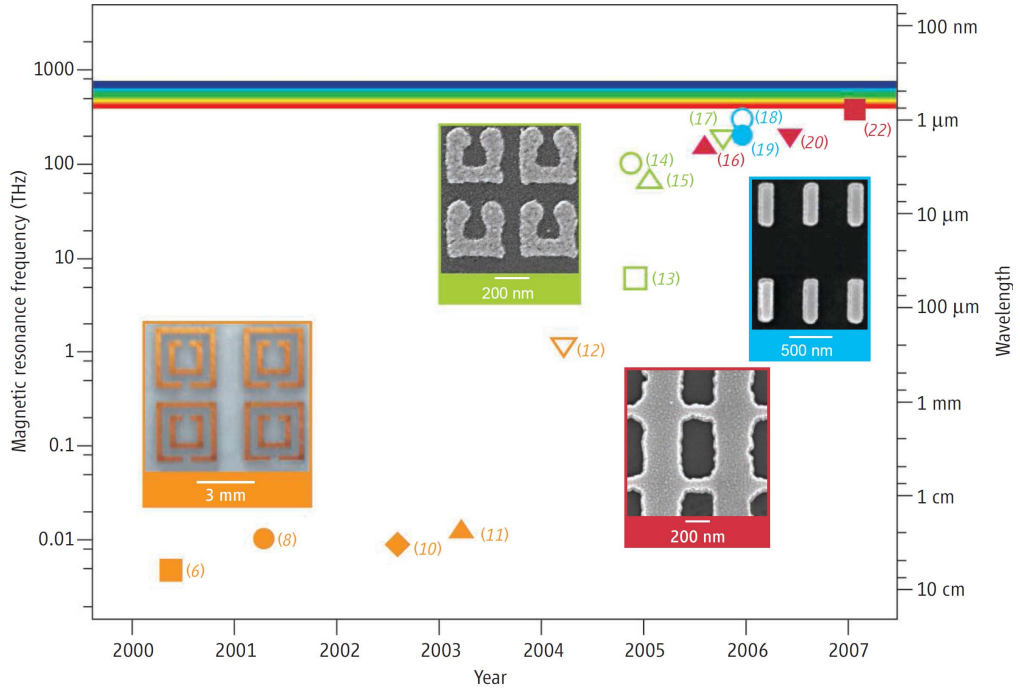


Figure 1.3. A brief graphical view of the history of metamaterials research [23]. The solid symbols indicate $n < 0$; the open symbols denote $\mu < 0$. The data in orange indicate structures based on double SRRs, the green data are for single SRRs, the blue data represent nanorod pairs, and the red data are for “fishnet” structures.

as perfect conductors in the visible regime. This prompted a shift from SRR-based metamaterials to cut wire pairs [26, 27, 28] to fishnet structures [1, 24, 29, 30, 31].

1.6 Setting the Stage for Active Metamaterials

In the mad dash to be the first research group to produce a metamaterial at optical frequency, researchers have largely ignored a more useful class of metamaterials designed with an actively controllable resonant response. The first frequency agile metamaterial was demonstrated in 2006 using patterned split-ring resonators on a heavily doped GaAs layer [32]. By contacting each of the resonators in series, an electrical bias could be used to induce carrier depletion from the split gap region resulting

in a bimodal response where the resonance was either present or not. In 2008, the same group showed how optical pumping could induce a change in path length of a particular resonator to dynamically tune the resonant response [33]. These two examples set the stage for active metamaterial work and illustrate that we can modulate both the amplitude and the frequency of the resonant response.

These active metamaterial examples have resonances in the terahertz, but their designs are not scalable to higher frequencies. The main focus of this thesis is to develop metamaterials with frequency tunability in the near-IR to mid-IR spectrum with applications in integrated optical components and telecommunications.

1.7 Thesis Scope

This thesis describes the design and development of resonant metallic nanostructures for use in active metamaterials. The first part of the thesis analyzes passive systems and includes some of the concepts that will be critical for developing tunable, dynamic metamaterial components. In Chapter 2, we demonstrate how the simplest type of metamaterial, an array of nanoparticles, can be used to enhance the photocurrent in a photovoltaic cell. We use a single indium gallium nitride quantum well as a test system and investigate the physics that describes nanoparticle coupling. We report experimental results detailing how the photocurrent is enhanced for different emitter layer thicknesses. We also include in this chapter device physics modeling that outlines how the nanoparticle array impacts the device performance and analyze the optical properties of the cell via full-field electromagnetic simulation using the finite difference time domain (FDTD) method. In Chapter 3, we explore how resonators can be coupled together to access more complex resonant behavior than is possible with single uncoupled SRRs. Through this work, we develop a number of key ideas, including how to vary the coupling distance such that the resonance shifts.

The second part of this thesis examines several different approaches to active metamaterial design and we outline some of the possible applications of these materials. In Chapter 4, we describe the first demonstration of frequency tunable metamaterials

at optical frequencies using vanadium dioxide, a material that changes phase at 70°C. We exploit this phase transition to develop materials with a tunable response, investigating both single and coupled resonators. We show how a novel fabrication scheme can be used to shift the tunability from a bimodal, amplitude modulating state to a frequency-tunable resonant response. We report both experimental and simulated data for these structures.

In Chapter 5, we explore how the frequency response can be tuned even more significantly by adhering metallic nanostructures to a compliant substrate. We describe the hard/soft nanolithographic transfer process that we developed to transfer resonators to polydimethylsiloxane (PDMS) and demonstrate the fidelity of this process. We report experimental and simulated results for highly strained metamaterials and show how their large degree of tunability can be exploited to demonstrate interesting resonant hybridization phenomena, such as Fano resonance modulation. In addition to full field electromagnetic calculations, we use finite element method (FEM) modeling of the mechanics of compliant metamaterials to determine the limits to plastic and elastic deformation. We also explore the effects of strain cycling on the metamaterial structures and discuss possible applications of this deformation.

In Chapter 6, we demonstrate how compliant tunable metamaterials are capable of both refractive index sensing and surface-enhanced infrared absorption (SEIRA). For SRR-based metamaterials, we can design sensors with high sensitivity values and large figures of merit. The tunability of these structures through the infrared also makes them well suited for detection of the absorption signal of vibrational modes throughout the “molecular fingerprinting”. We describe experimental and simulated results for surface-enhanced spectroscopy using both active and passive structures. The results highlight the promise of post-fabrication tunable compliant metamaterial sensors and the potential for integration with spectroscopic devices in remote sensing and microfluidic device applications.

Chapter 2

Plasmonic Enhancement of Photocurrent in an InGaN Quantum Well Solar Cell

In Chapter 1, we defined metamaterials as periodic arrangements of resonant nanostructures. A key feature of a metamaterial is the ability to change the way that light interacts with a material. We can change the way that incident light scatters into a material using arrays of metallic nanoparticles. By changing the size and shape of these particles, we can effect their resonant and scattering properties. In this sense, plasmonic nanoparticle arrays are the simplest metamaterials that we can design and we use this work as a segue for building more complex metamaterial structures in subsequent chapters.

In solar cells, thick layers are required for optical absorption, but thin layers are better for improved carrier collection. This suggests that the active region of a solar cell should be thinned as much as possible. Standard light-trapping techniques, however, are not scalable down to cells that are a fraction of a wavelength thick. In this work, we use plasmonic nanoparticle scattering as a way to guide and concentrate the light into small dimensions.

We use indium gallium nitride as the material system of choice because the band gap tunability and the material properties of InGaN alloys make them ideal candidates for photovoltaic applications. Plaguing this material system, however, is the large defect density of trap states that can reduce collection efficiency in the cell and the phase separation of InN that occurs at high In concentrations. Exploiting the benefits of nanoparticle scatters could enable much thinner active regions and possibly the use of quantum wells as the active region of a photovoltaic cell, as they can support a

much higher level of lattice mismatch compared to bulk material and have already been successfully employed in light emitting diodes.

In this chapter, we demonstrate enhanced external quantum efficiency and current-voltage characteristics due to scattering by 100 nm silver nanoparticles in a single 2.5 nm thick InGaN quantum well photovoltaic device. Nanoparticle arrays were fabricated on the surface of the device using an anodic alumina template masking process. The Ag nanoparticles increase light scattering, light-trapping, and carrier collection in the III-N semiconductor layers leading to enhancement of the external quantum efficiency by up to 54%. Additionally, the short-circuit current in cells with 200 nm p-GaN emitter regions is increased by 6% under AM 1.5 illumination. AFORS-Het simulation software results are used to predict cell performance and optimize emitter layer thickness.

2.1 Introduction

Plasmonic nanoparticle scattering offers a unique way to circumvent the inherent trade-off between absorption and carrier collection in the design of solar cells. Optically thick cells can absorb all nonreflected incident light, but incomplete carrier collection can limit cell internal quantum efficiency. The thickness reduction of high efficiency, low cost, thin film solar cells is limited by the absorption properties of the active layer. Increasing cell efficiency and reducing the material thickness both motivate investigating ways of increasing the light absorption in photovoltaic materials. Plasmonic nanostructures have been studied on both optically thick and thin semiconductor films [34, 35, 36, 37, 38, 39, 40, 41]. Conventional solar cells often incorporate surface texturing to increase the optical path length of light within the cell, but these structures are too large to be used in thin film cells [42]. Metal nanoparticles can serve a similar purpose in very thin cells, where surface texturing is not possible, due to their large scattering cross sections and enhanced local fields [16]. The resonant effect that results in scattering from metallic nanoparticles is primarily due to the induced dipole moment, \mathbf{p} , that is driven by the applied field, \mathbf{E}_0 according

to equation (2.1).

$$\mathbf{p} = \epsilon_m \alpha \mathbf{E}_0 \quad (2.1)$$

Here α is the dipole polarizability which is proportional to the radius of the particle, R , the permittivity of the surrounding medium, ϵ , and the permittivity of the metal, ϵ_m (equation (2.2)).

$$\alpha = 4\pi R^3 \frac{\epsilon - \epsilon_m}{\epsilon + 2\epsilon_m}. \quad (2.2)$$

The polarizability directly affects the absorption and scattering cross sections, C_{abs} and C_{scat} , respectively (equation (2.3a)).

$$C_{abs} = k \Im[\alpha] \quad (2.3a)$$

$$C_{scat} = \frac{k^4}{6\pi} |\alpha|^2 \quad (2.3b)$$

α is resonantly enhanced when $\epsilon(\omega) \cong -2\epsilon_m$. This results in large scattering cross sections that enhance local electric fields and increase the path length of the incident light. For thicker cells, the increase in optical path length translates to an increase in effective optical thickness of the active region. In the case of thin film cells, there is an additional benefit: the metal nanostructures can couple incident light into guided modes that propagate through the active region, thereby increasing absorption and photocurrent. Here, we demonstrate that nanoparticle light scattering can be tailored to enhance absorption in optically thin InGaN single quantum well (QW)-based photovoltaic devices, but the thick GaN buffer layer prevents testing absorption via incoupling to waveguide modes in the active region.

Recent breakthroughs in the ability to grow higher quality InGaN alloys have made them materials of particular interest for photovoltaic applications. The InGaN material system can be compositionally tuned across the visible portion of the solar spectrum, maintaining a direct band gap throughout the composition gradient (see Fig. 2.1) [43]. InGaN materials also exhibit superior radiation resistance making them suitable for space-based photovoltaics [44]. Several preliminary InGaN-based

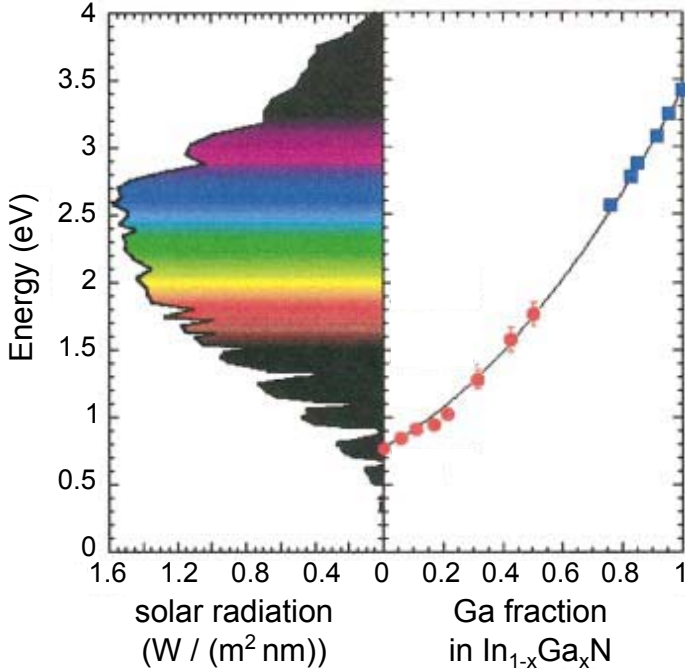


Figure 2.1. The band gap energy of $\text{In}_{1-x}\text{Ga}_x\text{N}$ can be tuned across the entire solar spectrum. The points are experimentally measured band gaps. (*Adapted from a figure in reference [44]*).

device designs have been demonstrated [45, 46, 47]; however, these devices have been limited by film quality due to strain and phase separation. QW-based architectures are relatively tolerant to lattice mismatch and have been used extensively in light emitting diodes (LEDs) and laser diodes at wavelengths through the visible spectrum. In this work we show that the absorption in a QW-based device can be enhanced, enabling the development of photovoltaic devices from material previously suitable only for LEDs.

2.2 Experimental Design

2.2.1 Quantum Well Structures

The GaN/InGaN/GaN structures employed here were initially designed as LEDs, but also serve here as prototypical extremely thin photovoltaic devices for probing

enhanced quantum well absorption. Figure 2.2A shows a schematic of the QW samples grown via metallorganic chemical vapor deposition. A 2 - 3 μm n-GaN buffer layer (n-doped $[\text{Si}] = 2 - 3 \times 10^{18} \text{ cm}^{-3}$) is first deposited on a sapphire substrate followed by a 2.5 nm InGaN QW with a band gap of 2.8 eV. A 12 nm p-AlGaN electron blocking layer is deposited on top of the QW, followed by a p-GaN emitter layer (p-doped $[\text{Mg}] = 3 - 5 \times 10^{17} \text{ cm}^{-3}$). A $7.5 \times 10^{-4} \text{ cm}^2$ window is etched into each device via Ar^+ ion milling of the top p-contact to facilitate nanoparticle deposition (Fig. 2.2B). The p-GaN deposited thickness is 200 nm, however, this is varied by changing the duration of the etch. Two samples of different emitter layer thickness (d in Fig. 2.2A) 50 and 200 nm, were studied.

2.2.2 Anodic Alumina Templates

We deposit Ag nanoparticles using a porous anodic aluminum oxide (AAO) masking technique [41]. This has the advantage of being inexpensive and provides control over size, height, and spacing of the nanoparticles. Figure 2.3 shows how the anodization voltage can be varied to change the properties of the nanoparticles. As the voltage is increased, the interpore spacing is increased. For our purposes, we wanted nanoparticles that were spaced close enough together to affect the entire cell, but far enough apart to prevent significant shadowing. We also wanted nanoparticles that were large enough to avoid being lossy, i.e., having large absorption in the nanoparticle itself. Al sheets (4N) are anodized in a two-step process at 80 V in a mixture of 0.3 M oxalic acid and 0.3 M malonic acid to yield interpore spacing of 200 nm. The Al is removed using an iodine-methanol solution leaving a porous aluminum oxide sheet. The mask template is etched in 5% dilute phosphoric acid for 65 min to yield pore diameters of 100 nm. While the anodization voltage sets the interpore spacing, the etch time sets the size of the nanoparticles. The template is placed in direct contact with the device window and used as a mask for thermal evaporation of Ag. The resulting nanoparticles are approximately 100 nm in diameter and height, with 200 nm spacing. Figure 2.2C shows a scanning electron microscopy (SEM) image of a representative nanoparticle array. Figure 2.3 shows arrays of nanoparticles made using

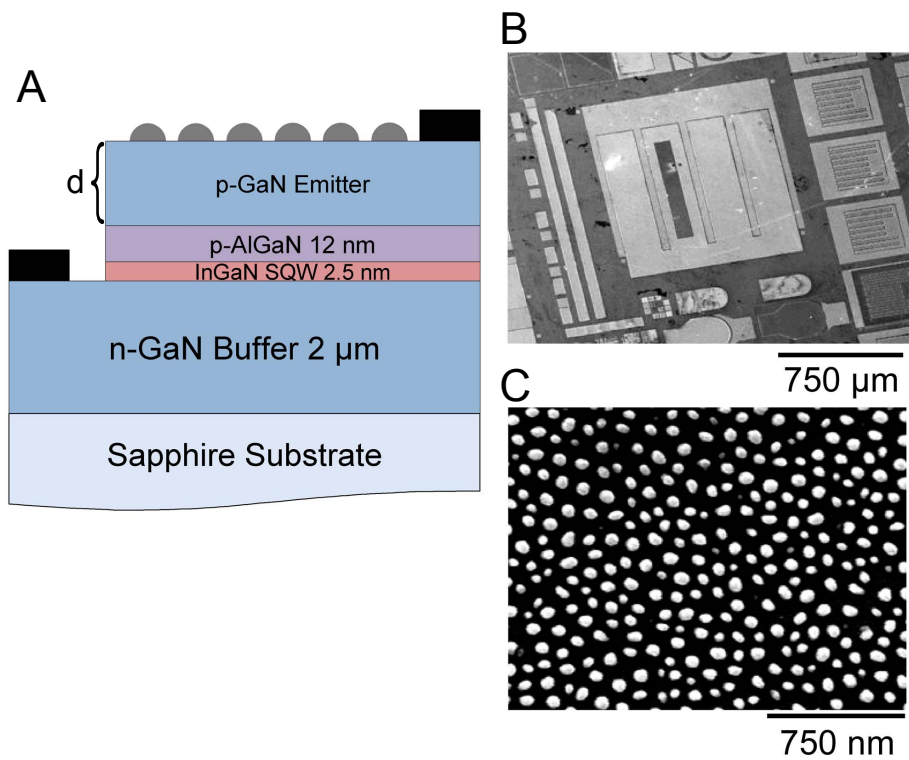


Figure 2.2. A. A schematic of the device structure with Ag nanoparticles is shown. Structures with emitter thicknesses, d , of 50 nm and 200 nm were investigated. B. An SEM image of the actual device shows the window etched into the top contact for nanoparticle deposition. C. A representative array of Ag nanoparticles is shown. They are spaced 200 nm apart, with 100 nm diameter and height, and deposited onto the QW cell via thermal evaporation through an anodic aluminum oxide template.

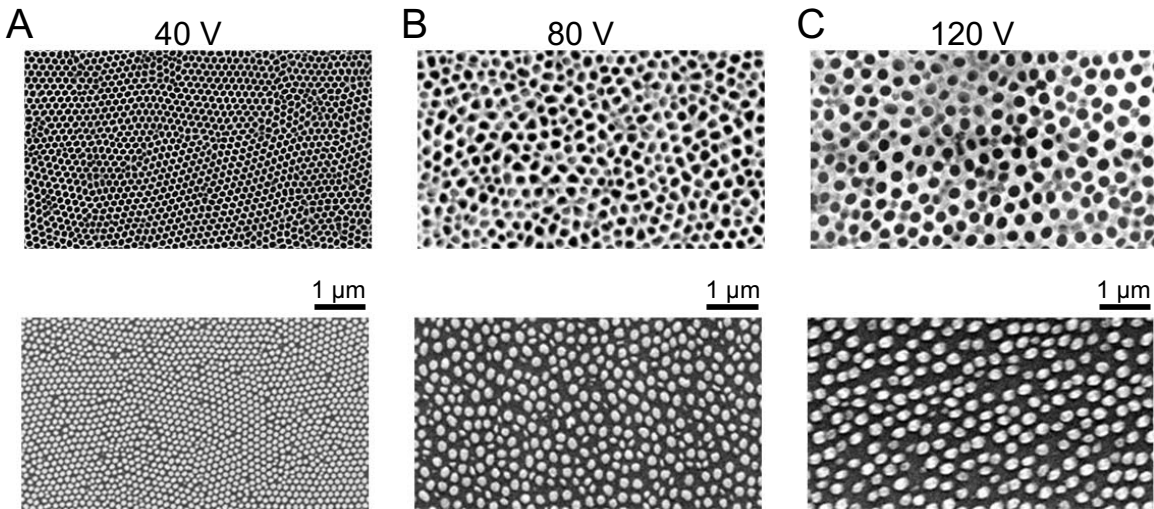


Figure 2.3. Masks made at different anodization voltages ranging from 40 V (A) to 120 V (C). The anodic alumina templates are used as thermal evaporation masks for Ag deposition. Below the image of each mask, the corresponding evaporated nanoparticle array is shown. (*Images courtesy K. Nakayama*)

masks of varying voltage. As the anodization voltage increases, the size of the pores and distance between pores increases. For lower voltages, the interpore distance is small resulting in somewhat regular arrangements of nanoparticles. This regularity in pattern is lost for higher anodization voltages and the irregularity in periodicity in Fig. 2.2C is characteristic of a deposition at 80 V. Detailed instructions for the AAO templating process are outlined in Appendix B.

Figure 2.4 shows the process steps for preparing the sample for external quantum efficiency and photocurrent measurements. We spun photoresist on the cells and defined a window lithographically. We etched through the p-side contacts (300 nm Au/50 nm Pt) as described previously with an Ar+ plasma, varying the length of this etch to change the thickness of the buffer layer. We then redefined the device window and used the AAO template as a mechanical evaporation mask. The metal was evaporated into the pores of the template. The template was then removed and the final device characteristics were measured. Control cells were also measured and underwent the same processing steps but without nanoparticle deposition.

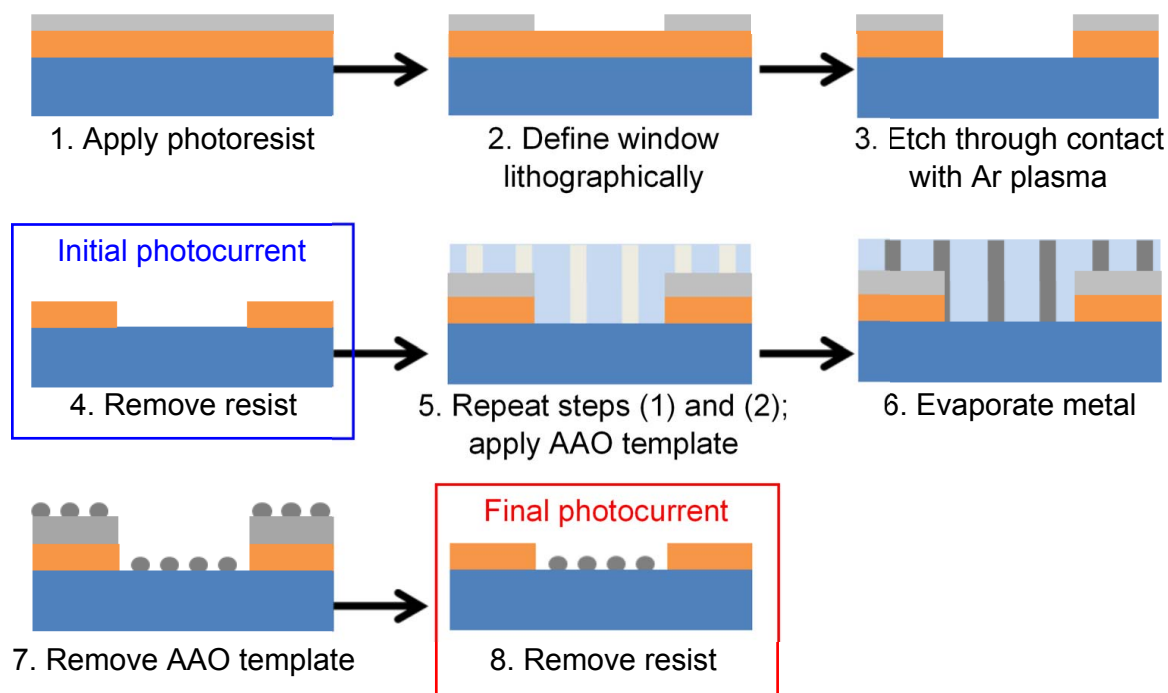


Figure 2.4. This schematic shows the process steps associated with preparing a cell for photocurrent measurements. The steps associated with the initial and final photocurrent measurements are indicated.

2.3 External Quantum Efficiency Measurements

In a solar cell, photons with energy equal to or greater than the band gap of the material can generate electron-hole pairs, although excess photon energy will be lost in the material to heat. Lower energy photons will pass directly through the material and not be absorbed. Thus, the band gap of a material dictates which portion of the solar spectrum will be usable. External quantum efficiency (EQE) is the ratio of carriers collected to the number of photons incident on the cell and these measurements provide an understanding of which photons are contributing to the photocurrent. Here, we use EQE measurements to determine where the photons are being absorbed in the photovoltaic cell as the band gaps of the GaN and InGaN regions are different.

External quantum efficiency (EQE) measurements are used to quantify how the absorption varies spectrally for devices coated with nanoparticle arrays. Figure 2.5 shows spectral response measurements for devices before and after nanoparticle deposition using monochromatic 300 W Xe lamp illumination across the region of the solar spectrum where the cells is absorbing. The band gaps of both GaN and InGaN are indicated in the figure. The cell with a 50 nm p-GaN emitter layer (Figure 2.5A) shows a 6% overall increase in external quantum efficiency (EQE) with the addition of nanoparticles. The majority of this enhancement occurs below the GaN band edge, at wavelengths longer than 360 nm, indicating that the photocurrent enhancement is primarily due to the InGaN QW layer. Figure 2.5B shows the cell with a 200 nm thick emitter layer. In contrast, the EQE enhancement is predominantly above the GaN band gap (at wavelengths shorter than 360 nm) indicating that the absorption enhancement occurs primarily in the GaN. Here the EQE increases by 54% overall due to the nanoparticles. The control cells for both cases underwent the same processing, including both etching and cycling in the thermal evaporator, but no change in the photocurrent upon illumination was observed. The notable difference in EQE between the two cells suggests that the light absorption is most strongly enhanced in the region closest to the Ag nanoparticles. The photocurrent enhancement may result from a combination of scattering, local field enhancement, and antireflection

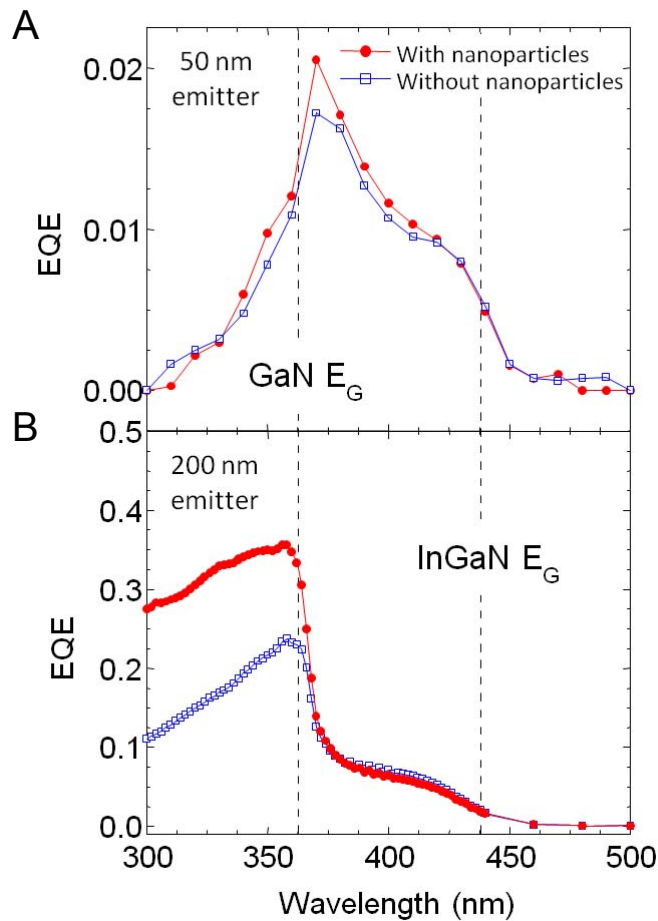


Figure 2.5. A. External quantum efficiency (EQE) curves of a QW cell with a 50 nm p-GaN emitter layer before and after nanoparticle deposition. B. EQE curves of a QW cell with a 200 nm p-GaN emitter layer before and nanoparticle deposition.

coating effects. We will explore this further in section 2.6.

2.4 Current-Voltage Measurements

Current-voltage measurements of the device with a 200 nm p-GaN emitter region under the AM 1.5 spectrum at 1 sun illumination (100 mW cm^{-2}) are shown in Figure 2.6. The presence of nanoparticle arrays on the cells increases the short circuit current from 0.223 to 0.237 mA cm^{-2} . For reference, the change in photocurrent for the control cells before and after processing was less than 1%. The increase in short circuit current (J_{sc}) is attributed to absorption enhancement evident from the spectral response measurements. The low open circuit voltage (V_{oc}) for these cells is attributed to damage induced by the dry etch processing required to remove the metal LED contacts. We note, however, that these values are the same for both samples with and without nanoparticles, as we would expect. The fill factor (FF), which is a ratio of the actual power output to the theoretical maximum, is also the same for both cases. The deterioration in V_{oc} that occurred upon etching the cells with 50 nm p-GaN emitter layers made the current-voltage measurements unreliable.

2.5 Device Physics Modeling

The enhanced J_{sc} could also be attributed to an increase in carrier collection efficiency at the surface of the cell. One plausible explanation for this observation is band bending at the metal-semiconductor interface, which increases the width of the depletion region and reduces the number of carriers lost to recombination in the emitter. Other research groups have shown that metal contacts to GaN can cause significant band bending at the semiconductor surface [48]. Metal layers have also been used to improve the contact to both p-GaN and p-AlGaN layers causing an increase in the depletion width at the surface of the device [49].

We use 1D device physics simulations (AFORS-Het) to model the change in the band bending and transport for cells with Ag nanoparticle arrays and, specifically,

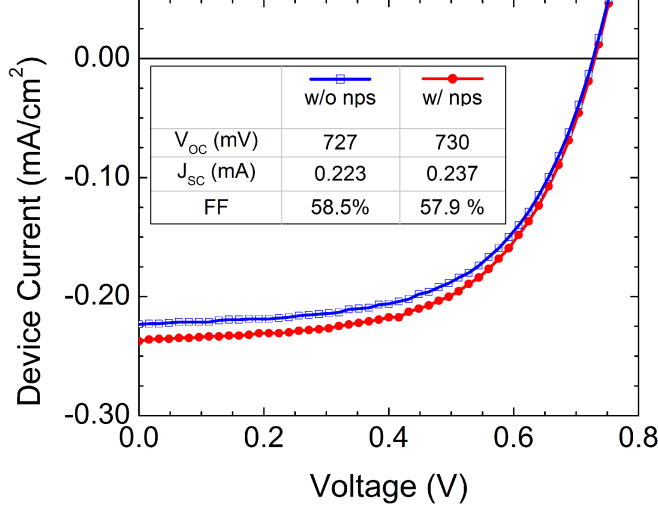


Figure 2.6. Current-voltage measurement of an InGaN QW solar cell with a 200 nm p-GaN emitter layer, with (red line) and without (blue line) nanoparticles.

to understand the possible improvement in carrier collection upon nanoparticle layer formation. In our model of cells covered with Ag nanoparticles, we assume band bending equivalent to the Ag-GaN barrier height of 0.54 eV at the semiconductor surface (Fig. 2.7A) [48] and a reduction of carrier recombination in the p-GaN emitter. The simulated versus the experimental EQE for both control cells and the nanoparticle-decorated 200 nm p-GaN emitter cell are shown in Fig. 2.7B, and show excellent agreement. This EQE calculation assumes a photon flux of $1 \times 10^{16} \text{ cm}^{-2} \text{ s}^{-1}$ and is calculated over the wavelength range from 300 to 500 nm, where the cell is photoactive. After validating the model against the experimental EQE measurements, it was then used as a basis for optimizing device design. Using the model, we calculated the relevant solar cell operating parameters for various emitter thicknesses under the AM 1.5 spectrum at 1 sun illumination (Table 2.1). For each emitter thickness, we compute efficiency, η , and compare to a 200 nm thick emitter reference cell without nanoparticles, η_0 . We report efficiency enhancement versus this reference cell (η/η_0) and find that an optimum emitter layer thickness of 65 nm doubles the efficiency of the modeled cell (Fig. 2.7C) with nanoparticles. Interestingly, this is slightly thicker

Table 2.1. Solar cell characteristics from AFORS-Het calculations

Buffer (nm)	V _{OC} (mV)	J _{SC} (mA/cm ²)	FF
200	2230	0.249	75.1%
100	2250	0.429	69.7%
50	2260	0.590	70.1%
20	2330	0.637	83.9%

that the 50 nm optimum emitter thickness for the cell without nanoparticles.

2.6 Modeling of Optical Generation Rates

In section 2.3, we found that the increase in EQE was predominantly in the layer closest to the nanoparticle array. To further investigate this, we modeled the electron generation rates via full-field electromagnetic simulation, using the commercially available software package, Lumerical. In the model, we vary emitter layer thickness from 20 to 200 nm, in order to understand where the photons are being absorbed and the optical consequence of thinning the emitter region. Electromagnetic simulations were run at discrete wavelengths across the entire spectrum using an approach pioneered in our lab by Ferry et al. [39, 50]. These calculations assume that for each photon absorbed, an electron is generated. Consequently, unlike the device physics modeling, these calculations do not account for the collection efficiency of the cell and represent an idealized upper bound to electron generation rates. They can, however, be used to understand where absorption is happening in the cell. The spectral response of the cell was determined by calculating generation rates at each wavelength, λ , according to equation (2.4).

$$G_{opt} = \frac{1}{2\hbar\omega} \Re[\Delta \bullet \mathbf{S}] = \frac{\epsilon'' |\mathbf{E}|^2}{2\hbar} [cm^{-3}s^{-1}] \quad (2.4)$$

Where G_{opt} is the generation rate at each wavelength, \mathbf{S} is the Poynting vector, ϵ'' is the permittivity, and \mathbf{E} is the electric field. The standard AM 1.5G spectrum is shown

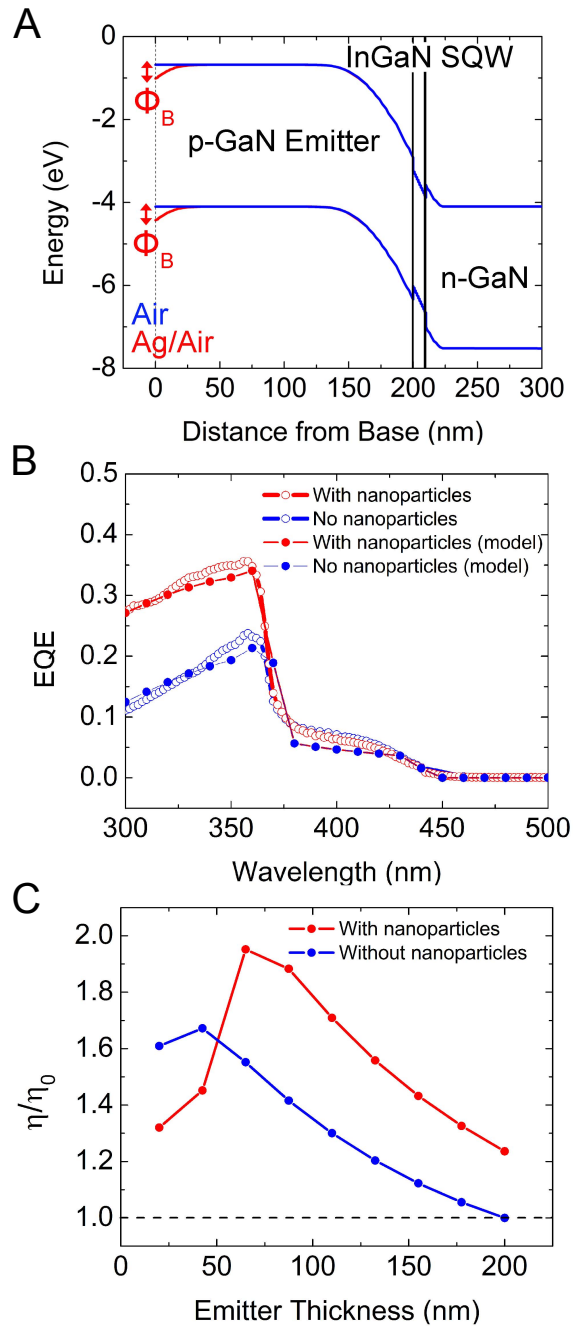


Figure 2.7. A. Band diagram generated in AFORS-Het for cell before and after nanoparticle deposition. B. AFORS-Het simulation of cell and experimental data before and after nanoparticle deposition. C. Solar cell efficiency calculations for different emitter layer thicknesses.

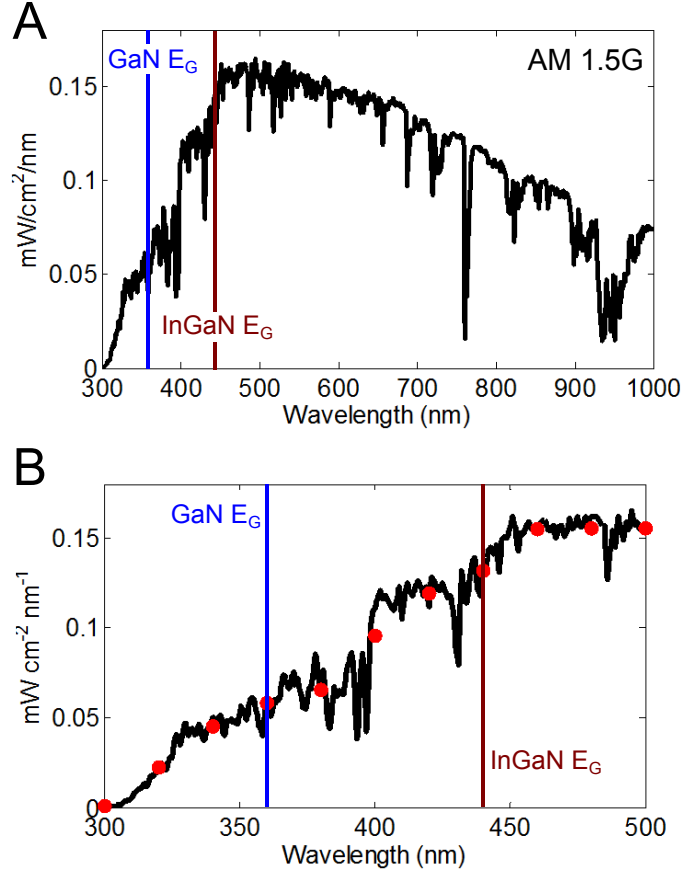


Figure 2.8. A. The standard AM 1.5G spectrum is shown with the GaN and InGaN band gaps highlighted. The portion of the spectrum that is used for the generation rate calculations is shown in (B) along with the discrete wavelength points that are simulated.

in Fig. 2.8A, along with the band gaps of GaN and InGaN. Given that the band gap of the InGaN used in our experiments is 440 nm, we calculate the generation rates from 300 to 500 nm at the discrete wavelengths shown in Fig. 2.8B.

The simulated electron generation rates weighted by the entire AM 1.5G incident spectrum are shown in Fig. 2.9. The top panel shows the anticipated generation rate profile for a flat cell, while the bottom cell shows the profile for a cell decorated with 100 nm diameter Ag nanoparticles. It is evident that the nanoparticles affect the absorption profile through the active region, and we can optimize the observed enhancement by tuning the size, spacing, and emitter thickness.

As a corollary to the device physics work previously discussed, we calculate generation rates for varying emitter thicknesses at each wavelength. Figure 2.10A shows the generation rate profile at 400 nm for a 20 nm GaN emitter layer with 100 nm diameter particles. As 400 nm is at a longer wavelength than the GaN band gap, there is only absorption in the InGaN region and the rest of the plot appears dark. There is a concentration effect between particles, and it is in these regions that the generation rate is highest. We can integrate over the InGaN region and determine the generation rate at each wavelength. We normalize these generation rates to a cell with the same emitter layer thickness without nanoparticles to determine generation rate enhancement. The results for a 200 nm emitter and a 50 nm emitter cell are shown in Fig. 2.10B. We find that for the 200 nm emitter, the optical generation rates are enhanced by up to 10% at certain wavelengths. The improvement in the 50 nm emitter cell is presumably less pronounced because the QW is already absorbing most of the incident light.

We expect that additional improvements could be achieved by thinning the entire cell, so that the semiconductor layers support waveguide modes leading to higher absorption enhancements. However, given the necessity of buffer layer growth and the low dielectric contrast of GaN to the sapphire substrate, this material system does not lend itself to making thin waveguides, making the goal of a SQW-based solar cell with ultra-thin cladding somewhat elusive.

2.7 Summary

We have investigated the effects of incorporating arrays of Ag nanoparticles on InGaN QW solar cells with emitter layer thickness of 50 and 200 nm. Devices with 50 nm emitter layers showed an overall 6% enhancement in photocurrent, with the increase occurring predominantly in the InGaN active region. Photocurrent was enhanced by 54% in cells with a 200 nm thick emitter layer, due primarily to enhanced absorption and collection in the p-GaN emitter, and JV characteristics also improved. Device physics simulations were used to understand the improved carrier collection

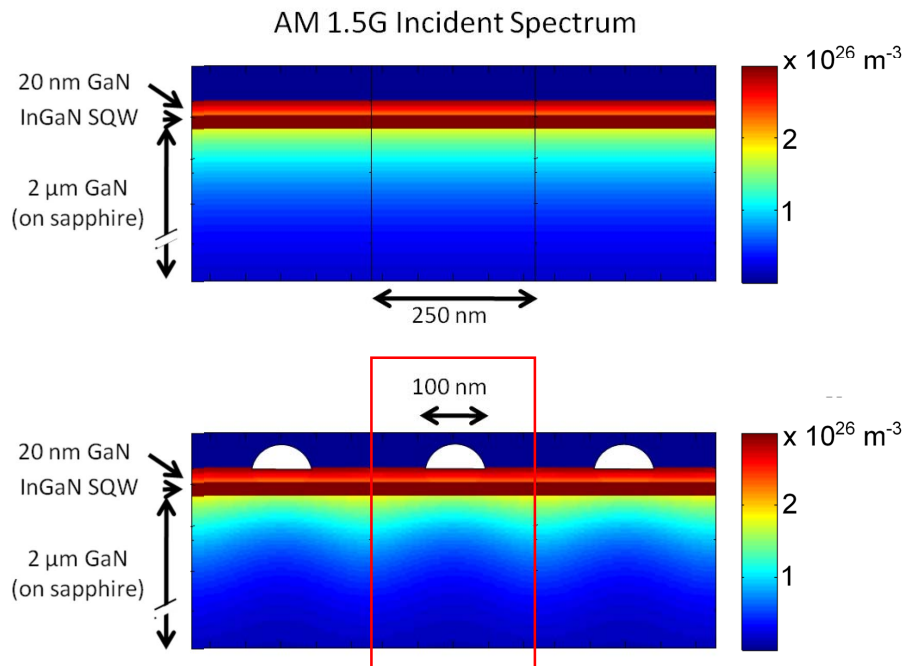


Figure 2.9. Electron generation rates calculated from full field electromagnetic simulation are shown. Rates are calculated at multiple frequency points and weighted by the AM1.5G spectrum. The top cell shows the generation rate profile for a flat InGaN quantum well cell while the bottom cell shows the generation rate profile for the same cell with 100 nm diameter Ag nanoparticles. The red box indicates the periodic unit cell used for the 3D simulation.

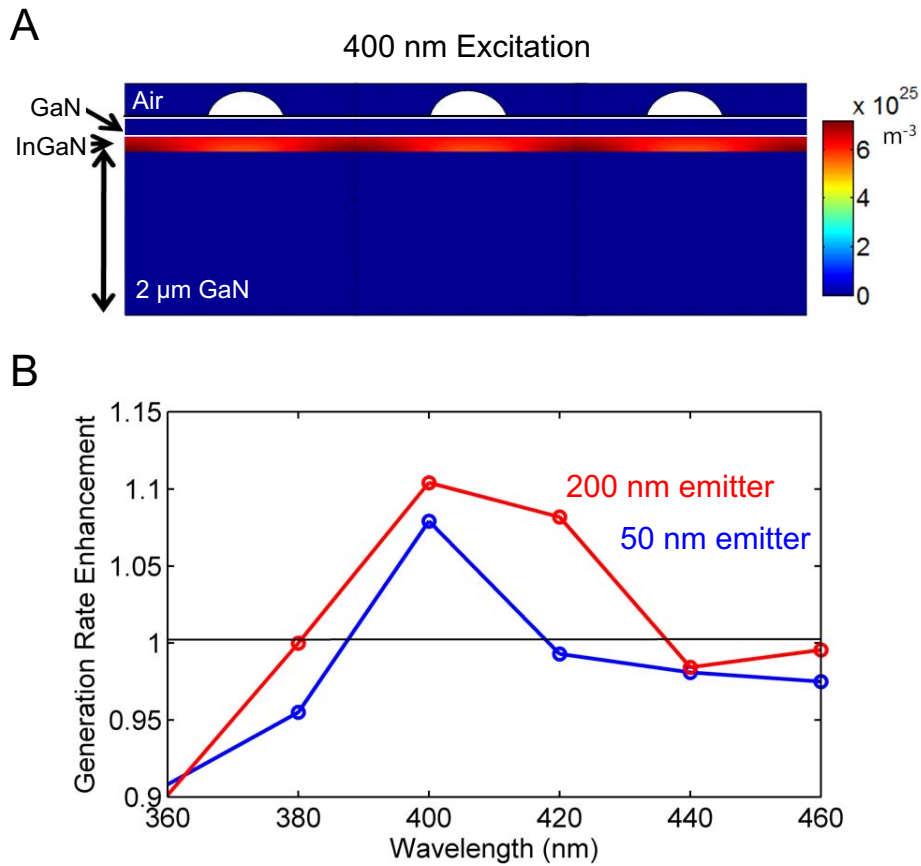


Figure 2.10. A. Electron generation rates in the InGaN single quantum well are calculated from full field electromagnetic simulation. The generation rates for an excitation wavelength of 400 nm are shown graphically. B. Generation rate enhancement is plotted as a function of wavelength for varying emitter thicknesses. Here the enhancement is determined by normalizing to a cell with the same emitter thickness but without nanoparticles.

of nanoparticle decorated cells and the model developed was used to optimize solar cell design for increased photovoltaic efficiency. Full field electromagnetic simulations also support the notion that thinning emitter layers should result in improved device performance and confirm the finding that absorption enhancement occurs primarily in the region closest to the nanoparticles. The single QW system is a useful platform for the exploration of absorption enhancement from plasmonic scatterers on ultra-thin cells designed for optimum photovoltaic response.

Chapter 3

Coupling in Metamaterials

As we discussed in the first chapter, metamaterials can be designed to exhibit particular resonant responses. They are comprised of periodic arrays of resonators with dimensions much smaller than the incident wavelength, and changing the size and geometry of the metamaterial elements can be used to shift the resonant features. In this chapter we outline how alternative metamaterial designs can be achieved with coupled asymmetric split-ring resonators (SRRs). By coupling resonators with different degrees of asymmetry and varying the coupling strength between resonators in a unit cell, the resonant frequencies and field intensities of arrays of SRRs can be modified. This chapter provides a framework for understanding coupling, while in later chapters we will use active design to tune the resonant properties.

3.1 Introduction

Metallic nanostructures can be used to generate plasmonic and metamaterial resonances at optical and near-IR frequencies. The ability to control the resonant frequencies of nanostructures through careful design of resonator shape and size opens up a wide set of possible applications ranging from sensing to optical modulators and filters. Breaking the symmetry in coupled metallic nanostructures is another tool that can be used to engineer the resonance, making it possible to access resonant modes that cannot typically be observed. Significant research efforts have led to the design of arrays of asymmetrically coupled plasmonic nanostructures and metamaterials that exhibit complex resonant phenomena such as plasmon resonance hybridization [51, 52], dark mode coupling [53, 54, 55], Fano resonances [56, 57, 58]

and electromagnetically induced transparencies (EIT) [59, 60, 61]. The ability to access more complex types of resonant effects leads to important design improvements for arrays of coupled particles over single nanostructures, such as the narrowing of the resonant line width.

The plasmon resonance hybridization framework describes coupled metallic nanostructures, such as nanoparticles, nanowires, or nanoshells, as having coupled hybridized energy levels analogous to the molecular wave functions in molecular orbital (MO) theory. Unlike MO theory, however, plasmonic and metamaterial structures enable complete control over not only which *meta*-atoms are making up a particular system, but also which mode is the symmetric and which is the antisymmetric. By changing orientation and alignment of coupled nanostructures such that their magnetic or electric dipoles are either in phase or out of phase, the energy levels can be shifted and even switched. This has been studied for basic metamaterial “atoms” by Liu et al. [30, 31], where the primary goal was to understand change in orientation of the structures in order to affect the relative magnetic dipole strengths of coupled resonators. In this work, we discuss how changing the coupling distance and sizes of *meta*-atoms in a fixed orientation can lead to similar resonant effects.

3.2 Experiment and Simulation Details

We use arrays of SRRs as a metamaterial design platform to study the effects of symmetry breaking, coupling, and resonance hybridization. In Fig 3.1, a schematic of a representative coupled SRR unit cell is depicted. We refer to the particular system shown as “tip-coupled SRRs,” as the tips of the SRR arms are facing each other. The SRRs have different arm lengths, denoted here as L_1 and L_2 , and the coupling distance between the resonators, d , is varied through the study. The width of the SRR, $w = 360$ nm, the in-plane periodicities $a_x = 750$ nm and $a_y = 975$ nm, and the metal thickness, $z = 120$ nm are kept constant for all the coupled and uncoupled SRR systems investigated. The Au resonators were fabricated in 100×100 μm area arrays on glass substrates with a 30 nm indium tin oxide (ITO) coating using standard

e-beam lithography followed by e-beam Au evaporation. A 2 nm Ti layer is used as an adhesion layer. All resonators patterns reported here were fabricated on the same glass slide. Representative scanning electron microscope (SEM) micrographs of the resonator unit cells are shown in Fig. 3.2.

The arrays of resonators were characterized using a Fourier Transform Infrared (FTIR) spectroscopic microscope in transmission mode. Transmission spectra were taken over a 25 x 25 μm area and normalized to a glass substrate without ITO. The spectra were collected from 1.4 to 3.2 μm . In this configuration, the electromagnetic (EM) wave was normally incident to the SRR plane ($\mathbf{k} \parallel \mathbf{z}$), with the electric field polarized perpendicularly to the arms and parallel to the x -axis ($\mathbf{E} \parallel \mathbf{x}$, $\mathbf{H} \parallel \mathbf{y}$). We can describe the individual SRRs as a nanoscale LC resonator, where the effective inductance, L , arises from the loop formed by the SRR. The effective capacitance, C , is due to the charge build-up across the split-ring gap. The E-field must be perpendicular to the SRR arms, as described, in order to drive the resonant response. This response is also characterized via full field electromagnetic simulation using the finite-difference time-domain (FDTD) method. A single unit cell is modeled with periodic boundary conditions in both the x - and y -directions to mimic the periodic array of SRRs. Perfectly matched layers are used along the z -direction, perpendicular to the metamaterial surface. A broadband plane wave is incident on the unit cell, and transmitted power is monitored using a power monitor placed behind the SRR unit cell. In the simulations, we employed experimental values of the complex refractive indices of Ag and ITO layer as determined from variable angle spectroscopic ellipsometry (VASE).

We first change the degree of asymmetry in a unit cell, by changing the arm lengths, L_1 and L_2 , of the SRRs relative to each other (section 3.3). The arrays in Fig. 3.2C show an example of this type of symmetry breaking. We then fix the resonator arm length and vary the coupling distance, d , between them (section 3.4.1). This results in changing the coupling strength and physically moving from “tip-coupled” arrays (Fig. 3.2A) to “back-coupled” arrays (Fig. 3.2C). The resonant behavior of these systems is compared to arrays of uncoupled SRRs (Fig. 3.2D)

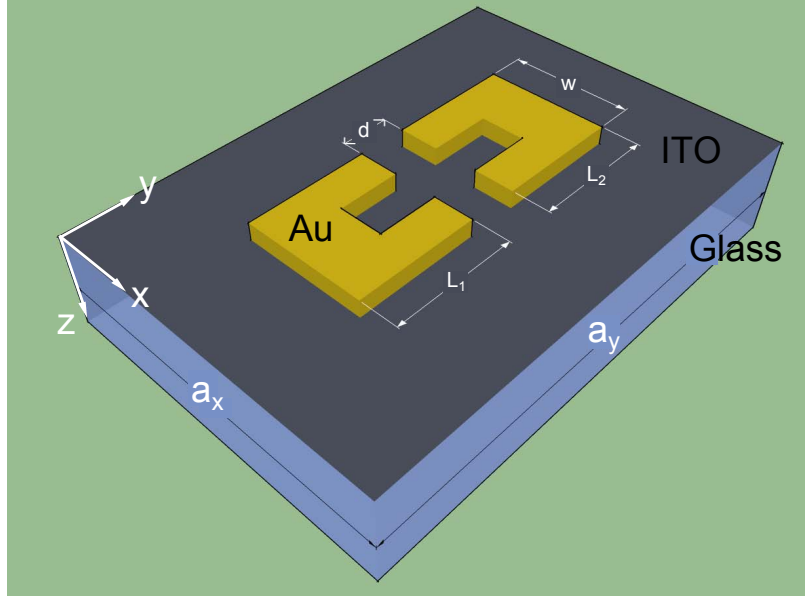


Figure 3.1. The schematic shows the a “tip-coupled” split-ring resonator (SRR) unit cell. The arrays of Au SRRs used in this study were patterned on ITO-coated glass slides with periodicities of a_x and a_y .

and we propose a hybridization framework which describes the coupled SRRs (section 3.4.3). Finally, we study the effects of extreme symmetry breaking where we transition from two coupled SRRs to an SRR coupled to a nanowire (section 3.5).

3.3 Changing Resonator Length to Introduce Asymmetry

Asymmetry is first introduced to the coupled SRR system by changing the arm length of the top and bottom SRRs (L_1 and L_2). The total length of the SRR arms, $L = L_1 + L_2 = 580$ nm and the coupling distance between the SRRs, $d = 150$ nm, are both kept constant. SEM micrograph images of the unit cells of five different coupled SRR arrays are shown in Fig. 3.3C where the arm lengths of top and bottom SRRs are $L_1 = 290, 310, 340, 370, 400$ nm and $L_2 = 290, 270, 240, 210, 180$ nm (from left to right). Measured and simulated transmission spectra for the corresponding

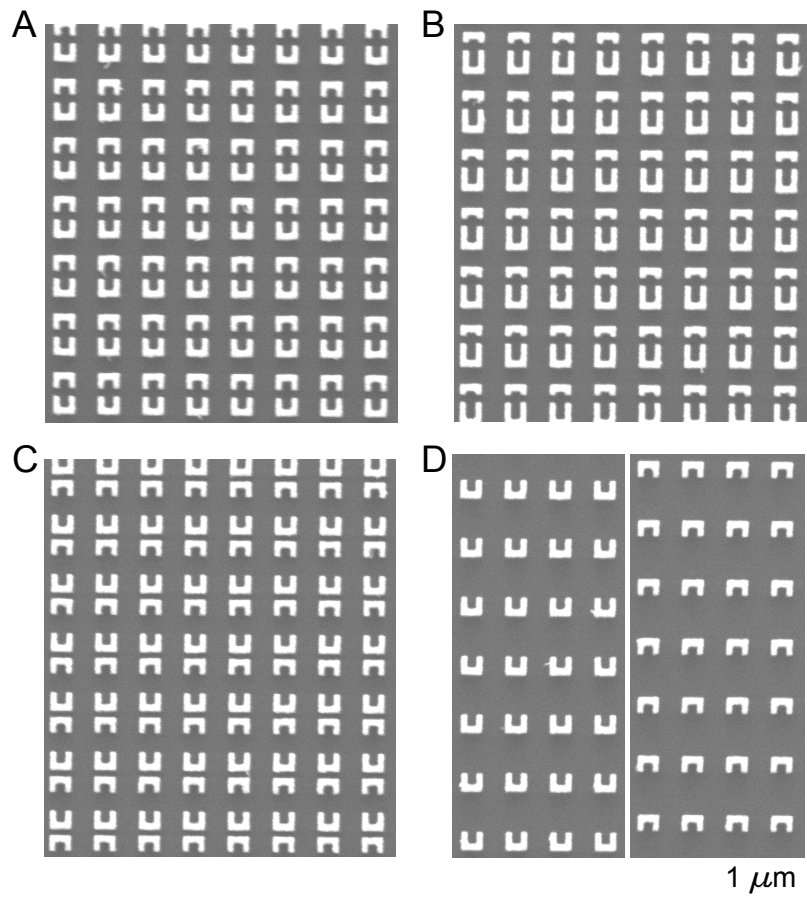


Figure 3.2. A. A “tip-coupled” split-ring resonator (SRR) unit cell. B. A “tip-coupled” SRR unit cell with much shorter arm length than that shown in A. C. A “back-coupled” SRR unit cell. D. Single SRR unit cells designed to show the resonators’ natural frequencies.

coupled SRR arrays are plotted in Fig. 3.3A and 3.3B, respectively. For the symmetric configuration, where the resonators have the same arm length ($L_1 = L_2$), a broad resonant dip is observed both in the experimental and the simulated data (black line) at $\lambda = 1.78 \mu\text{m}$. This is marked by λ_1 in the graph and is the spectral behavior that is anticipated for a single uncoupled SRR at near-IR wavelengths (see Ch. 2).

The asymmetry of these coupled arrays results in an additional resonance dip at longer wavelengths. For the asymmetric coupled SRRs with arm lengths of $L_1 = 310 \text{ nm}$ and $L_2 = 270 \text{ nm}$, the resonance that arises due to asymmetry results in a transmission dip in the measured spectra at $\lambda = 2.28 \mu\text{m}$ and in the simulated spectra at $\lambda = 2.30 \mu\text{m}$ (red line). This resonance is marked by λ_2 in the graph. The shallow dip in the measured transmission spectra of symmetric SRR arrays (black line in Fig. 3.3A) is attributed to unintentional asymmetry that was introduced during the fabrication process.

Breaking the symmetry in plasmonic nanostructures and metamaterials thus allows access to different resonant modes, which cannot be excited with coupled symmetric resonators. These have previously been dubbed dark modes, subradiant modes, and trapped modes as they do not freely radiate. They couple weakly to free space and thus need an external perturbation such as the symmetry breaking of the resonator geometry in order to be excited. In our system (Fig. 3.3), the symmetric coupled resonator system, where $L_1 = L_2$ (black line), traps the dark mode. As the asymmetry is increased, the dark mode that is visible at longer wavelengths becomes more and more prevalent.

The increase in degree of asymmetry also results in a separation of the two resonant frequencies, i.e., blueshifting of the LC resonances at shorter wavelengths and redshifting of the dark-mode resonances at longer wavelengths (yellow, red and brown lines). The separation of the resonant frequencies can be understood with an LC resonance picture. Changing the physical size of the nanoscale LC resonators results in a change in the effective inductance L and capacitance C . The change in size alters the resonant wavelengths of each individual SRR in the coupled SRR system and as the sizes of the SRRs become more disparate, the resonances diverge. For example,

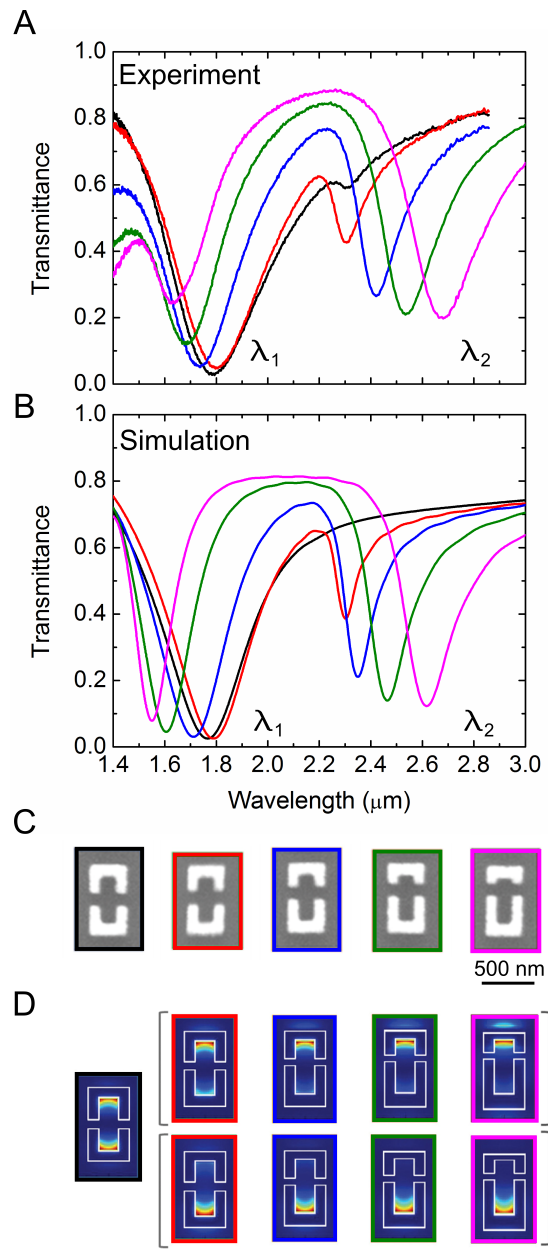


Figure 3.3. A. Experimentally measured FTIR transmission spectra and simulated transmission spectra (B) for 5 different coupled SRR systems. C. SEM micrographs of single representative unit cells of the corresponding coupled SRR unit cells. D. Magnetic field intensities as calculated from simulation of coupled SRR unit cells at their respective resonant frequencies.

the resonant wavelengths of the individual SRRs with $L_1 = 310$ nm and $L_2 = 270$ nm (red frame in Fig. 3.3C) are closer than the SRRs with $L_1 = 400$ nm and $L_2 = 150$ nm (pink frame).

We calculated magnetic field intensities along the z-axis ($|H_z|^2$) at the SRR-substrate interface at the resonant wavelengths corresponding to the dip of the transmission resonances as marked by λ_1 and λ_2 (Fig. 3.3D). Under resonant conditions, the magnetic field intensity is enhanced at the center of the SRR, due to the circular surface current excited by the incident electric field. For the symmetric coupled SRRs, the contributions of the top and bottom SRRs to the dipole moments are equal. As the magnetic field intensity for both SRRs is enhanced at the same wavelength, these are equal and contribute to the strong, broad resonance that is visible at 1.8 μm . For the asymmetric coupled SRR systems, however, the contribution of the larger SRR structure is dominant at the longer wavelength resonance (λ_2) and the contribution from the smaller SRR dominates the resonance at the shorter wavelength (λ_1) in agreement with the *LC* resonance description.

The degree of asymmetry controls both the EM resonant frequency and the intensity of the signal. In particular, the asymmetry affects the resonant linewidth and thus the quality-factor (*Q*-factor) of both the bright and dark-mode resonances (Figs. 3.3A and B). The *Q*-factor is the ratio of the resonant bandwidth ($\Delta\omega$) to the resonant frequency (ω), $Q = \Delta\omega/\omega$. Here we define the *Q*-factor in terms of the resonant wavelength, where $Q = \lambda/\Delta\lambda$. We define the resonant linewidth ($\Delta\lambda$) as the full width at half maximum (FWHM) at the resonant wavelength (λ). For the symmetric CSRR configuration, the quality factor is calculated from the measured transmission spectra to be $Q \approx 4.0$ at $\lambda = 1.78$ μm with $\Delta\lambda = 0.45$ μm . For the coupled SRR arrays with the lowest degree of asymmetry, the quality factors for the bright-mode resonance and the dark-mode resonance are $Q_1 \approx 4.5$ and $Q_2 \approx 23$, respectively. For lower degrees of asymmetry, the dark-mode resonances exhibit much higher quality factors than is typically achievable with resonators comprised of lossy metallic nanostructures at optical frequencies. The *Q*-factor for dark-mode resonances, however, decreases with increasing degree of asymmetry [53]. *Q*-factors

for the dark-mode resonances are 13, 10, and 7.5 for the blue, green, and pink lines, respectively (Fig. 3.3).

The Q -factors of the resonances are affected by several factors, including material losses due to absorption in the metal and ITO layers, losses due to coupling of incident electromagnetic wave with the resonators, and deviation from the ideal simulated parameters due to inhomogeneities introduced during fabrication. The resonator Q -factors could be increased by using lower loss substrates or by adding gain media into the metamaterial arrays. The ability to control the Q -factor of resonant elements is important for many applications, especially for biological and chemical sensors, narrow-band transmission/reflection filters and modulators.

3.4 Coupling Split-Ring Resonators

3.4.1 Distance Dependence

Inspired by coupled harmonic oscillators in classical mechanics in which resonant frequencies depend on the coupling strength, we propose controlling the coupling strength between the resonator elements as an alternative approach to tuning the metamaterial resonance. The effect of coupling strength was explored by varying the distance between two coupled SRRs. We chose as a test system the coupled asymmetric SRR system with the lowest degree of asymmetry, where $L_1 = 310$ nm and $L_2 = 270$ nm (green in Fig. 3.4). We fabricated four different coupled SRR arrays where the distance between SRRs decreased from $d = 150$ to 60 nm as shown in the SEM micrographs in Fig. 3.4. Figure 3.4 also shows the experimental (top panel) and simulated (bottom panel) FTIR transmission spectra of each array. The simulated results are in good agreement with the experimentally measured spectra. As the coupling distance is reduced, there is a redshift of the dark-mode resonance and a blueshift of the bright mode resonance. The Q -factors calculated for these spectra are $Q \approx 35$ for the trapped mode resonances and $Q \approx 4$ for the bright mode resonances. The Q -factors are the same for all coupling distances, thus coupling strength does

not change the quality factor of a coupled resonator. It is notable, however, that the transmission dip deepens with decreased coupling distance for dark-mode resonances at longer wavelengths. This is attributed to the increased phase difference in induced dipole oscillations with increased coupling strength [62].

3.4.2 Uncoupled versus Coupled Resonators

To better understand asymmetrically coupled SRRs in a resonance hybridization framework, we performed additional measurements and simulations for individual SRRs. Single SRR arrays with $L = 310$ and 270 nm are fabricated. The shorter SRR (blue line in Fig. 3.5) is resonant at 1.92 μm , whereas the larger SRR (red line in Fig. 3.5) is resonant at 2.16 μm . In Fig. 3.5, we plot the uncoupled SRR spectra with those for tip-coupled (green line) and also back-coupled SRRs (light blue line), where the resonators are back to back. The resonant wavelengths of the back-coupled SRRs are almost coincident with the resonant wavelengths of the individual uncoupled SRRs. This indicates that the coupling between back-to-back SRRs is very weak, even though they are only separated by 60 nm. The resonant wavelengths for tip-coupled SRRs separated by 60 nm are significantly shifted from the natural resonant wavelengths of the individual uncoupled SRRs due to the strong coupling at small distances. If we consider that the back-coupled SRRs are in fact a tip-coupled system with very large coupling distance then the large difference in resonant response is more understandable. The same behavior is evident for both the experimental and the simulated data.

3.4.3 Hybridization Picture for SRRs

In Figure 3.6, we plot resonance as a function of the distance between resonators. The blue and orange dashed lines correspond to the resonant wavelengths of uncoupled large and small SRRs, respectively. These are the same resonators that were shown in Fig. 3.5. For large inter resonator distances, the coupling effect is very weak and the resonances overlap with the natural resonant wavelengths of the uncoupled

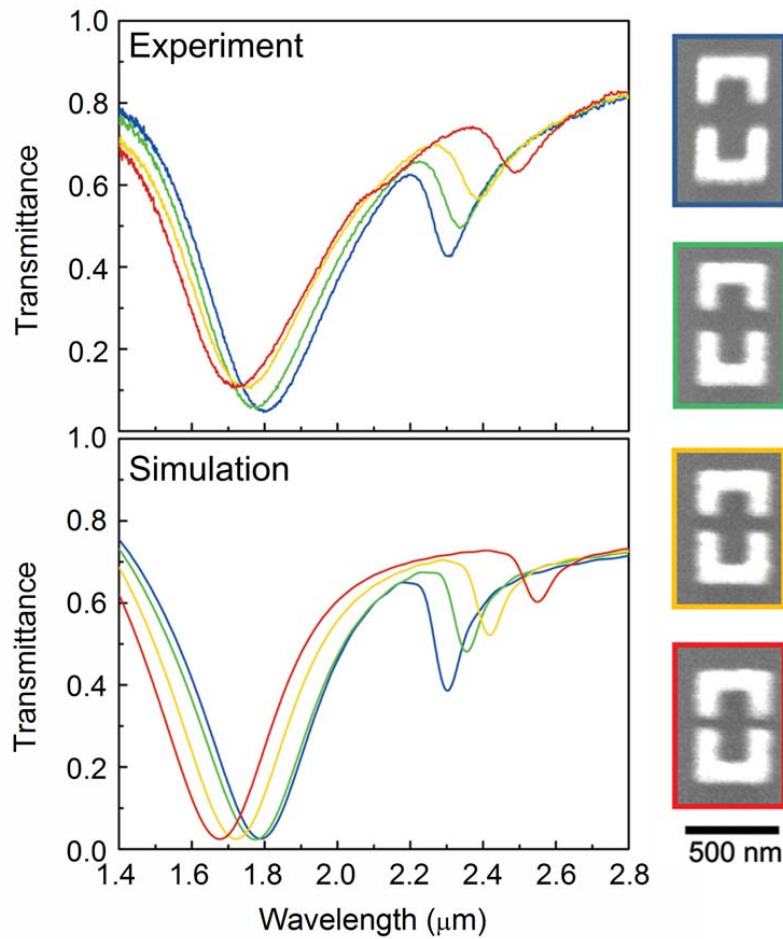


Figure 3.4. Experimentally measured FTIR transmission spectra (top panel) and simulated transmission spectra (bottom panel) for 4 different coupled SRR systems with decreasing coupling distance. SEM micrographs of single representative unit cells of the corresponding coupled SRRs are shown in the right hand panel.

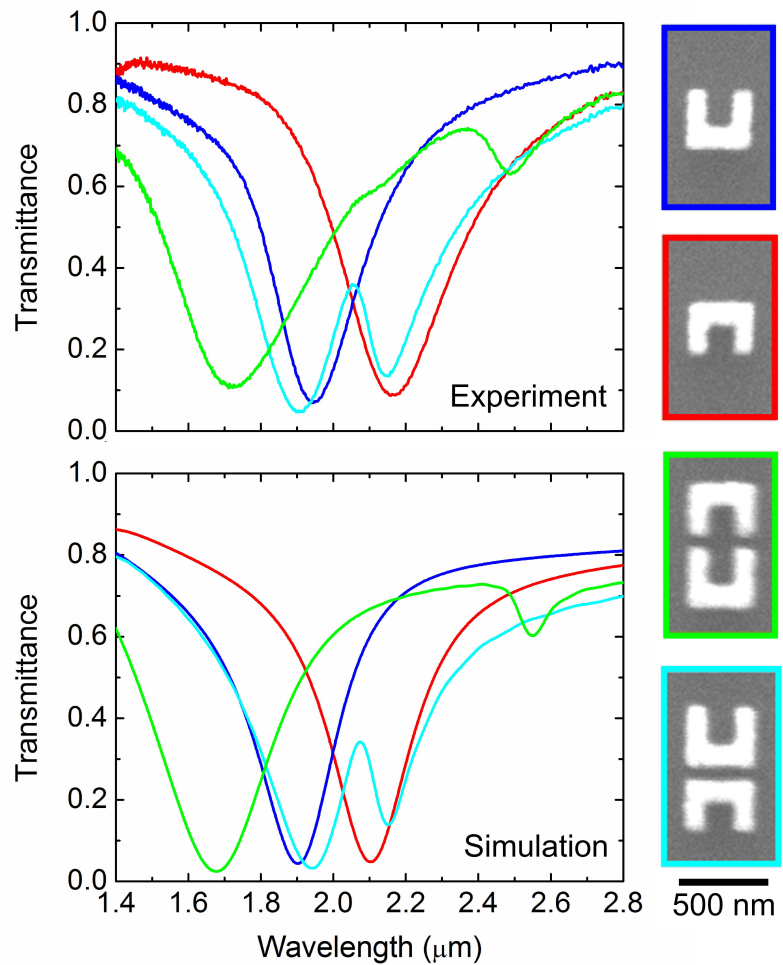


Figure 3.5. Experimentally measured FTIR transmission spectra (top panel) and simulated transmission spectra (bottom panel) for 2 different coupled SRR systems and 2 different uncoupled resonators. SEM micrographs of representative unit cells from the corresponding arrays are shown to the right.

resonators. For smaller coupling distances, however, we observe a strong resonance hybridization between the asymmetric SRRs. Given the agreement between experimental (red triangle) and simulated (blue circle) results, we performed simulations at shorter coupling distances of 10 and 30 nm to determine the change in resonant behavior for structures with dimensions smaller than those fabricated. We find that the resonant wavelength increases drastically at very small distances. A 10 nm coupling distance, for example, shifts the resonant wavelength to 3.62 μm . A schematic of resonance hybridization (Fig. 3.6 - right panel) depicts how the energy levels shift for various hybridization states. Snapshots of the electric field amplitudes along the x direction at the resonant wavelengths of the uncoupled and coupled SRRs (for $d = 60$ nm) are included in the schematic. The individual SRRs that are coupled together in this study have natural resonant frequencies ω_1 and ω_2 . Due to resonance hybridization, we observe both bright and dark modes for the coupled SRR system. This is analogous to the symmetric and antisymmetric modes of two coupled plasmonic structures described by plasmon hybridization theory [62].

3.5 Changing Resonator Shape for Extreme Asymmetry

We can combine the changes in arm length with changes in coupling distance to investigate strongly coupled systems with extreme asymmetry. In the resonance hybridization picture, the smaller resonator contributes more strongly to the bright (higher energy) resonance, and the larger resonator contributes more strongly to the dark (lower energy) resonance. This suggests that coupling two resonators with different natural resonant frequencies will lead to a large split in energy between the bright and dark mode resonances. To achieve very different natural resonances, we reintroduce the idea of asymmetrical lengths between structures. Recalling that the strongest effects are for high degrees of mismatch, the most extreme asymmetry is for $L = 0$. This is essentially a nanowire or nanobar and we refer to the coupled system

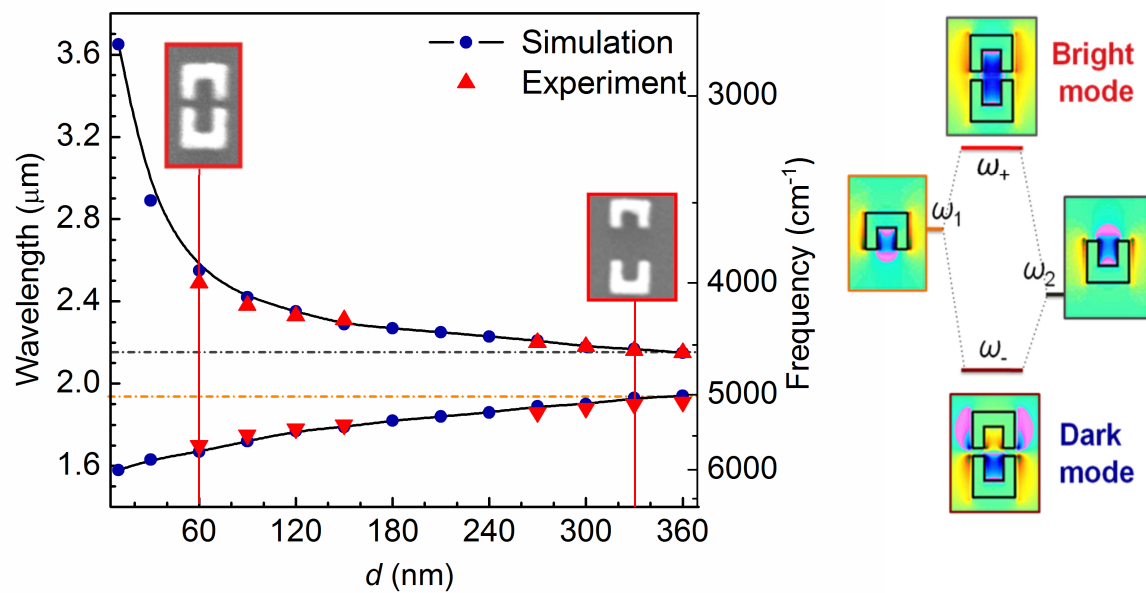


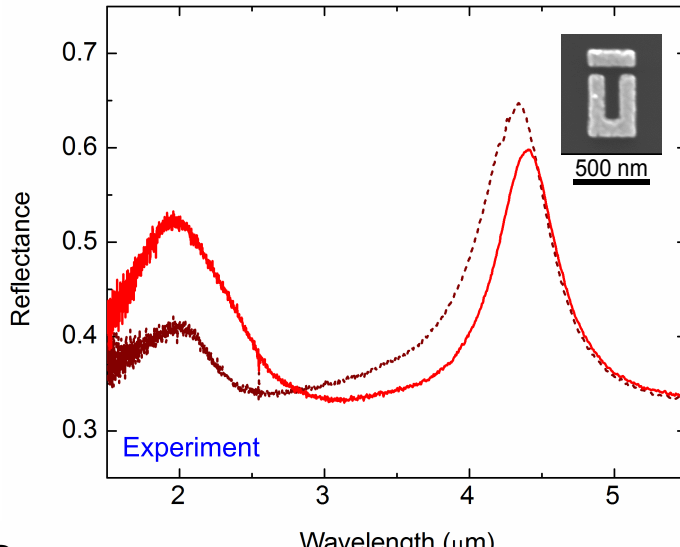
Figure 3.6. Measured and calculated resonance wavelengths of different tip-coupled SRRs as a function of distance. Resonance hybridization picture for a strongly coupled asymmetric SRRs. Time snapshot of electric field amplitudes are also provided for the corresponding resonance energies.

as an SRR-bar. The bar supports an electric resonance which is blueshifted from the SRR resonant wavelength. We can draw a similar picture of mode hybridization between these two structures, and given the relative dipole strengths of these two resonators, we can achieve a very high intensity antisymmetric resonance. As an example of this type of system, we show the experimental FTIR reflection spectra for both an SRR and a coupled SRR-bar on Si in Fig. 3.7A. We see that coupling to the bar does not significantly reduce the intensity of the signal, but it does result in a narrower linewidth and redshifts the resonant wavelength. In Fig. 3.7B, we report the simulated values for the reflection and show how the electric field intensity changes at each resonance. While it is convoluted with the broad electric resonance in the experimental data, the resonance for the coupled nanowire is evident as a small peak in the simulation data at $\lambda_{bar} = 2.5 \mu\text{m}$. In the subsequent chapters, we will use this structure quite extensively for the strong resonant signal and the relative ease of changing the distance between an SRR and nanowire for active metamaterial applications.

3.6 Summary

In this chapter, we have explored some important aspects of coupling in metamaterial unit cells. In particular, we have shown how two SRRs can be coupled together to achieve narrower spectral linewidths at the resonance frequency. In the work that follows, we will explore how these principles can be used to design frequency selective surfaces for modulators, filters, and sensors at infrared wavelengths. For many of these types of practical applications, it is desirable to tune the resonance over a wavelength range comparable to its linewidth, and so a narrower resonance can increase the tuning figure of merit (FOM), the ratio of the tuning range to the FWHM of the resonant peak. In particular, as we think about active metamaterial designs, the idea of coupling and ways that we can tune coupling between resonators will be critically important.

A



B

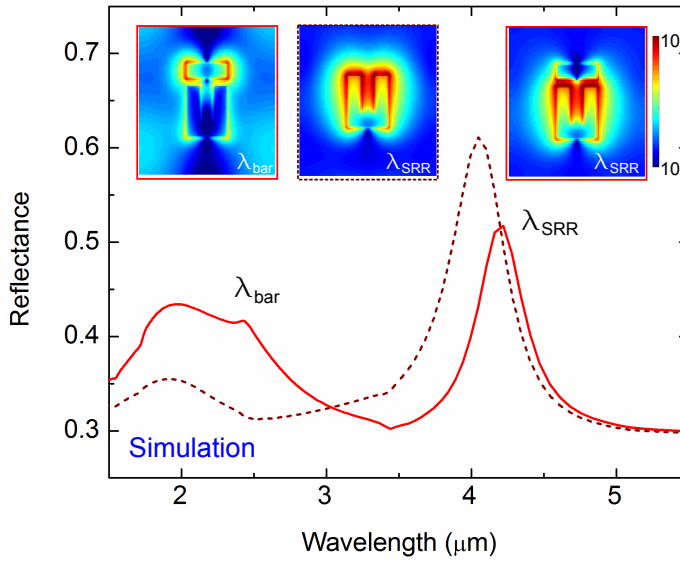


Figure 3.7. A. Experimental reflection spectra for both an SRR (dark red dotted line) and an SRR-nanowire coupled system (red line). A SEM micrograph of the fabricated SRR-nanowire structure is shown in the inset. B. The simulated data for the same structures are shown. The insets show the electric field intensity, $\|E\|^2$, at each resonant wavelength. These plots are all plotted on the same color scale as shown in the top right of the figure.

Chapter 4

Frequency Tunable Metamaterials Based on the VO₂ Phase Transition

In our first foray into the world of active metamaterials, we chose to exploit the phase transition of vanadium dioxide. At 68°C, VO₂ undergoes a transition from an insulator to a metal. By incorporating this switchable material into the unit cell of a metamaterial, we can create surfaces whose response changes completely as they are heated. Nanolithographic fabrication tools enable the design of materials that not only experience a bimodal on/off type behavior, but also materials with complex unit cells that have tunable responses. This means that in addition to modulating the resonant response, we can tune it to a desired frequency.

Engineering metamaterials with tunable resonances from mid-infrared to near-infrared wavelengths could have far-reaching consequences for chip-based optical devices, active filters, modulators, and sensors. Utilizing the metal-insulator phase transition in VO₂, we demonstrate frequency-tunable metamaterials in the near-IR, from 1.5 to 5 microns. Arrays of Ag resonators (SRRs) are patterned with e-beam lithography onto planar VO₂ and etched via reactive ion etching to yield Ag/VO₂ hybrid SRRs. FTIR reflection data and FDTD simulation results show the resonant peak position redshifts upon heating above the phase transition temperature. We also show that, by including coupling elements in the design of these hybrid Ag/VO₂ bilayer structures, we can achieve resonant peak position tuning of up to 110 nm.

4.1 Introduction

Electromagnetic resonances in subwavelength metallic resonators can be used to engineer optical responses not found in natural materials [1, 2]. Metamaterials have reemerged following their initial introduction [18], and are the subject of intensive investigation for applications in frequency selective surfaces [4, 5] and transformation optics, e.g. negative-index materials [24, 26, 29, 63], super-lensing [10, 57], and cloaking [12, 13, 14]. Active metamaterials have been demonstrated at terahertz frequencies using carrier depletion in GaAs [32, 64], photoexcitation of free charge carries in Si [33], and the metal-insulator phase transition in vanadium oxide thin films [65]. Typical metamaterials consist of arrays of metal structures embedded in a dielectric with feature sizes much smaller than the desired operating wavelength. In the simplest sense, the unit cell of a metamaterial array is designed to be an individual LC circuit with resonant frequency, $\omega_o \propto (LC)^{-1/2}$ [4]. Split-ring resonators (SRRs) are the basis for many metamaterial designs due to ease of fabrication and modeling. Each SRR has a distributed inductance, L , and a distributed capacitance, C , arising from charge build-up at the notch. The choice of materials and the resonator dimensions set these two parameters and determine the resonant frequency of the metamaterial. Active metamaterial designs have previously focused on changing the capacitance in the SRR gap to modulate the amplitude of the resonance [32, 33, 64]. Integrating materials with tunable electrical or optical properties allows further control over the resonant response in metamaterials. Vanadium oxide is a promising candidate that exhibits a dramatic change in its complex refractive index arising from a structural phase transition from monoclinic to rutile. Here, we propose an alternative geometry consisting of self-aligned, hybrid Ag/VO₂ SRR bilayers as an approach to tuning the metamaterial response in the near-IR by controlling the resonator geometry with the phase transition. VO₂ undergoes a structural transition from an insulating monoclinic phase to a metallic rutile phase at 68°C [66, 67]. This phase transition can occur on a subpicosecond timescale [68] and can be induced thermally, optically [69] or electrically [70]. As a result of the insulator-to-metal transition, the conductivity

increases by as much as four orders of magnitude and the optical transmission in the near-IR decreases significantly [71]. Drastic changes in the optical properties of VO_2 with the phase transition enable control over the transmission and reflection properties of nanophotonic structures, such as nanoparticles [71, 72], hole arrays [73], and metamaterials [65].

4.2 Vanadium Dioxide Growth

The VO_2 thin films were grown epitaxially by pulsed laser deposition on c-plane Al_2O_3 substrates at 500°C. A vanadium metal target was used as the source material and deposition takes place in a 12 mTorr oxygen environment. 60 nm thick VO_2 films were deposited with a 300 mJ laser pulse at a rate of 10 Hz. The deposition is particularly sensitive to both the oxygen partial pressure in the chamber and the substrate temperature and a parameterized study of the growth was necessary to determine the correct conditions. The growths were characterized using x-ray diffraction (XRD) (Fig. 4.1a). The peaks are indexed in this plot, showing that only one phase of VO_2 is present. We verified the switching of the VO_2 using both FTIR spectroscopy (Fig. 4.1B) and variable angle spectroscopic ellipsometry (VASE) (Fig. 4.1C). In both of these figures, the drastic effect that the transition has on the optical properties is evident.

4.3 Unit Cell Design and Fabrication

The active metamaterial device design presented here consists of self-aligned Ag/ VO_2 SRR arrays (Fig. 4.2A). Utilizing the insulator-metal phase transition in VO_2 , we can control the effective dimensions of the unit cell as well as the optical properties of the hybrid-SRR arrays in both phases. In this case, switching the phase of the VO_2 results in a change in effective thickness of the resonator. In addition to testing uncoupled SRRs, we also study coupled SRR systems. As discussed in Chapter 3, coupling metamaterial elements together enhances the local electric field in the unit

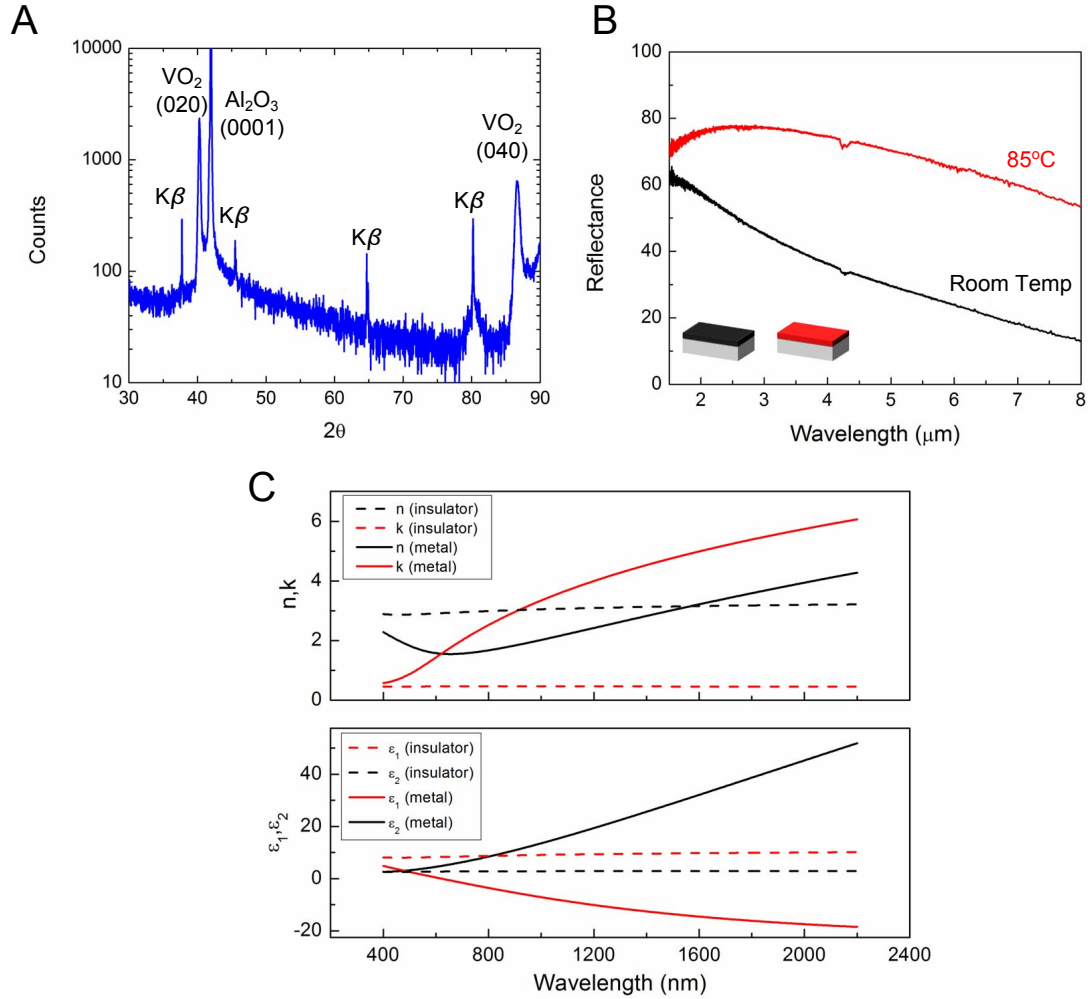


Figure 4.1. A. X-ray diffraction scan for a VO_2 film grown at 500°C in a 12 mTorr oxygen environment. B. Reflectance data for a thin film of VO_2 on sapphire as shown in the inset schematic are reported. The black line is the reflectance spectrum for a film at room temperature and the red line shows the data taken at 85°C . C. Variable angle spectroscopic ellipsometry (VASE) data for the VO_2 in both insulating and metallic phases is shown.

cell, which in turn reduces the spectral linewidth at the resonant frequency (Fig. 4.2B-D). A narrower resonant peak will increase the tuning figure of merit (FOM), the ratio of the tuning range to the full width at half maximum (FWHM) of the resonant peak. In this work, we investigate four self-aligned hybrid-SRR structures including two coupled SRR systems and one SRR coupled to a nanowire. The metamaterial arrays are patterned using standard electron beam lithography. Silver is thermally evaporated to create 150 nm thick resonators and 10 nm of chromium is subsequently evaporated to act as an etch mask. Following metal lift-off, the samples are etched using a CF_4/O_2 reactive-ion etch. The 100 W CF_4/O_2 plasma etches the VO_2 film not masked by the Cr/Ag SRR structures to yield hybrid Ag/ VO_2 SRR elements. The isotropic nature of this etch ensures that there is little undercutting of the underlying VO_2 .

4.4 Silver SRR Arrays on Planar Vanadium Dioxide Substrates

An SRR array fabricated on a 60 nm thick planar VO_2 film was tested using the reflection mode of an FTIR microscope with a light source in the range of 1.5 - 8 microns. Reflection data were normalized using an optically thick gold standard. Electromagnetic radiation, normally incident to the SRR array (along the z -direction) with the incident E-field polarized perpendicular to the SRR arms, was used to efficiently couple to the resonators and induce circulating currents in the structures (Fig. 4.2A). Two resonant reflection peaks, 2.1 μm (electric resonance) and 3.6 μm (magnetic LC resonance), were observed as shown in Fig. 4.3A. The sample was subsequently heated to temperatures above the insulator-metal phase transition temperature and then cooled using a commercial heating stage comprised of a silver block with a tiny aperture milled in the center. The resulting spectra show a continuous change from two distinct metamaterial resonant peaks to a broad reflection indicative of metallic VO_2 . Although there is a slight hysteresis, the resonances are recovered upon cooling

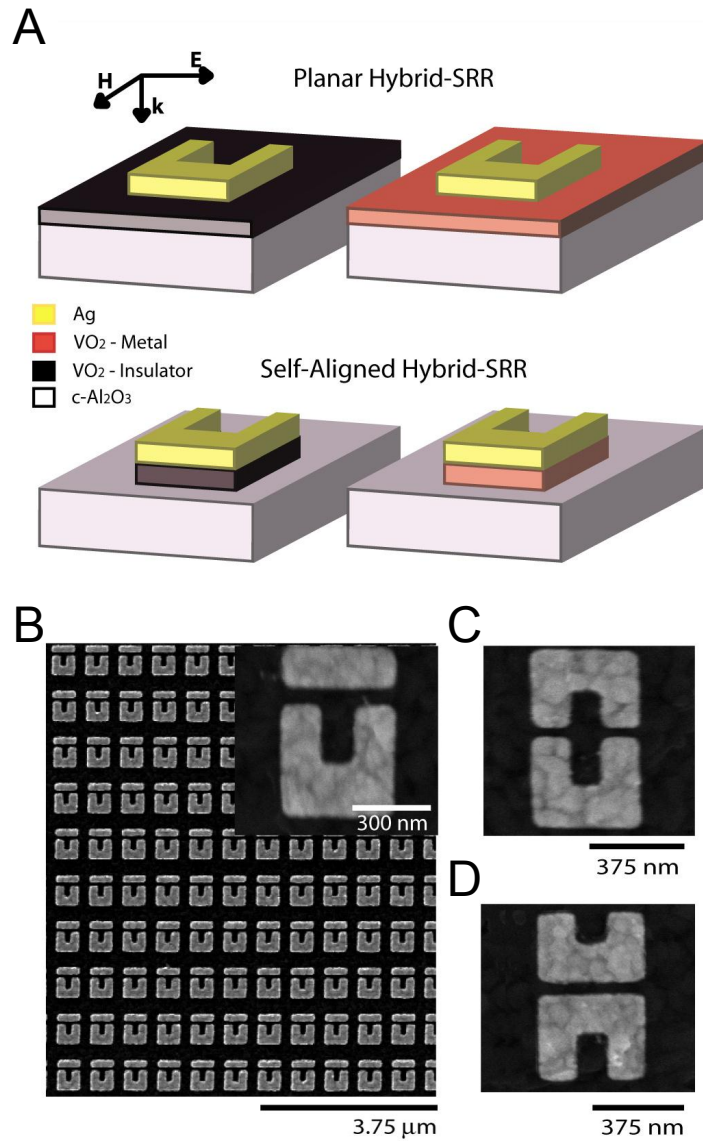


Figure 4.2. A. Schematic of a self-aligned silver/vanadium oxide metamaterial unit cell. The 150 nm thick silver SRR is fabricated by e-beam patterning and metal lift-off. $70 \times 70 \mu\text{m}$ arrays of these structures sit on 60 nm of VO₂. A 10 nm chromium mask protects the silver SRR during etching. B-D. SEM images of the three coupled-SRR metamaterial arrays studied in this work.

below the phase transition temperature. We also measured the reflection from a 60 nm thick VO₂ film on sapphire substrate at room temperature and 85°C. The reflection intensity at 3.6 μm increased from 0.36 to 0.75, indicating a drastic change in complex refractive index of the VO₂ thin film upon phase change (Fig. 4.1B).

The resonant response was modeled using Lumerical, a commercially available finite-difference time-domain (FDTD) simulation software. A unit cell of the investigated structure is simulated using periodic boundary conditions along the x - and y -axes and perfectly matched layers along the axis of propagation of the electromagnetic waves (z -axis). A broadband plane wave is incident on the unit cell along $+z$ -direction, and reflection is monitored by a power monitor that is placed behind the radiation source. Electric and magnetic fields are monitored by frequency profile monitors. Figure 4.3B shows the simulated response of an Ag SRR array on a planar VO₂ thin film in both the insulator and metallic phases. To accurately simulate the metamaterial response, we extend the complex refractive index of the VO₂ thin films in both phases (Fig. 4.3C) from the VASE measurements (Fig. 4.1C) by fitting to models. In the insulator phase, the VO₂ optical constants are fit to a Tauc-Lorentz model. In the metal phase, VO₂ acts like a Drude metal with strong absorption. These models were used to extrapolate the results to the near and mid-IR to aid in FDTD simulations. The simulated reflection spectra in both VO₂ phases agree well with the measured data. We calculated the magnetic field intensity, $|H_z|^2$ at $\lambda = 3.6 \mu\text{m}$ (inset of Fig. 4.3B) for the SRR array in the insulator (right) and metallic phases (left) of VO₂. The resonant behavior in the insulator phase is evident from the magnetic field profile, in which the magnetic field is concentrated at the center of SRR due to the excitation of circular surface currents at the resonance frequency. In the metallic VO₂ phase, however, the LC circuit of each SRR is shorted and the array no longer resonates. Although the resonant behavior of the metamaterial can be switched with the phase transition of a VO₂ thin film, this switch is essentially bimodal. In the metallic phase the sample is highly reflecting and behaves like a mirror at IR wavelengths, meaning that the spectral selectivity required for practical applications is not achieved. To overcome this problem, we propose a self-aligned

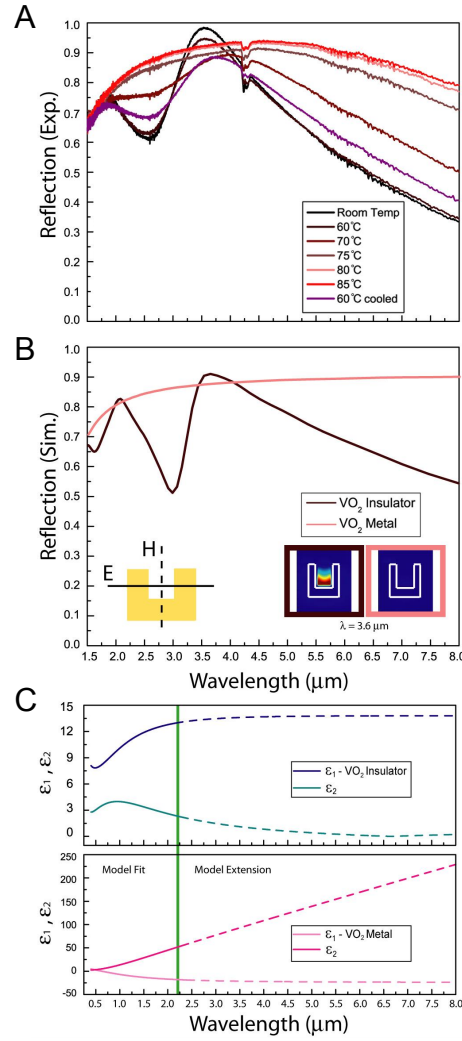


Figure 4.3. A. Reflection spectra of 150 nm thick Ag metamaterial arrays on 60 nm VO₂ thin films. Above the insulator-metal transition temperature of VO₂, the reflection properties of the SRR array are similar to those of a planar metallic VO₂ film. B. Simulated reflection spectra are shown for the structure. Magnetic field intensity, $|H_z|^2$ plots, show the resonance disappear above the VO₂ transition (inset). C. Variable angle spectroscopic ellipsometry is used to model the complex optical constants of VO₂ thin films.

SRR design composed of a stack of Ag and VO₂ layers, whose resonant frequency could be modulated thermally.

4.5 Silver and Vanadium Dioxide Hybrid SRRs

The samples are etched using reactive ion etching to yield self-aligned hybrid-SRR arrays. Figure 4.4A shows experimental reflection spectra for self-aligned Ag/VO₂ SRR structures with dimensions of 450 x 400 nm and 150 nm width SRR arms (inset). The resonant reflection peak is observed at 2.52 μ m, compared to 3.6 μ m before etching. The blueshifting of the metamaterial resonance is a direct effect of replacing much of the underlying high dielectric constant VO₂ substrate with air. Upon heating above the insulator-metal phase transition temperature to 100°C, the resonant reflection response of the new hybrid-SRR structure redshifts by $\Delta\lambda = 100$ nm to 2.62 μ m. A schematic of the self-aligned hybrid-SRR unit cell is shown in Figure 4.2A. Simulations of the metamaterial array show a similar redshift (≈ 100 nm) with an associated overall decrease in the reflection due to the increased absorption in the VO₂ metallic phase (Fig. 4.4B, blue line). However, this result does not agree well with the measurements, as we do not see such a drastic reduction or broadening of the peak intensity.

Additional simulations were performed to investigate the behavior observed in the experiment. The experimental results suggest that the nanostructured VO₂ is not a homogeneous metallic rutile phase, but represents a nanocomposite phase where the semiconductor and metallic phases coexist. Other researchers have reported that the VO₂ phase transition occurs via nanoscale domain switching rather than a bulk homogeneous phase transformation [74], and the phase transition and optical properties of nanoscale VO₂ structures have been shown to differ from those seen in continuous thin films [71]. Given that the actual switching mechanism is likely inhomogeneous for patterned nanoscale structures, and that characterization of the actual domain structure is nontrivial, we employed the simplest model possible that provides good quantitative agreement with experimental observations: we assume that the heated

60 nm thick VO₂ film is a bilayer composed of a 15 nm thick VO₂ film in the metallic phase at the Ag/VO₂ interface and a 45 nm thick VO₂ film in the semiconductor phase at the VO₂/sapphire interface (Fig. 4.4b, light red line). The increase in peak intensity for the bilayer approaches that observed in the experimental data. Based on the experiments and simulations, we conclude that the optical thickness of the VO₂ layer is different than the geometric thickness. It is also important to note that the optical properties of VO₂ films in both phases were only measured up to 2.2 μm . For longer wavelengths, we extrapolated the complex refractive index data by fitting to the optical models previously described (Fig. 4.3C). Error in this extrapolation could lead to incorrect predictions for the wavelengths of interest.

Simulated magnetic and electric field intensity plots ($|H_z|^2$, and $|E_x|^2$) of the self-aligned SRR structure ($\lambda = 2.5 \mu\text{m}$) for both the insulator and metallic VO₂ phases are shown as insets in Figure 4.4B. The resonant behavior is evident in the field profiles. At the resonant wavelengths, the electric field is strongly localized between the edges of the SRR arms due to the circular currents on the SRR. Since VO₂ has higher losses in the metallic phase, the calculated intensities of the magnetic and electric fields are lower compared to those in the insulator phase. When the active material is in the insulator phase, each unit cell of the metamaterial array acts as a 150 nm thick Ag SRR on a 60 nm thick VO₂ substrate. Upon heating above the phase transition temperature, the effective optical thickness of the resonator element changes due to the phase transition, which causes the effective capacitance and inductance of the SRR element to increase and the resonant frequency to decrease. The proposed hybrid metal/VO₂ design is applicable to any resonator element in which the resonant behavior depends on the effective optical thickness.

4.6 Coupled Asymmetric Hybrid SRRs

Frequency selective metamaterial surfaces could be used as modulators, filters, and sensors at IR wavelengths. For practical applications, it is desirable to tune the resonant wavelength by a linewidth of the resonance peak (FWHM). As seen in Fig. 4.4A,

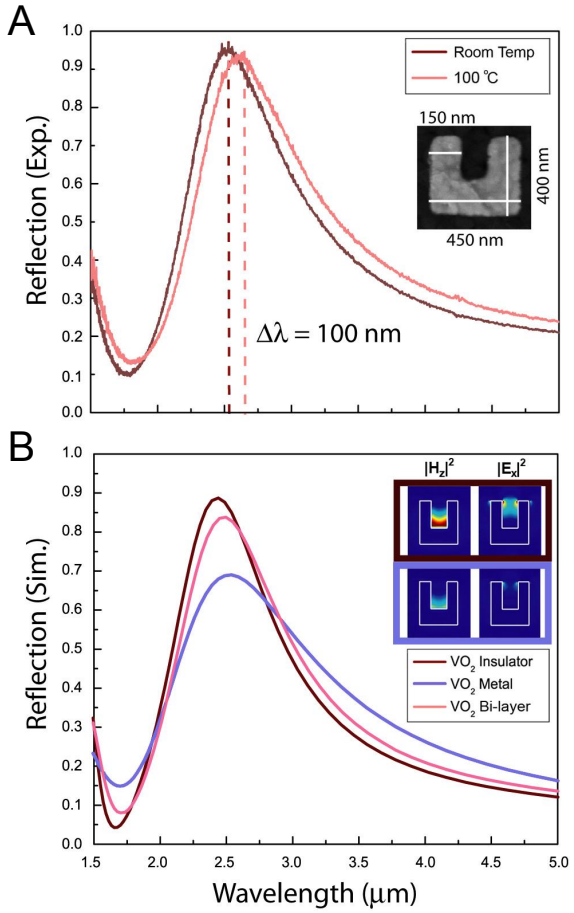


Figure 4.4. A. FTIR reflection spectra of self-aligned 150 nm Ag/60 nm VO₂ hybrid-SRR arrays. The magnetic resonant peak shifts by 100 nm upon heating as the VO₂ undergoes a phase transition. B. FDTD simulations of the self-aligned hybrid-SRR array based on measured VO₂ optical data. A bilayer VO₂ model (15 nm thick metal phase, 45 nm thick insulator phase) is used to predict the experimental results. (Inset) Simulated field intensity profiles ($|H_z|^2$, and $|E_x|^2$) at $\lambda = 2.5 \mu\text{m}$ for hybrid metamaterials show resonances both for insulating and metallic VO₂ phases.

the resonance linewidth of an ordinary SRR array is fairly broad (FWHM $\approx 1.25 \mu\text{m}$) and $\Delta\lambda \approx 100 \text{ nm}$ tuning is relatively small compared to the resonance bandwidth. In order to increase the FOM, the ratio of $\Delta\lambda$ to the FWHM of the resonant peak, one could either increase the wavelength tuning range ($\Delta\lambda$) or decrease the line width of the resonance. Here, we demonstrate spectral line width narrowing of metamaterial resonances by introducing coupled asymmetric SRRs at near-IR wavelengths.

Figure 4.5 shows the experimental reflection spectra for coupled, self-aligned, Ag/VO₂ hybrid-SRR structures in the near-IR range from 1.5 to 5.0 microns. First, a SRR structure coupled to a nearby nanowire (Fig. 4.2B) is investigated (Fig. 4.5A). We observe two resonant reflection peaks, λ_1 and λ_2 , that can be attributed to electrical and magnetic resonances, respectively. Magnetic and electric field intensities in the insulator phase are plotted in the inset. The reflection peak at $\lambda_1 = 1.8 \mu\text{m}$ is due to the electric dipole resonance of the nanowire. The magnetic fields are localized around the nanowire due to the surface current flowing parallel to the nanowire. At the electrical resonance wavelength, simulations predict strong localization of electric fields at the ends of the nanowire. The resonant wavelength, λ_1 , does not change when the VO₂ switches phase. The wavelength of the nanowire dipole electric resonance is determined by the nanowire length and does not depend significantly on the thickness of the metal. The resonant peak at the higher wavelength, $\lambda_2 = 3.0 \mu\text{m}$, is due to the magnetic resonance, as evident by the characteristic magnetic resonance field responses, (i) large magnetic response at the center of SRR and (ii) strong electric field localization at the SRR gap. The magnetic resonance wavelength is red-shifted by $\Delta\lambda_2 = 100 \text{ nm}$ as the VO₂ changes phase from insulator to metal. Introducing nanowires as an additional element to the metamaterial unit cell resulted in narrower resonance peaks than those observed for ordinary SRR arrays. The FWHM of the resonance peaks at 1.8 and 3.0 μm were measured to be 0.5 and 0.7 μm , respectively. The FOM of ordinary SRR array was 0.08, whereas the FOM for the nanowire-coupled SRRs is 0.14, due to the spectral linewidth narrowing of the metamaterial resonance.

Breaking the structural symmetry of metamaterials has been shown to yield narrower metamaterial resonances at microwave frequencies [53]. Coupling a nanowire

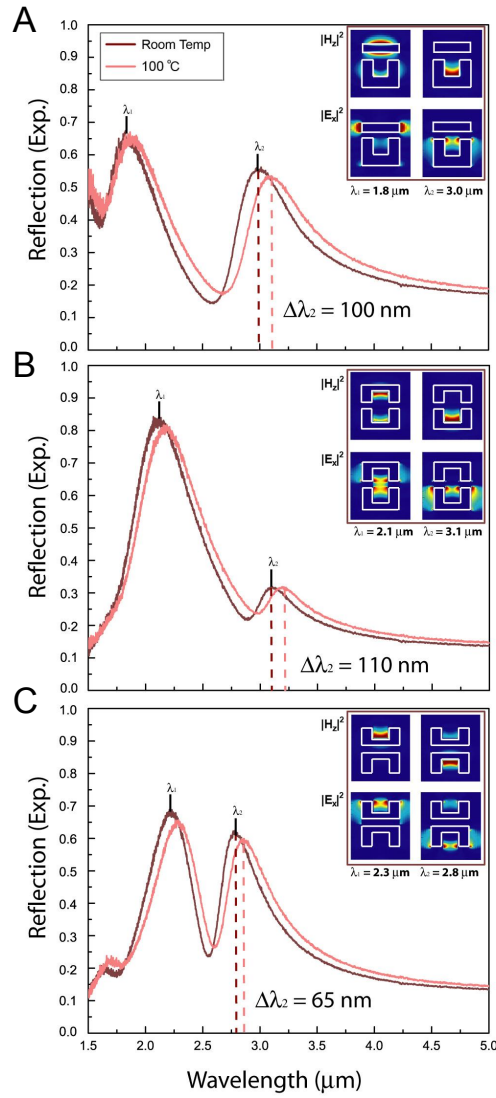


Figure 4.5. Reflection spectra for various geometries above and below the phase transition are shown. A. In the SRR coupled to a bar geometry, the magnetic resonance at $3.0 \mu\text{m}$ is shifted by 100 nm to $3.1 \mu\text{m}$. Simulated field plots (inset) at the resonant wavelengths show $|H_z|^2$ (top) and $|E_x|^2$ (bottom) of the self-aligned structures on insulating VO_2 . B. The resonant peaks for face-to-face coupled structures redshift by 110 nm. C. The magnetic resonant peaks in back-to-back coupled structures shift by 65 nm.

to a single SRR is a way to introduce asymmetry to the resonant elements. Another approach is to couple two SRRs of different sizes (asymmetric SRRs) by properly designing the unit cell. Figure 4.5B shows the reflection spectra of two face-to-face SRRs of different dimensions (Fig. 4.2c) in the insulator and metallic phases. The resonant peaks for these SRRs are $\lambda_1 = 2.1 \text{ } \mu\text{m}$ and $\lambda_2 = 3.1 \text{ } \mu\text{m}$. Simulated field plots (inset) show the signal at λ_1 is due to resonances in both SRRs, whereas the signal at λ_2 is due only to the SRR with longer arms. In the case of coupled SRR arrays, the shorter wavelength response is due to the SRR with shorter arms. The total shift upon phase change in the VO_2 is $\Delta\lambda_2 = 110 \text{ nm}$. Figure 4C shows the reflection spectra for an array of back-to-back coupled SRRs (Fig. 4.2D) with the same dimensions as the face-to-face structures. Coupling the SRRs in this manner narrowed the wavelength separation of the two resonant peaks: λ_1 redshifted by 200 nm to $2.3 \text{ } \mu\text{m}$ and λ_2 blueshifted by 300 nm to $2.8 \text{ } \mu\text{m}$. The change in the magnetic resonant reflection peaks for these coupled structures is $\Delta\lambda_1 = \Delta\lambda_2 = 65 \text{ nm}$. We observed the hybridization of the resonant wavelength of a single SRR, $\lambda = 2.52 \text{ } \mu\text{m}$, to shorter and longer wavelengths, λ_1 and λ_2 . Different coupling schemes resulted in different peak positions in the reflection spectra. The resonant peak shift depends on the coupling strength of resonator elements, and in the case of strong coupling, resonant peaks show larger shifts [62]. Since the electric fields are strongly localized at the gap of SRRs, the coupling of face-to-face SRRs is stronger than back-to-back coupled SRRs. We observed larger resonance wavelength separation in the case of face-to-face SRRs.

4.7 Summary

Metamaterial resonances can be engineered using different coupling and hybridization mechanisms. The three geometries investigated here show reflection resonances of different magnitudes, at wavelengths dependent on the size and degree of coupling between SRRs. In all cases, the magnetic resonance reflection peaks of self-aligned structures redshift as the overall geometry changes with the VO_2 insulator-metal

phase transition. Here, we used a sandwiched VO_2 active layer between an Ag SRR and sapphire substrate, which caused resonant wavelength tuning of ≈ 100 nm. Incorporating VO_2 nanostructures as different resonant metamaterial elements such as the SRR gap or the SRR arms by a two-step electron-beam lithography process could yield better device performances and higher tuning ratios. In this work the phase change was induced thermally simply by heating the metamaterial array, but optical and electrical phase changes are also possible in VO_2 .

In this work, we have demonstrated the first active metamaterial at near-IR wavelengths. Our designs were based on an Ag/ VO_2 stack which allowed us to change the optical geometry of the resonant element with the heat-induced phase transition of VO_2 . Resonance hybridization with additional coupling elements such as nanowires or different size SRRs led to narrower metamaterial resonant peaks and increased the frequency-tuning figure of merit.

4.8 Opportunities

There are a number of directions for future research in this area. The structure that we have demonstrated in some ways represents the simplest structure that can be designed. By exploiting advances in fabrication capabilities, such as direct write e-beam lithography, where sequential writes are aligned to each other, we can envision designing structures where the VO_2 is used to change not only the thickness, but also the shape of the resonator. Relatively simple approaches to this would be extending the length of the resonator arms in order to create a longer inductance loop. We could also imagine designing coupling elements entirely out of VO_2 . In this way, the resonators could transition from uncoupled to coupled states.

An even more exciting opportunity for the design of VO_2 -based metamaterials revolves around recent progress made on Si substrate growth. A parameterized study of the growth parameters required for deposition via PLD on Si substrates was performed. The same conditions described previously for growth on sapphire were used, however the partial pressure of oxygen was increased to 15 mTorr with a substrate

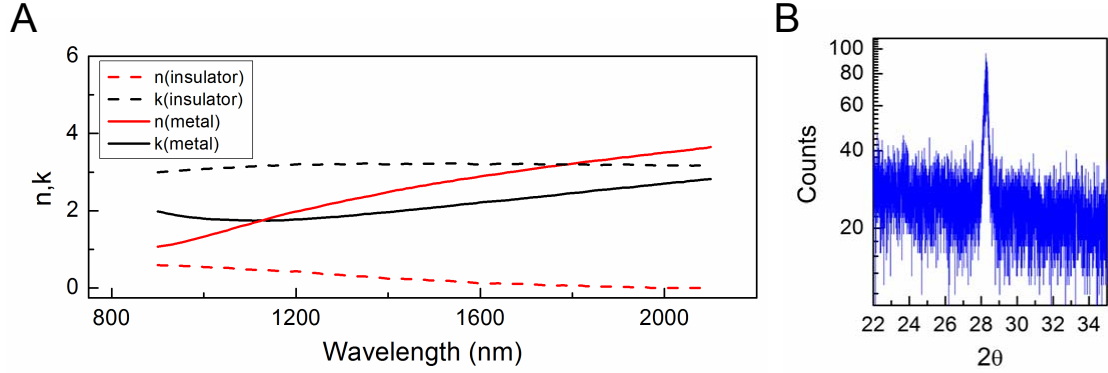


Figure 4.6. The n and κ values for vanadium dioxide grown on Si as measured by variable angle spectroscopic ellipsometry are reported in (A). The XRD for a 65 nm film is shown in (B).

temperature of 500°C. In Fig. 4.6A, we report the VASE data for a representative 65 nm film of VO₂ on Si. The higher values of κ compared to the ellipsometric data for VO₂ grown on Si indicates that though the film switches, it is much lossier than films grown on sapphire. This is expected due to the larger degree of lattice mismatch of VO₂ with Si. While the XRD data prove that only one phase of vanadium oxide was grown (Fig. 4.6B) and are consistent with the peak values reported by other groups, the intensity is very low, corroborating the finding that film quality is not as good as that grown on sapphire. Nevertheless, these films were used to develop and demonstrate a VO₂-based optical modulator [75]. Also, the ability to grow on Si enables contacting the VO₂ and switching the material electrically. Electrical switching of VO₂ occurs on much shorter timescales and could provide the basis for faster, more elegant metamaterial designs.

Chapter 5

Compliant Optical Metamaterials

Electromagnetic metamaterials are composites engineered at the subwavelength scale to have specific optical properties. By carefully designing individual unit cells, behavior that is unattainable in the constituent materials can be demonstrated. Metamaterial designs are typically limited to a narrow operating bandwidth that is predetermined by the fabricated dimensions. In this work, we exploit the mechanical deformability of a highly compliant polymeric substrate to achieve dynamic, tunable resonant frequency shifts of greater than a resonant linewidth. These designs may find application as sensors, optical modulators, and filters.

Metamaterial designs are typically limited to operation over a narrow bandwidth dictated by the resonant linewidth. Here we report a compliant metamaterial with tunability of about 400 nm, which is greater than the resonant linewidth at optical frequencies. This is accomplished using high-strain mechanical deformation of an elastomeric substrate to controllably modify the distance between resonant elements. Using this compliant platform, we demonstrate dynamic surface-enhanced infrared absorption by tuning the metamaterial resonant frequency through a C-H stretch vibrational mode, enhancing the reflection signal by a factor of 180. Manipulation of resonator components is also used to tune and modulate the Fano resonance of a coupled system.

The effect of metamaterial shape on the plastic deformation limit of resonators is investigated. We find that the response is elastic under large global tensile strains when the local strain is evenly distributed. The plastic and elastic limits of resonator deformation are explored and the results indicate that, once deformed, the resonators operate within a new envelope of elastic response. We also demonstrate the use of

coupled resonator systems to add an additional degree of freedom to the frequency tunability and show that compliant substrates can be used as a tool to test coupling strength.

5.1 Introduction

Metamaterials are artificially engineered composites that can exhibit optical responses unattainable in their component materials [1, 2, 76, 77]. The optical response of a metamaterial can be engineered by manipulation of the size, pattern, and composition of its subwavelength unit cells. This response, however, is usually fixed at the time of fabrication yielding materials that are essentially “passive” and operate over a limited bandwidth. The response of otherwise passive metamaterials can be rendered active by integrating dynamic components into the design. Active metamaterials, which seek to tune the resonant frequency range via control of the active medium, represent a new class of designs. To date, amplitude modulation of optical metamaterials, which affects the intensity of the response at the resonant wavelength to create an on/off response, has been achieved via electrical carrier injection in semiconductor substrates [32] and mechanical reorientation of resonant elements using microelectromechanical systems [78]. Frequency tunability has been demonstrated by changing the dielectric environment of the resonator with phase-transition materials [9, 79], liquid crystals [21], and optical pumping of the substrate [33]. Here we take a different approach and exploit the elasticity of a compliant substrate to tune the resonant frequency of a metamaterial in the near-IR by changing the distances and thus the coupling strength between pairs of resonator elements.

Stretchable electronics have recently garnered increasing interest [80], and though mechanical deformation of elastomeric substrates has been used to induce spectral shifts in the resonance of nanophotonic structures such as nanoparticle dimer extinction [81] and gratings [82], the reported tunability range was limited. Our results represent the first demonstration of broad tunability of metamaterials via the elastic and plastic deformation of compliant substrates and, surprisingly, the nanoscale

resonator arrays can be subjected to tensile strains as high as $50 \pm 1\%$ without delamination or distortion of the metallic elements. Although flexible metamaterials have been fabricated to operate at microwave [83] and terahertz [84, 85] frequencies, compliant tuning of metamaterials has not previously been shown. We also demonstrate tunable Fano resonances [56, 57, 86, 87] utilizing the mechanical deformation of compliant dolmen-type resonator arrays.

5.2 Metamaterial Design and Fabrication

The metamaterial structures investigated are planar, coupled split-ring resonator (SRR) arrays in which the resonant frequency depends on the geometry of the SRR and the complex refractive index of the metamaterial substrate. At optical frequencies, U-shaped SRRs have been extensively studied [88, 89] and can be modeled as electrical LC resonators with a resonant frequency of $\omega_0 \sim (LC)^{-1/2}$, where the effective capacitance C depends on the gap size, and the inductance L is proportional to the total effective length of each SRR. This resonant frequency can be altered by changing the geometry of the SRR or by introducing a coupling element, such as a nanowire. This introduces an additional parameter, the coupling constant, which provides further control over the resonant wavelength of metamaterial structures. The coupling constant depends on the distance between the resonator pairs, and we have previously reported that, for passive structures, changing the coupling distance results in a significant shift in the resonant frequency response [88].

In order to examine dynamic modulation of coupling distances, we developed a hard/soft nanolithographic pattern transfer technique and investigated a number of different SRR designs. The schematics in Fig. 5.1 outline this process and show how a representative pattern, an SRR with bar resonator, is transferred to the polydimethylsiloxane (PDMS). The metamaterial arrays are patterned on a sacrificial Si wafer using electron beam lithography. Au is evaporated using electron beam evaporation to create 100 nm thick patterns (Fig. 5.1 Step 1). A bilayer e-beam resist is used to achieve high resolution nanosized features. We also evaporate a 3 nm layer

of Ti to serve as an adhesion layer for the Au to the Si. We found that without the adhesion layer, the patterns can get quite badly damaged or delaminate completely during the lift-off process. Following lift-off in acetone and trichloromethane, the Au is functionalized with a monolayer of 3-mercaptopropyl trimethoxysilane (MPT) under a 50 mTorr vacuum. The MPT creates an Au-S bond at the surface that preferentially binds with PDMS (Fig. 5.1: Step 2). PDMS is cured on top of the patterns at 70°C for 1 hour. A 1:12 ratio of polymer curing agent to prepolymer (Sylgard 184) is used to achieve a highly compliant form of PDMS. Low-bias inductively coupled plasma reactive ion etching (ICP-RIE) with SF₆ is used to selectively remove the Si wafer leaving a free-standing 1 mm thick PDMS substrate with 100 nm thick metallic patterns on top. Figure 5.1A shows an electron micrograph of the pattern on the Si wafer after electron beam patterning. The micrograph in Fig. 5.1C shows the pattern on PDMS after transfer, demonstrating that the nanostructures do not undergo any kind of deterioration in the transfer process. The transfer process is reproducible for a number of designs with nanometer feature sizes and has been replicated for many different samples.

Mechanical deformation of the substrate is used to stretch the resonators apart, changing both the capacitance of the SRR gap and the coupling strength between resonator pairs. A custom-built stage is used to deform the samples and was designed to operate with both a Fourier Transform Infrared (FTIR) spectrometer and an environmental scanning electron microscope (ESEM). The stage is shown in Fig. 5.2. The sample was clamped to the manipulators shown in this picture and then stretched. Figures 5.4A and 5.4B show metamaterial arrays on PDMS before and after stretching, respectively. The ESEM micrograph in Fig. 5.4B shows the extent of deformation observed for a strain of $50 \pm 1\%$ in the y direction. The strain is defined as $(l - l_0)/l_0 \times 100\%$, where l_0 is the initial length of the sample and the error is 1%. Different elements can be coupled to the SRR structure in order to change the operating frequency. Here we show four different samples (Fig. 5.4C with dimensions): SRR-bar, asymmetric coupled SRR (ACSRR), square SRR (sqSRR), and double SRR (DSRR) arrays.

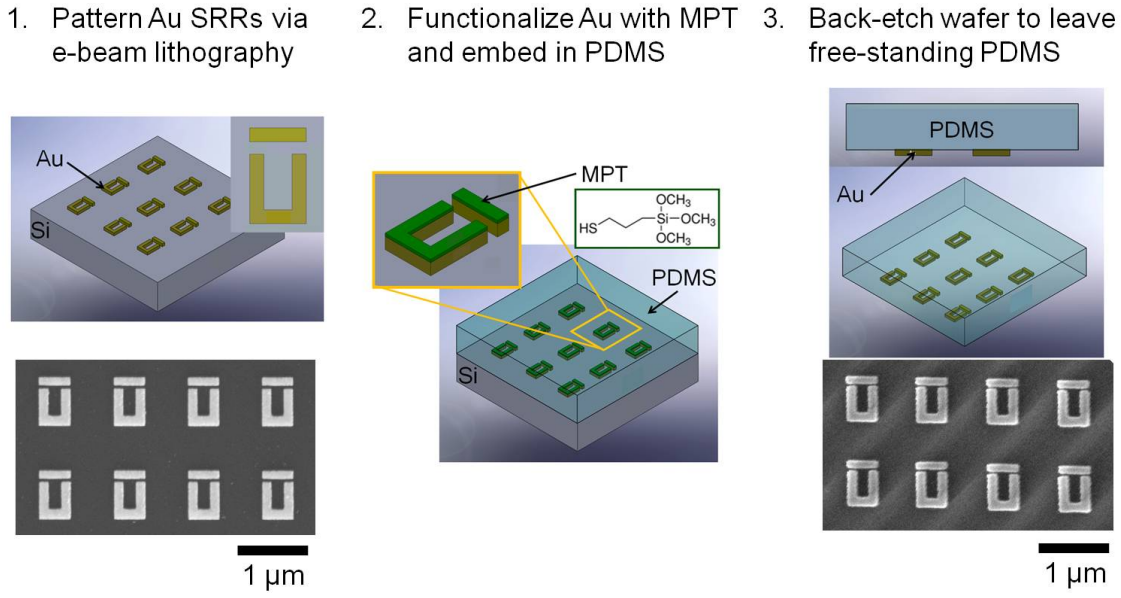


Figure 5.1. The schematic shows the sequence for fabricating compliant metamaterials. The first step illustrates how the SRRs are lithographically patterned on a Si handle wafer. The SRR-nanowire coupled resonator pair is used as an example, but the same approach is followed for all resonator types. The SEM shows the resonators as patterned on Si. The second step shows how the Au is functionalized with MPT and embedded in PDMS. Last, the Si wafer is back etched via reactive ion etching to leave a free-standing PDMS substrate. The SEM in this panel shows the fidelity of the pattern transfer.

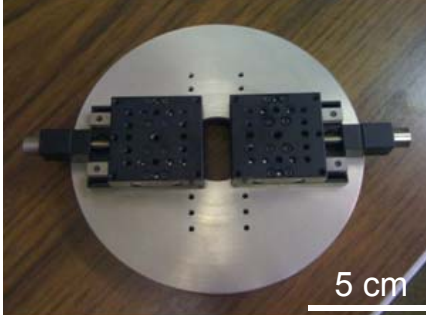


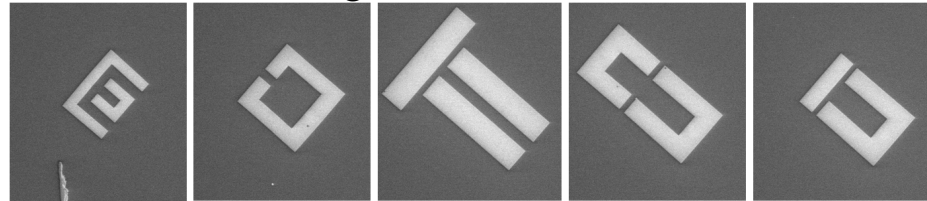
Figure 5.2. The custom-built stage used for compliant metamaterial testing is shown. The manipulators on each side are used to stretch the sample. The bottom plate is made of stainless steel and designed to replace the standard stage used with the FTIR microscope. A smaller stainless steel disc is used with the ESEM microscope (not shown here).

While for nanoscale resonators this transfer process works well and the resonators can sustain high levels of strain, for larger metallic features this does not hold true. In Fig. 5.3, we show ESEM micrographs of larger resonators patterned on the same sample. These resonators are the same shape as the nanoscale resonators described previously, but are much larger as evident from the scale bar. We note that some of the resonators delaminate completely from the surface, while others are significantly deformed. Thus, it seems to be the nanoscale nature of the resonators that enables this approach to both transfer and testing of compliant resonant samples.

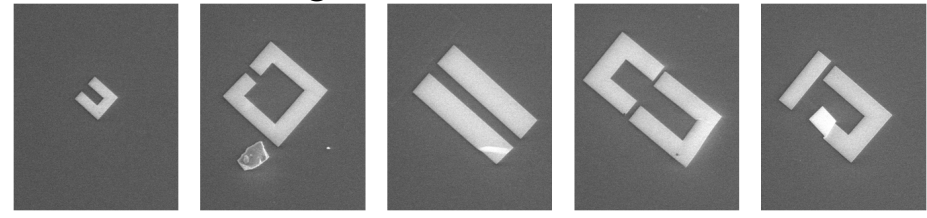
5.3 Basic Uncoupled Split-Ring Resonators

We first investigate basic SRR designs and compare a circular SRR (CSRR) design (Fig. 5.5A) with a square SRR (SSRR) design (Fig. 5.5B). The leftmost panels in (Fig. 5.5) show Fourier Transform Infrared (FTIR) spectroscopic reflection spectra for the two different shaped resonators. The initial resonance for the CSRR is at 5.04 μm (Fig. 5.5A - blue dashed line) and represents the pattern after transfer from the

Before stretching:



After stretching:



50 μm

Figure 5.3. Large SRRs before and after stretching on highly strained substrate.

Si to the PDMS and prior to stretching. Straining the resonators in the direction parallel to the gap causes the gap to decrease and the capacitance to increase. As is evident from the expression for λ_0 , increasing the capacitance will decrease the resonant frequency and redshift the resonant wavelength. For a strain of 10% (solid blue line), the resonance shifts 60 nm to 5.10 μm . The resonators were strained up to 50%, which redshifts the resonance by 140 nm to 5.18 μm . The total path length of the SSRR is shorter than that of the CSRR and, consequently, the initial resonance is at a shorter wavelength. This is indicated by the dashed blue line and occurs at 4.56 μm (Fig. 5.5B). For the SSRR, we find that stretching the structure to a global strain of 10% induces a shift of 60 nm to 4.62 μm , while a strain of 50% shifts the resonance by 140 nm to 4.70 μm .

Although the induced shift in resonance is the same for both of these structures, there is a noticeable difference between the CSRR and the SSRR structures. When the samples are allowed to relax after stretching to 50% strain, the resonance of the CSRR (Fig. 5.5A) moves to a value between the initial resonance and the fully strained resonance, whereas the SSRR resonance remains at the fully strained resonance. In order to better understand the mechanical deformation, the structures

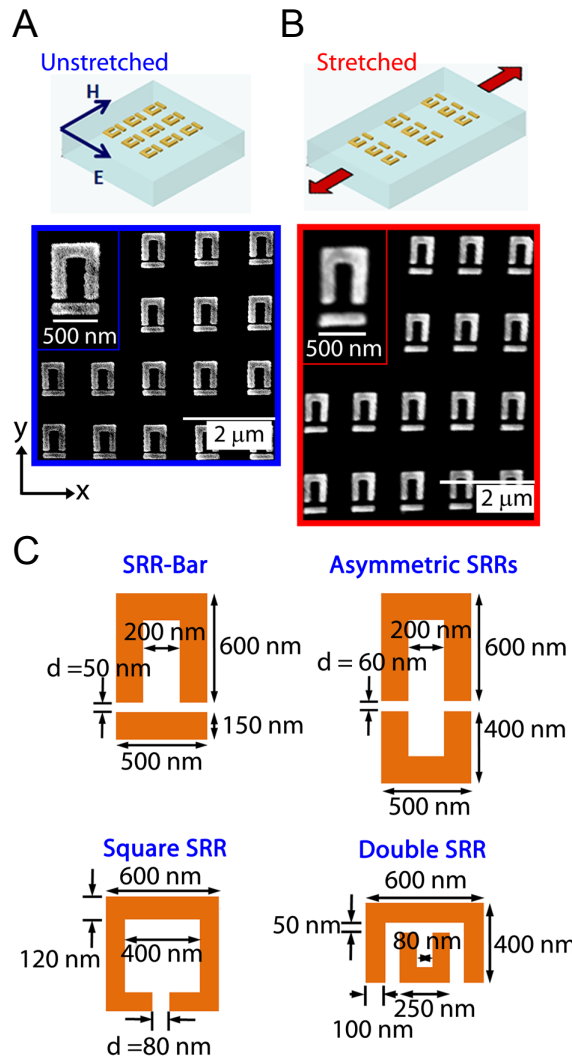


Figure 5.4. A. The top panel is a schematic of the substrate prior to stretching with Au split-ring resonators attached. The polarization of the incident electromagnetic radiation is also indicated. The bottom panel shows environmental scanning electron microscope (ESEM) images of a unit cell and representative array prior to stretching. B. The top panel shows a schematic of a stretched array. The bottom panel is ESEM images corresponding to 50% strain of the array in (a). C. Schematics of each unit cell structure studied with dimensions: SRR-bar, asymmetric SRRs, square SRR, and double SRR structures.

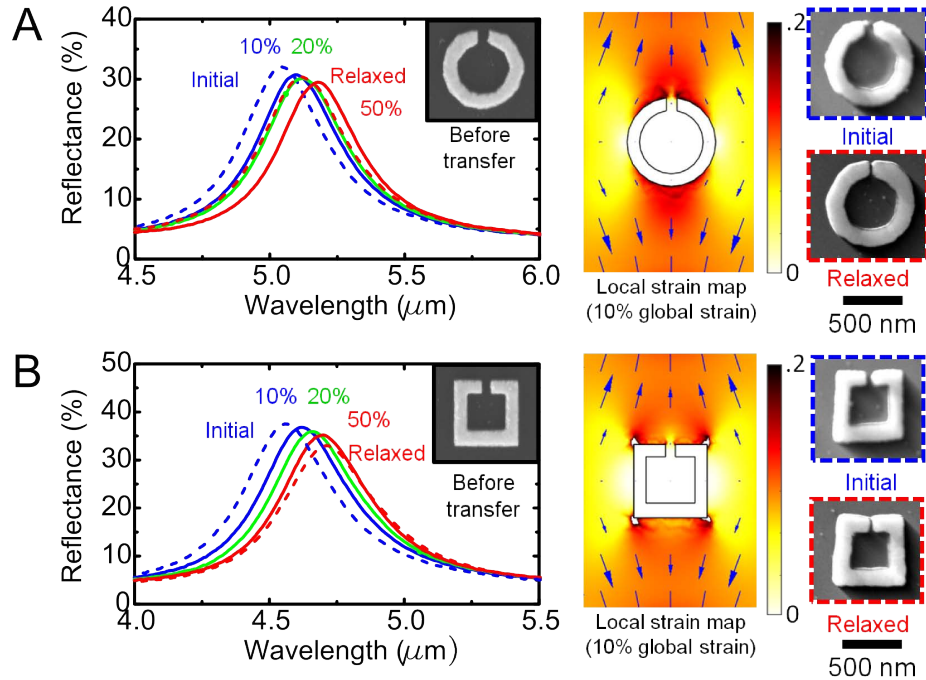


Figure 5.5. A. The leftmost panel shows the FTIR spectra for a circular SRR (CSRR) for strains of up to 50%. The inset of this graph shows the resonator on Si prior to transfer to the PDMS. The solid lines represent the sample with active deformation, while the dotted lines indicate initial and final resonance of the arrays. The center panel of this figure shows the local strain map for a CSRR as calculated using FEM modeling. The color map corresponds to the local strain induced in the resonator, while the arrows indicate actual displacement of the CSRR. The panels on the right show environmental SEM images of a single resonator after transfer (“Initial”) and after mechanical deformation (“Relaxed”). The same data for the square SRR (SSRR) are shown in (B).

were modeled using finite element method (FEM) continuum mechanics calculations. The results of these calculations are shown in the strain maps in both Figs. 5.5A and 5.5B. The colors in the image indicate the local strain induced for 10% global strain, while the arrows show the displacement. It is evident that for the CSRR, the strain is distributed around the outside of the Au, with small regions of high strain concentrated at the gap. The strain on the SSRR, however, is highly localized at the corners of the resonator. This high strain density causes irreversible deformation of the Au-PDMS system upon stretching. These results are corroborated by the environmental SEM images shown in Fig. 5.5. In the case of the CSRR design, the SEM shows that the pattern changes much less dramatically upon transfer to the PDMS. When the sample is relaxed, the gap size decreases, but the shape of the ring is not distorted. For the square ring, the shape is already slightly distorted after transfer to the PDMS and after relaxing, the arms are obviously bowed inwards. Both of these structures are useful for guiding future resonator designs. For designs where an elastic response is important, we would want to ensure that there are no regions of high strain density upon stretching. For designing resonators where deformation is used to permanently tune the resonance to a specific value, regions of high local strain could be exploited to give predetermined resonator shapes.

5.4 Elastic Response of Coupled Resonators

The basic split-ring designs allow control over the capacitance but lead to limited tuning of the resonance. In order to achieve linewidth-scale tunability of the resonant frequency, we introduce another resonator to the system in such a way that the resonators are coupled. By changing the distance between the coupled resonators we can affect the coupling constant, thereby changing the resonant frequency. In Chapter 3, we used passive structures to show that a change in the coupling constant shifts the resonant frequency.

Figure 5.7 shows the dynamic response of arrays of SRR-bar and ACSRR structures, for strains of up to 50%. ESEM images of 4×4 arrays of unit cells are shown for

the initial structures, the samples under 50% strain, and the samples after relaxation (Fig. 5.7A and Fig. 5.7C). The custom-built stage is used to uniaxially stretch the compliant substrate. The coupling distance changes, as does the array period both parallel and perpendicular to the strain axis. The optical response of each sample was measured using FTIR spectroscopy in reflection mode. Although transmission mode would be preferable for characterizing the response, the thickness of the PDMS substrate makes this difficult. Although it is technically transparent in the IR, the numerous absorption features of the C-H vibrational modes make it appear optically thick. Even for thinner, spun cast samples, the vibrational mode signals would seriously affect the ability to resolve the optical response (see 5.6). The reflection spectra for the SRR-bar structures are shown in Fig. 5.7B. We find that the observed resonance shifts are due to changes in coupling between the resonators and that the changing array period has a negligible effect. The spectrum has a reflection peak at $3.65 \mu\text{m}$. The sample was first strained 10% in the y direction resulting in a blueshift of the resonant wavelength by 30 nm. The blueshift of the resonance frequency is due to the reduction in coupling strength when the coupled resonator elements are separated. The sample was then relaxed and the resulting data are coincident with the initial spectral position showing that for up to at least 10% strain the tuning is elastic in nature.

The reflection peaks shown in the data correspond to the hybridized antisymmetric electromagnetic resonance of the unit cell [88]. However, coupled systems composed of asymmetric resonator elements have both symmetric and antisymmetric resonances. Only the antisymmetric resonances are typically reported, as the amount of tuning is larger and more strongly dependent on the coupling distance than for the symmetric resonance. In Fig. 5.8, the wavelength range is extended in order to show how both the symmetric and the antisymmetric mode are affected by the sample strain. In the case of the SRR-bar, the symmetric mode, which is largely due to the nanowire resonance, is almost completely unaffected by changing the coupling distance with the other resonator.

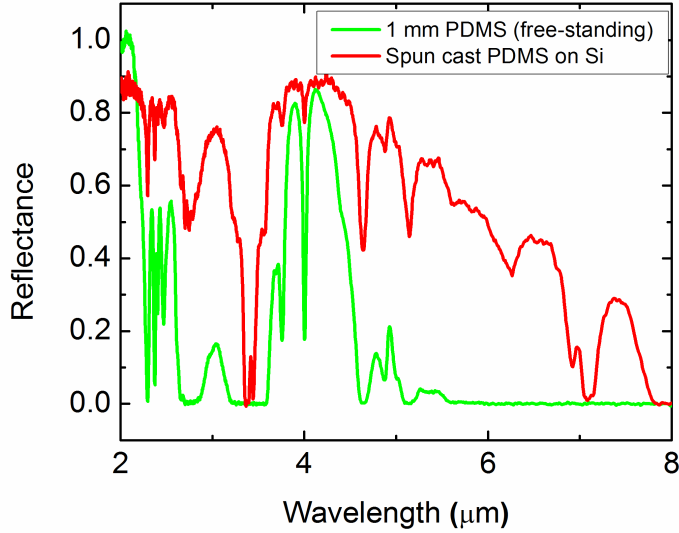


Figure 5.6. This figure shows transmission data for both a thick 1 mm free-standing PDMS sample (green line) and a thinner, spun cast sample on Si (red line).

5.5 Inelastic Response of Coupled Resonators

In the previous section, we explored the limits of elastic tunability, and while elastic tunability of a metamaterial may be desirable, inelastic deformation could prove to be of particular importance for post-fabrication tuning. For tensile strains of 20% and 50%, we observe the reflection peak shift by 80 and 140 nm, respectively. This corresponds to an initial SRR-bar distance of 50 nm and a stretched distance of 56 and 71 nm, as obtained from statistical analysis of ESEM images of arrays. After inducing a tensile strain of 50%, the elastomeric substrate was relaxed. The reflection peak position after relaxation is redshifted by 260 nm from the initial resonant peak, suggesting that the nanowire is closer to the resonator than in the original position. This is corroborated by the ESEM image (Fig. 5.7A), which shows that the SRR-bar coupling distance is now 35 nm due to the permanent plastic deformation of the PDMS. Full field electromagnetic simulations of the reflectance of the metamaterial arrays are shown in Fig. 5.7B and these data agree well with the experimental results.

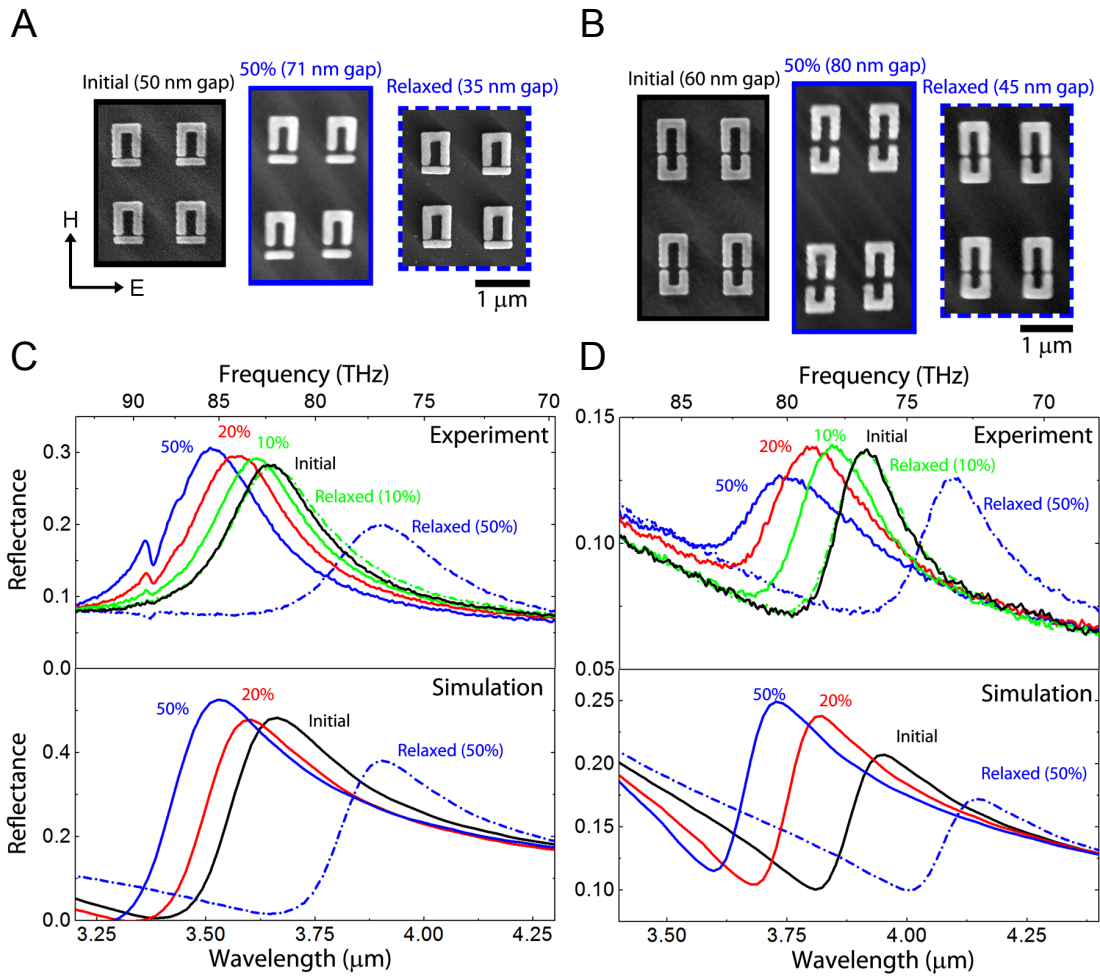


Figure 5.7. A. ESEM images of an array of 2×2 SRR-bar unit cells initially, relaxed, and for 50% strain. The measured gap distances are shown in parentheses. B. ESEM images of an array of 2×2 ACSRR unit cells initially, relaxed, and under 50% strain. C. Experimental FTIR reflectance data for an array of SRR-bar structures with strains of up to 50% are shown in the top panel and simulated reflectance data are shown in the bottom panel. D. Experimental FTIR reflectance data for an array of ACSRRs with strains of up to 50% are shown in the top panel and simulated reflectance data are shown in the bottom panel.

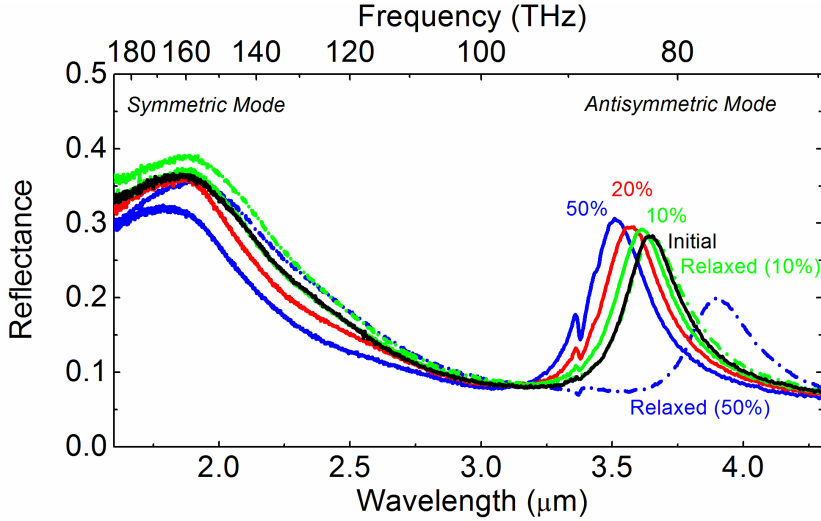


Figure 5.8. The reflectance data for the SRR-bar coupled resonator array. These are the same data as in Fig. 5.7B (Experiment). Here, however, the reported wavelength range is extended to shorter wavelengths in order to show both the symmetric and antisymmetric resonant modes.

The method used to measure the SRR gap width is illustrated in Fig 5.9. The ESEM micrographs for each level of strain are imported into MATLAB. The text is cropped from the bottom of the image and the image is digitized (Fig. 5.9B). A unit cell is selected from the cell, rotated using the base of the SRR and the bar as markers. A line scan in the vertical direction is then used to measure the gap. This is repeated for each unit cell in the image (Fig. 5.9C). The pixel coordinate values are then calibrated to the scale bar in the original image. Gap widths for each degree of strain are reported in Fig. 5.9D.

Changing the geometry of the resonant element from a nanowire to an asymmetric SRR reduces the resonant linewidth, improving tunability. Figure 5.7D shows the reflectance data for the array of ACSRRs. The initial reflection peak position is observed at 3.90 μm for a coupling distance of 60 nm. Elastic tuning was achievable up to 10% and, in this case, the peak was blueshifted 70 nm, double the wavelength shift for the SRR-bar structure. For strains of 20% and 50%, the coupling distance is increased to 72 nm and 85 nm and the resonance is observed at 3.78 and 3.74

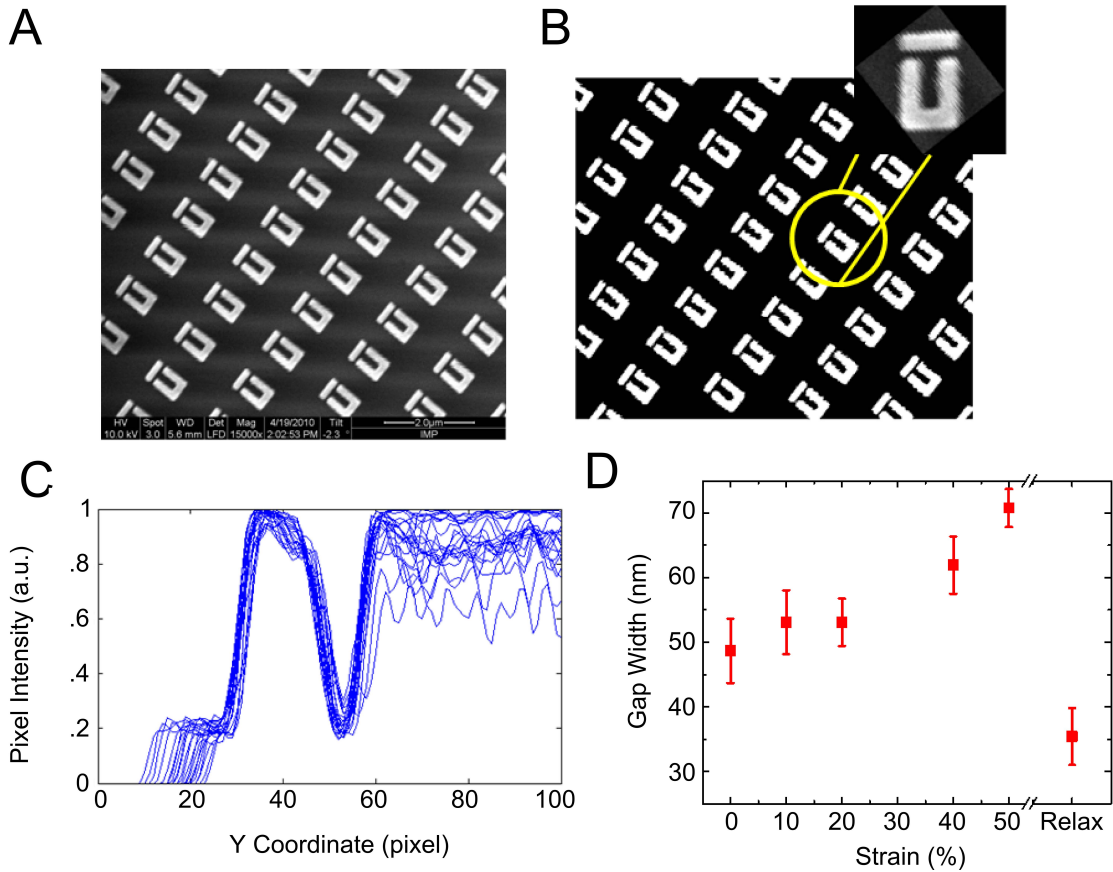


Figure 5.9. This process diagram indicates how gap size is measured for each level of strain. ESEM microscopy is used to image the resonators at each level of strain. A representative raw image (as imported into MATLAB) is shown in (A). The text is cropped and each unit cell is identified and rotated (B). Line scans in the vertical direction are used to determine the number of pixels between the bar and the SRR (C). The pixel size is calibrated to the original scale bar and the widths are averaged over all unit cells of the image. Gap widths for each strain are reported in D.

μm , respectively. After relaxing the sample, the SRRs are closer than in the original sample and the coupling distance was reduced to 45 nm, corresponding to a final resonance position of 4.07 μm . The simulation data for the ACSRR array are shown in the bottom panel of Fig. 5.7D and agree well with the experiment.

Tunability ranges vary for the different arrays, due to the sensitivity of the resonant wavelength shift on the coupling mechanism of the SRR designs. In order to compare the effect of strain on the tunability range for various resonator designs, we define a figure of merit (FOM) of tunability as the resonant wavelength shift, $\Delta\lambda$, divided by the full width at half maximum (FWHM) of the initial reflection peak. The top panels of Figs. 5.10A, B, C and D compare FOM as a function of mechanical strain. We induced tensile strains of up to 50% in the y direction and 25% in the x direction. Finite element modeling (FEM) results showing maps of normalized strain in the top layer of PDMS for each of the four SRR unit cells are displayed in the bottom panels with arrows indicating displacement vectors. For the sqSRR structure (Fig. 5.10A), a maximum FOM of 0.4 for 50% strain is measured. From the FEM simulations of strain, we see that stretching along the y direction brings the arms closer, resulting in a decrease of the sqSRR gap. As a result, the effective capacitance increases, redshifting the resonant wavelength. The converse is true for stretching in the x direction. As previously discussed, with this simple sqSRR design, mechanical tuning can only affect the gap capacitance and linewidth tunability cannot be achieved.

5.6 Achieving Linewidth Tunability

In order to increase the tunability range, more complex designs are necessary. We also explore coupled resonators, such as the DSRR [90] (Fig. 5.10B), for which the FOM can be increased to almost 0.6. Plotting the FOM data shown in Fig. 5.7 for the SRR-bar and the ACSRR structures, we note that increased coupling can indeed yield higher tunability. For the SRR-bar structure, we achieve a maximum FOM of 0.6 for strain applied along the y direction and 0.4 for strain applied along

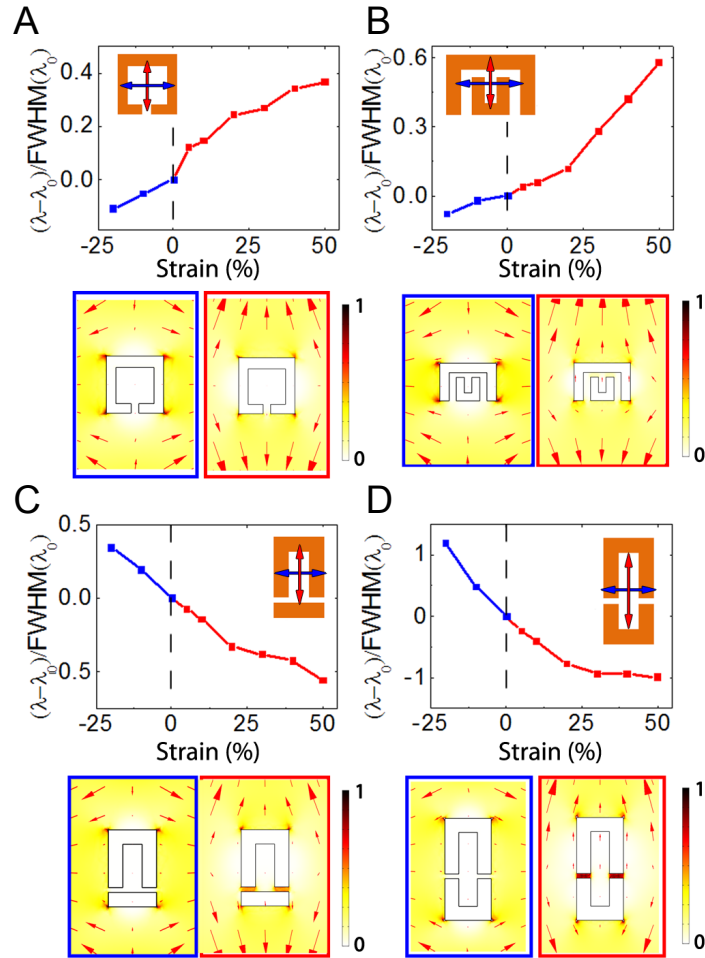


Figure 5.10. The top panel of each figure shows the reflection peak position shift divided by the FWHM of the initial reflection peak for the four different arrays stretched along the primary strain axis (positive tensile strain, shown in red) and the secondary strain axis (negative compressive strain, shown in blue), the square SRR data are shown in A, the double SRR data are shown in B, the SRR-bar data are shown in C, and the asymmetric coupled SRR data are shown in D. The bottom panel of each figure shows the strain density map for perturbations along the primary (red outline) or secondary (blue outline) strain axis. These data are normalized to the maximum for the SRR-bar configuration.

the x direction (Fig. 5.10C). For the ACSRRs, we achieve linewidth tunability by stretching the array in either direction (Fig. 5.10D). Coupled SRRs of differing size yield narrow electromagnetic resonances [53] and thus, the FOM is highest for the ACSRR configuration.

5.6.1 Mechanical Modeling of Compliant Metamaterials

Mechanical modeling for the DSRR shows that as the structure is strained, the arms of the outer SRR bend inwards, increasing the coupling with the inner SRR and, in turn, the FOM. In the case of the SRR-bar and the ACSRR, however, the modeling shows that as the coupling element stretches away from the SRR, the highest region of strain is located in the gap and the displacement vectors show that these structures stretch uniaxially and do not experience bending as in the DSRR or sqSRR structures. This understanding of the nanomechanics provides useful insight for designing coupled resonators at the nanoscale for certain types of deformation and predicting the consequent mechanical and optical behavior. Coupling this with our previous discussion of the effect of shape on resonator deformation, we can begin to conceive of coupled resonator shapes with much larger elastic tuning ranges or plastic deformation that allows particular resonant frequencies to be accessed.

5.7 Sensing with Compliant Metamaterials

Nanophotonic metallic structures, such as plasmonic resonators and metamaterials that enhance the electric fields at the near-field, find applications in spectroscopic techniques such as surface-enhanced infrared absorption (SEIRA) [91, 92, 93] and surface-enhanced Raman scattering (SERS) [94, 95, 96] for biological and chemical sensing [31, 97, 98]. Here, we exploit the mechanical tuning of the electromagnetic resonances of metasurfaces to amplify the signal of an infrared vibrational mode for surface-enhanced reflection spectroscopy. In Fig. 5.11A, the measured reflectance spectra and representative ESEM images for various degrees of strain are shown for the DSRR array. In the reflection spectra of a PDMS substrate without metallic

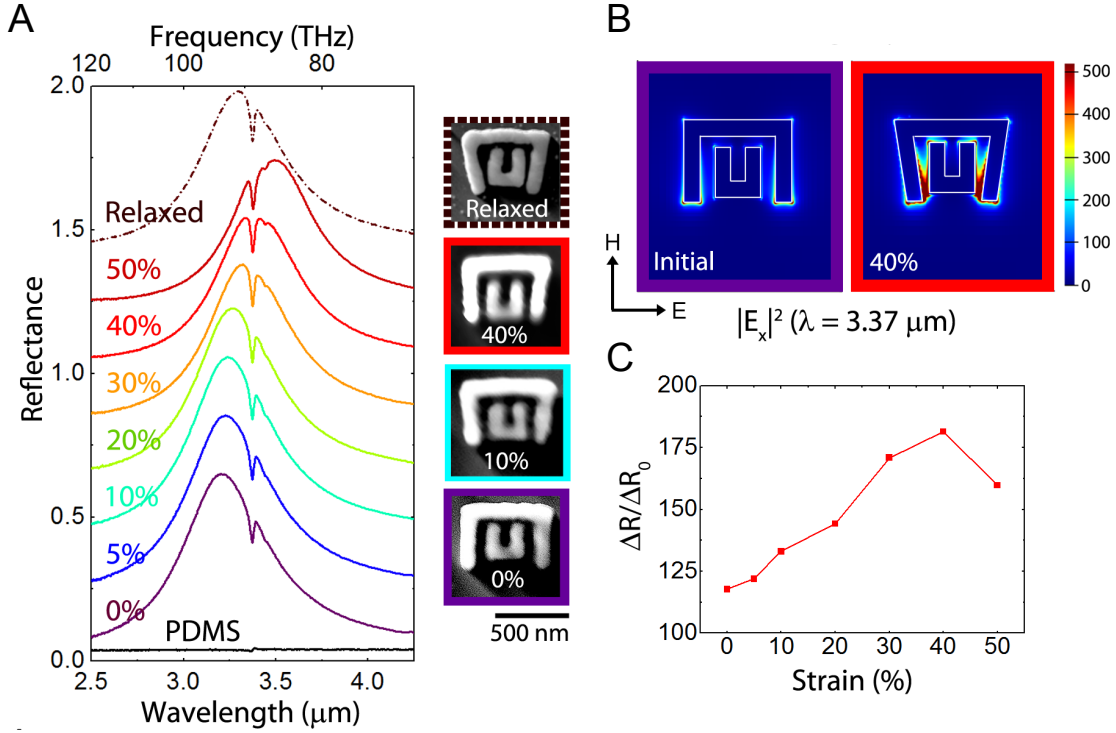


Figure 5.11. A. Experimentally measured spectra for the DSRR structure array for tensile strains of up to 50%. ESEM images of structures initially, under various amounts of strain, and relaxed are shown. B. Electric field intensity plots at the vibrational mode resonant wavelength ($3.37 \mu\text{m}$) for the initial structure and at 40% strain are shown. C. The signal enhancement for the C-H stretch vibrational mode as a function of observed tensile strain is shown.

nanostuctures, we observe a weak absorption feature at $3.37 \mu\text{m}$ which corresponds to the vibrational mode of the C-H stretch bond [99]. Prior to stretching, the resonant wavelength of the metamaterial is $3.21 \mu\text{m}$. We observe a reflection dip associated with the coupling of the metamaterial resonance to the C-H stretch vibrational mode.

By introducing mechanical strains up to 50% we are able to controllably tune the resonant wavelength of the metamaterial through the C-H vibrational absorption at $3.37 \mu\text{m}$. For 40% strain, we find that the peak of the metamaterial resonance is at $3.37 \mu\text{m}$, coincident with the spectral position of the vibrational mode, resulting in increased absorption. Using full-field electromagnetic simulation, we calculate the

total electric field intensities for the initial and 40% strained DSRR at 3.37 μm as shown in Fig. 5.11B. Given that the resonance of the initial DSRR is at a lower wavelength (3.22 μm), the electric field intensity at 3.37 μm is much lower than for the 40% strained DSRR. In Fig. 5.11C, we report the enhancement factor for the signal, $\Delta R/R_0$, which is the ratio of the resonator-enhanced absorption to the absorption from bare PDMS. For a resonator array in unstrained PDMS the enhancement factor is 115, whereas at a strain of 40%, the absorption is enhanced by a factor of 180. We observe a 1.6-fold increase in the reflection signal upon optimizing the strain. The absorption enhancement is attributed to the electric field enhancement in “hot spot” regions between the two resonator legs, and is maximized when the resonance of the metamaterial is matched to the C-H stretch vibrational mode as evident from the electric field intensity plots. Given that the metallic nanostructures are adhered to the surface of the substrate, we assume that the observed reflection signal is coming from a relatively thin layer of PDMS at the metal-substrate interface.

We also explored the possibility of using SRR-bar resonators to achieve resonant enhancement of the vibrational mode at 3.37 μm . The advantage of the SRR-bar system is that more significant tunability can be achieved for smaller amounts of strain. In Fig. 5.12, we revisit the SRR-bar system. The solid red line shows the resonant frequency for an SRR-bar system where the distance between resonators, d , is 110 nm. We patterned three other arrays of nanowire-SRRs with distances of 90 nm (pink line), 70 nm (light blue line), and 50 nm (blue line). The electron micrographs of each of these designs on Si prior to transfer are shown to the right of the FTIR spectra. The dashed lines indicate the shift of the resonant peak with 5% strain. In the case of the $d = 110$ nm system, 5% strain causes no shift in the resonant peak position. As the initial coupling distance decreases, however, the induction of 5% strain does cause a shift in resonance. For the $d = 90$ nm case, the resonance shifts 10 nm and in for the $d = 70$ nm resonator pair, the peak shift is 50 nm. Finally, for the $d = 50$ nm system, the peak shifts by 80 nm from 3.65 to 3.57 μm , a significant fraction of the linewidth.

Figure 5.12B shows a plot of intensity of the reflection dip for each resonator

divided by the reflection dip of the peak for bare PDMS. First, we see that, as each resonator is strained and the enhancement moves from the solid to the dashed line, the enhancement of the absorption feature increases. This is a result of shifting the resonance of the SRR closer to the resonance of the vibrational mode. Additionally, the resonance of the $d = 110$ nm SRR matches the vibrational mode most closely and hence results in over a 200-fold enhancement of the reflection dip before stretching. When this array of resonators is stretched, the enhancement of the absorption feature increases to 225. In previous work, we showed that large strains could be applied to match the resonant frequency and increase the signal strength. In this case, we show how a small amount of strain (5%) can be used to optimize the resonance of a resonator designed to operate at a particular frequency.

Given the *in situ* tuning capability of these types of structure, resonators could be designed to operate over a certain bandwidth and “focus” on peaks at particular frequencies. Mechanically deformable metamaterials could provide a more sensitive, broadband platform for both SEIRA and SERS measurements enabling sensing of low-concentration solutions of chemicals and biological agents, and we will discuss this further in Chapter 6.

5.8 Modulating Fano Resonances with Compliant Metamaterials

We also extend the concept of mechanical tuning of electromagnetic resonances to plasmonic nanocavities. Recently, optical Fano resonances using coupled plasmonic nanostructures have received considerable interest [56, 57, 86, 87]. Here, we study a dolmen-type resonator [56, 57, 61] and demonstrate how mechanical tuning can be used to modulate the Fano response. The dolmen-resonator consists of two plasmonic components: (i) a pair of metal strips with a dark-mode (subradiant) resonance, and; (ii) a monopole antenna exhibiting a bright-mode (superradiant) resonance. Coupling these two resonant elements yields a Fano-type resonance. The experimental data for

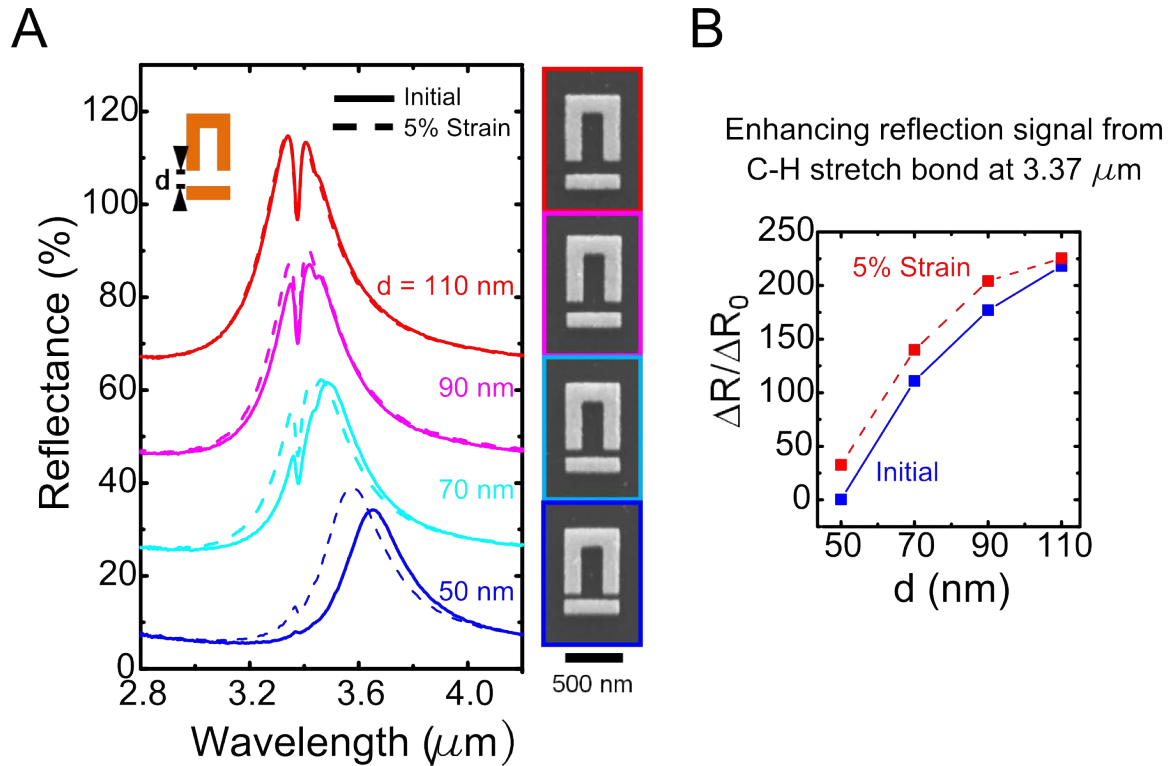


Figure 5.12. A. FTIR spectra for various SRR-nanowire coupled resonator pair arrays are shown. The spacing, d , is varied from $d = 110 \text{ nm}$ (red line) to $d = 50 \text{ nm}$ (blue line). Each dashed line shows how 5% global strain affects the resonant peak position. The SEM images to the right of the FTIR data show the SRR-bar designs on Si prior to transferring to PDMS. B. The change in reflection for the absorption feature corresponding to the vibrational mode of the C-H stretch bond is shown. The change is reported relative to the reflection dip for bare PDMS. The data for both the initial position and the 5% strain resonant peak position are reported.

various strains are shown in Fig. 5.13A. The initial spectrum has distinct resonances at 2.72 and 3.18 μm with a reflection dip at 2.95 μm . When the dolmen-resonator array is strained along the y -direction, the coupling distance, d_y , increases causing a decrease in the coupling strength similar to that observed for the SRR-bar geometry. For 20% strain, we observe that the λ_1 reflection peak blueshifts and the peak amplitude decreases with reduced coupling between the bright and dark modes. We then relax the sample to its original position and the second reflection peak reappears. We repeat the same procedure for 50% strain and note that the second reflection peak becomes almost imperceptible (red line). The dashed red line in Fig. 5.13A shows the measured reflection spectra after relaxation, demonstrating that we are able to recover the Fano resonance after inducing a tensile strain. We observe that the reflection peak positions shift from the original positions due to plastic deformation upon stretching. This results in a decrease of d_y , leading to stronger coupling between resonators in a pair, and is evident in the ESEM image of the relaxed sample.

We use digitized ESEM images of characteristic unit cells to calculate the total electric field intensities using full-field electromagnetic simulation. In Fig. 5b, we plot the electric field intensities for the two reflection peaks, λ_1 and λ_2 , prior to stretching. The electric field is strongly enhanced at the tips of the optical monopole antenna at λ_1 due to the dipole antenna resonance. At 2, the electric field is strongly localized between the optical antenna and the wire pair as a result of strong coupling between these two resonant elements. In Fig. 5.13C, we plot the field intensities for 50% strain at $\lambda_1 = 2.80 \mu\text{m}$ (left) and $\lambda_2 = 3.22 \mu\text{m}$ (right). The coupling distance (d_x) increases, but the distance between the metal wire pair (d_y) decreases, resulting in an enhanced field between the metal wire pair for both resonances. At λ_2 however, the fields are not strongly localized between the wire pair and the optical antenna due to reduced coupling. The field intensity of the relaxed structure (Fig. 5.13D) is similar to the plot for the initial structure; however, the reflection peak positions are shifted to $\lambda_1 = 2.82 \mu\text{m}$ and $\lambda_2 = 3.35 \mu\text{m}$. We note that the λ_2 reflection peak is now aligned with the C-H vibrational mode and this signal is enhanced by a factor of almost 120.

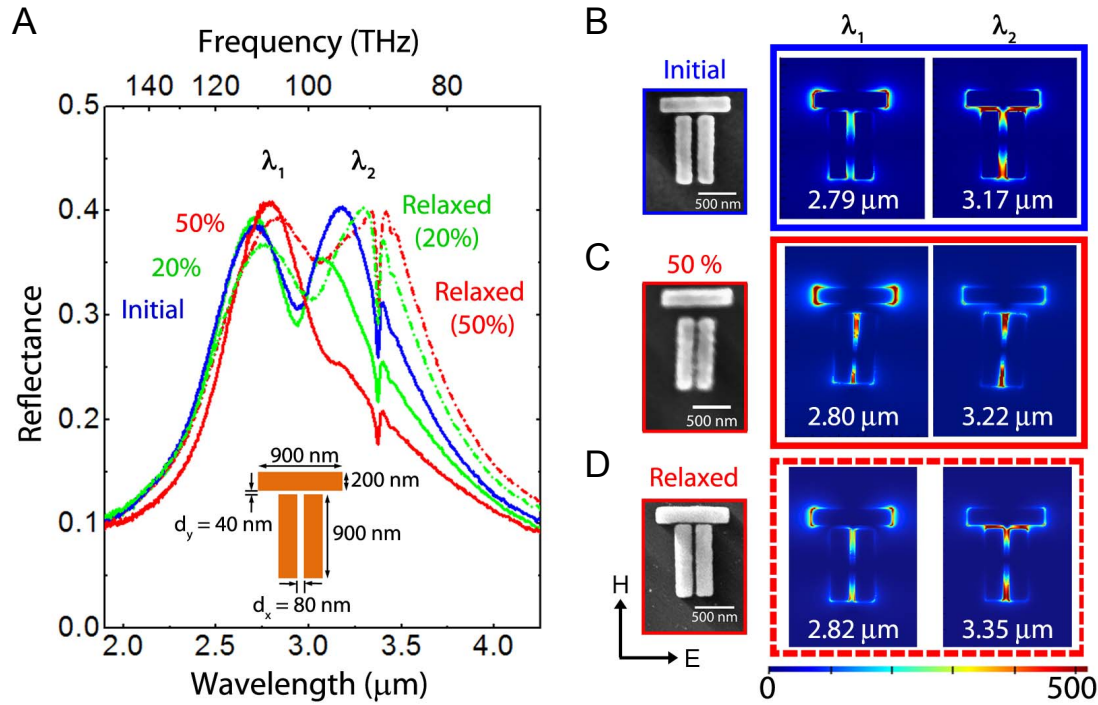


Figure 5.13. A. Experimentally measured spectra of the dolmen-resonator structure for observed strains of up to 50%. The schematic of the dolmen-resonator structure with dimensions is shown as an inset to the graph. B. ESEM image showing the unit cell initially and the electric field density at λ_1 and λ_2 , the two reflection peak positions. C. ESEM image for the unit cell under 50% tensile strain and the corresponding electric field intensity plots at λ_1 and λ_2 . D. ESEM image for the unit cell after relaxation and the corresponding electric field intensity plots at λ_1 and λ_2 .

5.9 Larger Strain and Changes in Elasticity

Full linewidth tunability is an important goal for any active metamaterial as it is critical for a number of applications, including optical filters and modulators. In Figure 5.14A, we demonstrate the effects of larger strain on the $d = 50$ nm SRR-bar coupled resonator system. For a strain of 20%, the resonant peak blueshifts to 3.56 μm from the initial resonance position of 3.64 μm . Instead of relaxing back to the initial resonance, the peak relaxes to a frequency that is further redshifted due to permanent deformation of the PDMS in the gap. Similar behavior occurs for a strain of 50% where the resonant peak shifts to a wavelength of 3.51 μm and then relaxes back to a resonant frequency that is even further redshifted at 3.91 μm . Though the 50% strain resonant peak position is not a full linewidth shift from the initial position, it is a linewidth shift from its relaxed position.

Elasticity of the response is an important criterion for active metamaterials, and we show here, as above, that for strains of more than 10% the samples have an inelastic response. In Figure 5.12B, however, we examine the sample response after deformation to a tensile strain of 50%. In this case, the initial position is the same as the “Relaxed (after 50%)” position in Fig. 5.14A. The resonant peak position shifts to 3.77 μm for a strain of 20%. Of particular interest here is that the sample relaxes back to the initial resonance. Similar behavior is observed when the sample is stretched to 50% strain and the peak blueshifts 330 nm to 3.67 μm , a full linewidth from the initial resonance. These data show that once deformation has been introduced to a sample, there is a new elastic deformation limit. This means that subsequent loading cycles, like that shown in Fig. 5.12B, give information about sample strain history. In addition, it shows that we can initially introduce deformation to achieve an elastically tunable response.

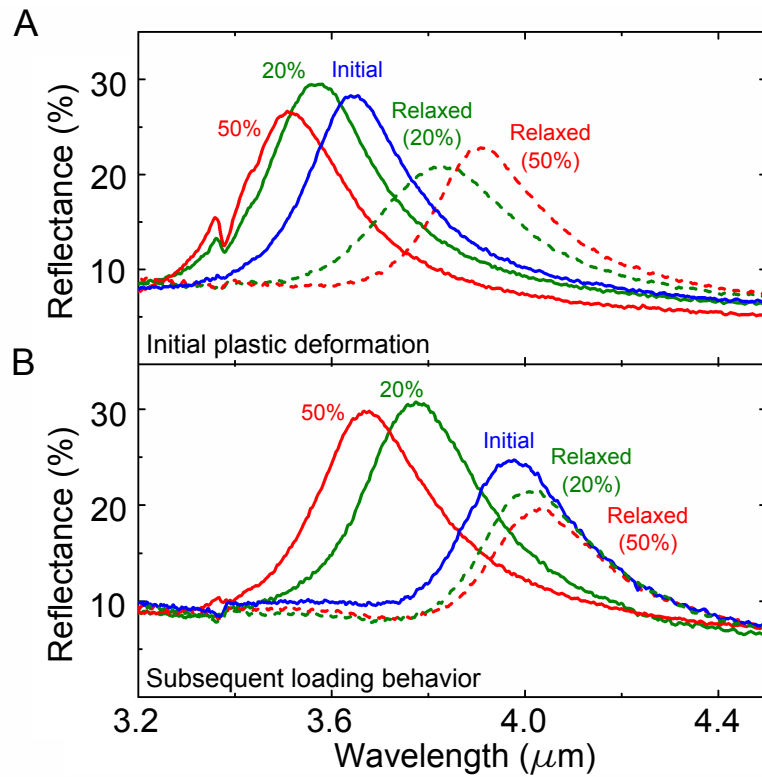


Figure 5.14. A. Initial plastic deformation: FTIR spectra for the $d = 50$ nm SRR-nanowire coupled resonator pair under tensile strains of up to 50% are shown. B. Subsequent loading behavior: FTIR spectra for tensile strains of up to 50% are shown. The corresponding 0% strain positions (“Relaxed (after 20%)” and “Relaxed (after 50%)”) data are shown to demonstrate the elastic nature of the resonator after initial deformation.

5.10 Summary

We have demonstrated large strain mechanical deformation of a compliant metamaterial to achieve resonant frequency tuning by up to a linewidth and have exploited the mechanical control of coupled resonators to dynamically enhance infrared absorption of a molecular vibrational mode, which could provide a new degree of freedom in molecular sensing and detection. We expect that the structures reported here are the first of a new class of highly compliant bendable, stretchable, and tunable metamaterials, signaling a departure from the use of brittle, hard inorganic materials to achieve complex optical material responses.

Chapter 6

Compliant Metamaterials for Sensing

Metamaterials can be designed to operate at frequencies from the visible to the mid-IR making these structures useful for both refractive index sensing and surface-enhanced infrared absorption (SEIRA) spectroscopy. Here we investigate how the mechanical deformation of compliant metamaterials can be used to create new types of tunable sensing surfaces. For split-ring resonator (SRR) based metamaterials on poly-dimethylsiloxane (PDMS), we demonstrate refractive index sensing with figures of merit of up to 10.1. Given the tunability of the resonance of these structures through the infrared, they are well suited for detection of the absorption signal of vibrational modes throughout the “molecular fingerprinting” regime. For split-ring resonators on silicon we find SEIRA enhancement factors on the order of 10^4 . The results highlight the promise of post-fabrication tunable sensors and the potential for integration with microfluidic devices.

6.1 Introduction

The design of nanophotonic sensors has garnered increasing interest as nanoscale fabrication becomes more sophisticated. New fabrication capabilities, advances in nanoscale analysis, and the improved computational power of full field electromagnetic simulations have led to a wealth of new designs based on the surface plasmon resonance of metallic structures. By tuning the geometrical properties of nanoscale features, shapes from crescents to bowtie antennas have achieved increasingly higher electric field enhancements which translate to improved sensitivity [91, 96, 100]. In recent years, optical metamaterials, metallocdielectric composites made up of subwave-

length elements, have emerged as a new class of nanostructured architectures that enable the control and directed emission of light [1, 2, 24]. While nanostructured plasmonic designs exhibit a characteristic electric resonance, metamaterial designs offer an additional magnetic resonance, which is more sensitive to the environment and exhibits a narrower linewidth [4]. This resonance can be tuned from the visible through the infrared by changing the geometry of a characteristic resonator, and the linewidth can be narrowed further by introducing coupling elements to the metamaterial unit cell [88].

A common approach to sensing is to detect small changes in the refractive index of the local environment by measuring the shift in frequency of the local surface plasmon resonance (LSPR) [31, 101, 102, 103, 104, 105]. Plasmonic nanostructures have been used extensively as LSPR detectors since their resonant frequency is highly sensitive to changes in the dielectric constant of their environment. Typical sensitivities are in the hundreds to thousands of nm/RIU or tens to hundreds of meV/RIU with the highest values reported for structures with sharp edges and coupled features with small interparticle gaps [58, 106, 107, 108, 109]. Functionalization of the metallic surfaces can be used to limit binding to specific analytes and this approach has been used to demonstrate a degree of molecular sensitivity [61].

Refractive index sensors cannot rival surface-enhanced spectroscopic techniques, such as surface-enhanced Raman spectroscopy (SERS) and surface-enhanced infrared absorption (SEIRA), which are widely used for sensing particular biological and chemical agents. The sensitivity depends on the high electric field intensities of nanostructured surfaces leading to signal enhancement factors on the order of 108 and 104 for SERS and SEIRA, respectively [91, 92, 93, 94, 95, 96, 97, 98, 110]. Similarly, the most sensitive SERS and SEIRA structures have sharp corners or edges which support significant enhancements to the local electric field intensity, resulting in detection limits on the order of zeptomoles for SEIRA [97] and single-molecule spectroscopy using SERS substrates [111, 112, 113]. SEIRA enhancements are weaker than those anticipated for SERS, as the enhancement depends on $|E|^2$ versus $|E|^4$. This combined with the difficulty of making a substrate that can operate over the entire infrared regime

has led to far less research into SEIRA substrates. Metamaterial designs are well suited to this problem as they can be designed to operate throughout the infrared spectral range and have both sharp edges and strong interfeature coupling required for high enhancement factors. There have been several previous demonstrations of both surface-enhanced and refractive index metamaterial-based sensors in the literature [31, 97, 114]. By building metamaterial-based sensors that operate in the near-to mid-IR, the molecular fingerprinting regime, the narrow magnetic resonance could be exploited to both sense changes in refractive index and to enhance the signal of a particular vibrational mode.

Although metamaterials can be designed to work from the visible to the microwave, the operating frequency is largely fixed by the constituent materials at the time of fabrication. Ideally the response would be tunable *in situ* to operate over a broader bandwidth and cover many different vibrational modes of the analyte. Here, we use a metamaterial system based on coupled split-ring resonators (SRR) adhered to a polymeric substrate, PDMS, to demonstrate precise control over resonant frequency tunability and electric field enhancement. The resonant frequency of an SRR, λ_0 , is described by $\omega_0 \propto LC^{-1/2}$, where L is the inductance and depends on the resonator path length and C is the capacitance across the split in the resonator. By attaching the resonators to a compliant substrate, mechanical deformation can be used to change the capacitance of the gap and the coupling strength between resonators [81, 114]. This can be exploited to achieve up to linewidth tunability of the resonant responses and to customize the resonant response of the metamaterial post-fabrication. Here we present a metamaterial-based sensor that exploits the mechanical deformability of a highly compliant polymeric substrate to both detect small changes in refractive index and resonantly enhance the signal from a broad range of vibrational modes.

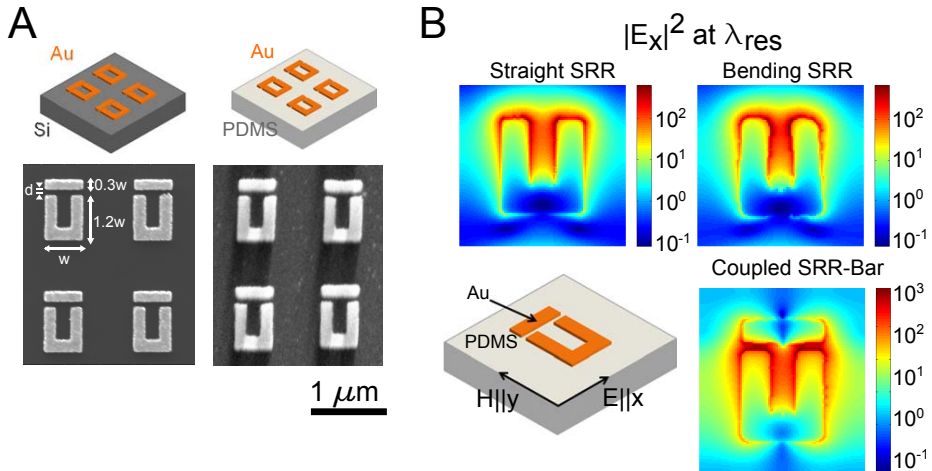


Figure 6.1. A. SEM micrographs of a representative array of split-ring resonators (SRRs) are shown both before and after transfer to the PDMS substrate. The schematics serve as labels to the micrographs. For the structures shown here, $w = 500$ nm, $d = 40$ nm, and the other dimensions scale as indicated with w . B. The electric field intensity is plotted for three different resonator cases, each at their respective resonant frequency. The straight SRR case shows the simulated field for a basic uncoupled SRR. The bending SRR case includes the deformation of the SRR arms when the resonators are attached to a compliant substrate. The bottom right panel shows the coupled SRR-bar system and the schematic in the bottom left shows the electric field polarization relative to an individual resonator.

6.2 Enhanced Local Electric Field for Metamaterial-Based Sensing

The sensitivity of both refractive index sensors and surface-enhanced spectroscopic techniques depends critically on the intensity of the local electric field. We have previously shown that designing coupled resonator structures greatly enhances the local field at the resonant frequency, in a manner similar to the hybridization of plasmonic nanostructures [88]. Thus, we start our discussion with an analysis of the anticipated field enhancements for coupled resonators. The resonator geometries that we choose to utilize in this work are 100 nm thick Au SRRs coupled to Au bars (SRR-bar) on a PDMS substrate. As discussed in previous work [114], the metamaterials are fabricated by patterning Au resonators on a Si handle wafer (Fig. 6.1A) and then transferring the patterns to a PDMS substrate using a hard/soft nanolithographic pattern transfer process. The SEM micrograph of the structures on PDMS (Fig. 6.1A - right panel) shows the fidelity of the pattern transfer process for a representative array of SRRs with a resonator width (w) of 500 nm and a coupling distance (d) of 40 nm.

The electric field intensity for three different resonators on PDMS is calculated via full field electromagnetic simulation at their respective resonant frequencies with the electric field polarized perpendicular to the resonator arms (Fig. 6.1B). In the top left panel, we show the electric field plot for an SRR with straight arms. This simulation uses the measured geometry of a resonator on Si as determined from SEM micrographs of the patterned Au. When uncoupled resonators are transferred to the PDMS substrate, however, the stress in the PDMS causes the arms to bend inwards slightly. This bending causes an increase in the electric field intensity at the tips of the SRR, as made evident by the top right panel of Fig. 6.1B, which increases the sensitivity of these structures compared to straight SRRs. In the bottom right panel, the coupled SRR-bar case is plotted. The coupling in this unit cell increases the maximum field intensity by an order of magnitude from the uncoupled case. Coupling resonators together in a metamaterial unit cell is thus critical to the design of highly

sensitive sensors or to any application that requires locally enhanced electromagnetic fields.

6.3 Refractive Index Sensing with Compliant Metamaterials

In order to further test the idea of using metamaterials as refractive index sensors, we consider first the SRR geometry shown in Figure 6.1. We use FTIR spectroscopy to measure the reflectance of the arrays across the IR spectrum. The samples are measured between $\lambda = 1.5$ and $8 \mu\text{m}$ in a Fourier Transform Infrared (FTIR) microscope equipped with a liquid nitrogen-cooled MCT detector. The measurements are taken in reflection mode at normal incidence and are the result of the coaddition of 64 scans with a 1.928 cm^{-1} resolution. A CaF_2 polarizer is placed in the incident beam path and a KBr beamsplitter is used for all measurements. The reflectance data are normalized to a gold standard. The experimentally measured spectra for both an uncoupled SRR and a coupled SRR-bar with $d = 40 \text{ nm}$ are shown in Figure 6.2A. For clarity, we limit the width of the graph to the region where the magnetic resonant peak is located. We note that the electric resonance of the material is blueshifted from this peak. The resonance of the uncoupled SRR on PDMS in an ambient environment is $3.14 \mu\text{m}$, and coupling to a bar shifts the resonant frequency to $3.42 \mu\text{m}$ (Fig. 6.2A). In order to determine the sensitivity of the arrays as refractive index sensors, the reflection spectra were measured in three different index-matching fluids with refractive indices of 1.47, 1.54, and 1.61. The resonant frequency of the array is highly dependent on the dielectric constant of the surrounding environment, and increases cause the resonance to red-shift due to the increase in effective capacitance of the split gap. The resonance shifts from $4.37 \mu\text{m}$ in the $n = 1.47$ index-matching fluid to $4.61 \mu\text{m}$ in the $n = 1.61$ index-matching fluid. This represents a shift in the resonant wavelength, λ_{res} , from the initial measurement in air of 1.23 and $1.47 \mu\text{m}$, respectively. The resonant peak shifts are more dramatic for the $d = 40 \text{ nm}$ coupled

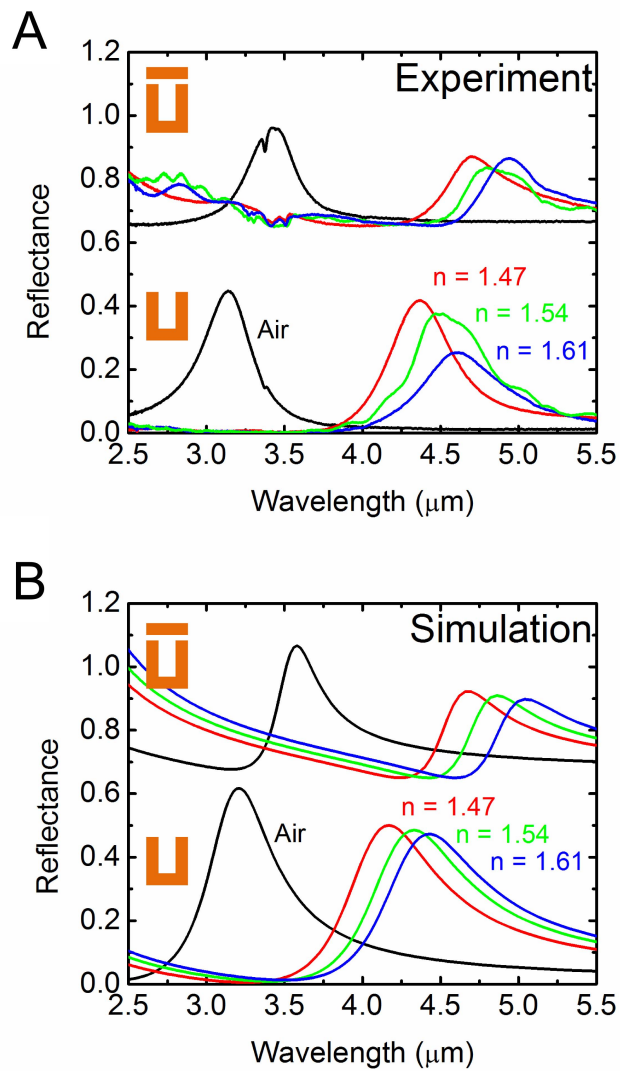


Figure 6.2. A. Experimentally measured FTIR reflection spectra for representative arrays are shown. The bottom set of data is for an array of uncoupled resonators in air and three different optical matching fluids. The index of the fluids used is indicated in the plot. The coupled data are for an array of SRR-bar resonators with a coupling distance of 40 nm. The response for uncoupled and coupled arrays is also simulated and these data are shown in (B).

resonator case, where the resonance is $4.71\text{ }\mu\text{m}$ in the $n = 1.47$ index-matching fluid and $4.94\text{ }\mu\text{m}$ in the $n = 1.61$ index-matching fluid, a redshift of 1.28 and $1.51\text{ }\mu\text{m}$, respectively. The simulated data for these resonator arrays are shown in Figure 6.2B. The uncoupled resonator data shown takes into account the resonator bending described previously and enables a much better fit to the experimentally obtained values than the straight SRR case, which is not shown here. The full-field electromagnetic wave simulations shown here were performed using Lumerical, a commercially available finite-difference time-domain (FDTD) simulation software. A unit cell of the investigated structure was simulated using periodic boundary conditions along the x and y axes and perfectly matched layers along the propagation of electromagnetic waves (z axis). A broadband plane wave was propagated incident on the unit cell along the $+z$ direction, and reflection was monitored by a power monitor that was placed behind the radiation source to emulate the actual experiment. Electric fields were monitored with frequency profile monitors. The optical constants for Au were taken from Palik and a constant refractive index of 1.2 was used for the PDMS.

From the reflectance data, we can calculate the sensitivities of the resonator arrays, defined as the change in resonant frequency as a function of change in refractive index in units of nm/RIU. The sensitivity is then divided by the full width at half maximum (FWHM) of the resonant peak in an ambient environment to determine the figure of merit (FOM) of the resonator array [115]. We report FOM values for two different unit cell width geometries: $w = 500$ and 220 nm . A representative SEM micrograph of a 4×4 array of resonators on PDMS is shown (Fig. 6.3A and 6.3D). For the larger, $w = 500\text{ nm}$, resonator array we calculate FOM values of up to 8.9 for a coupling distance of $d = 40\text{ nm}$ and a slightly lower value of 8.2 for a coupling distance of 55 nm . The unfilled data point in Fig. 6.3B where $d = 500\text{ nm}$ refers to the uncoupled resonator case. These data can be fit to an exponential decay curve, allowing us to predict the FOM for smaller coupling distances. Figure 6.3C shows corresponding simulation data for a number of different coupling distances and we calculate FOM values of 6.0 and 5.4 for coupling distances of 40 and 60 nm , respectively. We attribute the lower FOM values to the broadening of the resonant

peaks in simulation as evident in Fig. 6.2B. We simulate the SRR with both straight arms and with bending arms as previously described, and we find that the enhanced local field of the SRR while bending leads to an increase in the FOM from 3.3 to 3.7. The FOM values for the smaller resonator are higher than those reported for the larger unit cell, with values of 10.1 for a coupling distance of 30 nm and 9.3 for a coupling distance of 40 nm (Fig. 6.3B). As in Fig. 6.3A, we plot the FOM value of 8.5 for the uncoupled resonator at a coupling distance equal to the resonator width of 220 nm and the line represents an exponential decay fit to the data. The simulated values are also reported for a number of points and we compute a FOM of 8.9 for $d = 40$ nm, 8.3 for $d = 60$ nm, and 7.1 for the uncoupled, bent SRR case.

Reducing the coupling distance between resonators leads to higher FOM as a result of the higher local electric field for both resonator sizes. In addition, we find that the FOM value will always be higher for a coupled resonator as the presence of the bar narrows the resonant peak. We attribute part of the discrepancy between simulation and experiment to inaccurate modeling of the SRRs on PDMS and assume that the average degree of bending of the SRR arms is actually higher for the ensemble than that predicted by the single SRR unit cell used in simulation. It is also possible that the SRR arms bend inwards when coupled to bar, and this could also contribute differences for larger coupling distances where the stress is not offset by the bar. Nevertheless, these FOM data represent the highest values reported for nanostructures in the IR compared to previous reports of 3.9 for Au structures [31]. This design is rivaled only by a three-dimensional double nanopillar structure which has a FOM of 23 at a resonant wavelength of 1368 nm [107].

We summarize our experimental results in Table 6.1 and find that the highest FOM values can be engineered for the smallest coupling distances and the smallest resonator sizes. On the other hand, large SRRs are capable of achieving much higher sensitivity values (nm/RIU). This is also evident in Figure 6.4, where we have plotted the sensitivity in nm/RIU as a function of resonator width and coupling distance. In this series of simulations, we varied the coupling distance for three different resonator widths, $w = 300, 500$, and 800 nm. We found that the values of sensitivity could

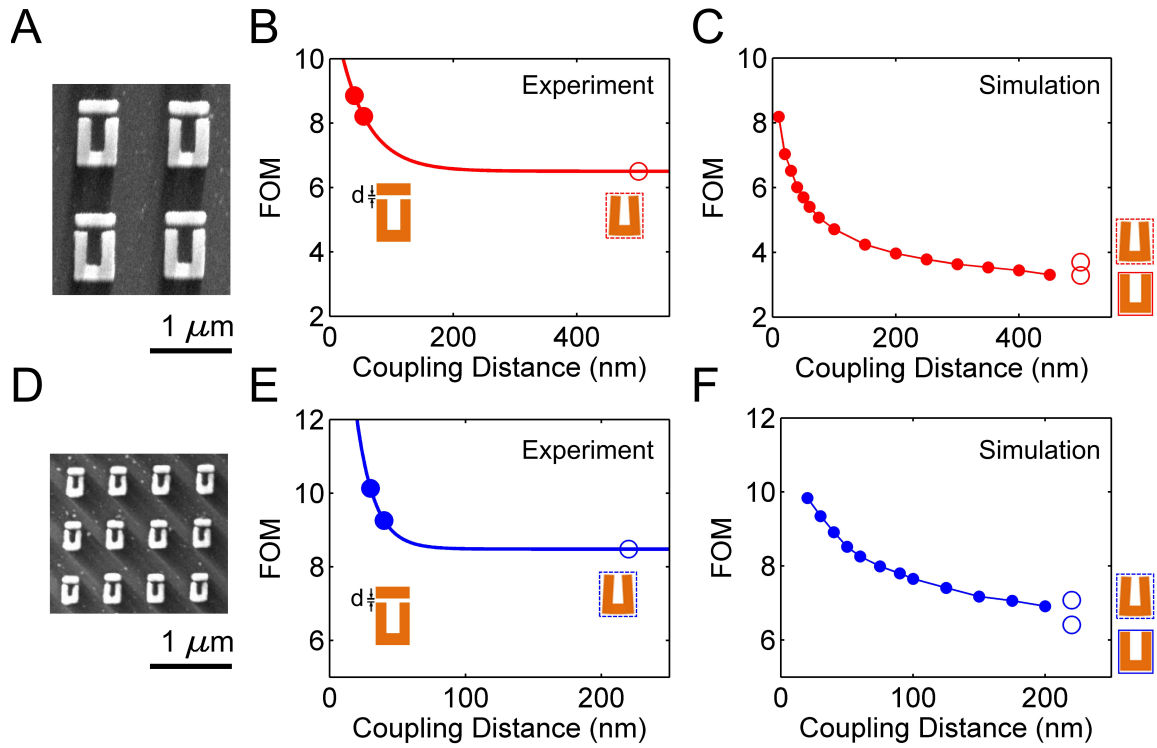


Figure 6.3. A. Experimentally determined figure of merit (FOM) values of resonators with $w = 500$ nm are plotted. The FOM is the sensitivity in terms of nm/RIU divided by the full width at half maximum (FWHM) of the resonant peak in air. The unfilled data point at a coupling distance of 500 nm refers to the uncoupled SRR, i.e., without a bar. C. Simulated data for the same resonators is plotted. Two different uncoupled resonator cases are simulated: the “straight SRR” and “bending SRR.” The same data for smaller resonators are shown in (D-F). Here, the uncoupled distance is equal to the width of the resonator, 220 nm.

Table 6.1. Sensitivity and figure-of-merit values for different sizes of coupled and uncoupled resonators

Structure	w (nm)	d (nm)	λ_{res} (μ m)	Sensitivity (nm/RIU)	Sensitivity (meV/RIU)	FWHM (nm)	FOM
SRR	220	-	1.42	1192	497	141	8.5
SRR-bar	220	40	1.45	1225	488	121	10.1
SRR	500	-	3.14	2480	216	381	6.5
SRR-bar	500	40	3.33	2546	190	286	8.9
SRR	800	-	5.09	3366	116	521	6.5

be fit to exponential decay curves and the values of these curves are interpolated in the figure. One of the key features of this approach in general is that resonators can be designed to span a broad spectrum of operating frequency, figure-of-merit values, and sensitivity and sensors can be selected and designed based on specific needs. We report the resonant wavelength of the structures on PDMS in an ambient environment for a number of different sized resonators in addition to their sensitivities and FOM values in Table 6.1. The sensitivity in units of eV/RIU is also reported for comparison with other sensor geometries in the literature. The wide distribution of resonance values shows that resonators can be designed to work through most of the IR with limits being imposed, not by the fabrication technique or design stipulations, but rather by the characterization techniques available. For instance, the 800 nm SRR-bar geometry is not included in Table 6.1 because the resonance is red-shifted out of the range of the detector.

6.4 Compliant Metamaterials for Surface-Enhanced Spectroscopy

The ability to tune the response of these resonators either through fabrication or with in situ dynamic components is also of interest for surface-enhanced spectroscopic tech-

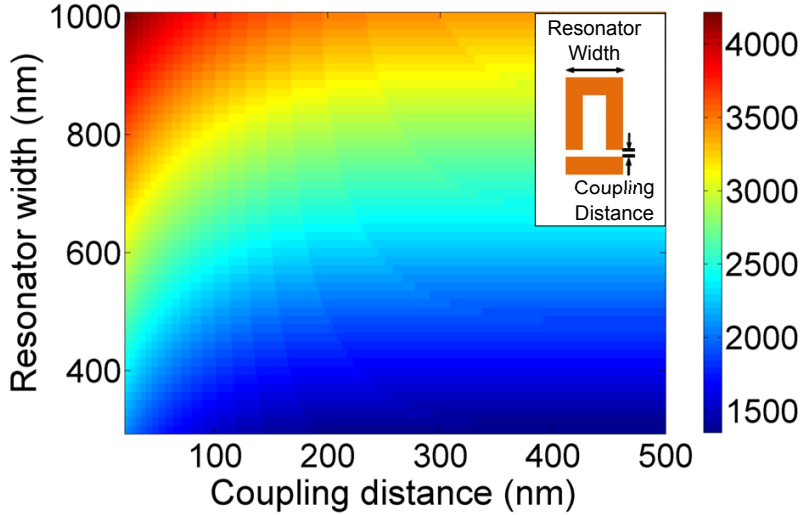


Figure 6.4. Sensitivity as a function of coupling distance and resonator width. The inset is a resonator showing the relevant dimensions.

niques, where alignment to particular vibrational modes is crucial for enhancement of the molecular signal. For example, the dips in the experimental data in Fig. 6.2A for the coupled resonator in air case (black line) near $3.3 \mu\text{m}$ are due to an overlap of the metamaterial resonance with the vibrational modes of the symmetric and antisymmetric C-H stretch bonds in the PDMS. The notch in the uncoupled resonator in air peak is also due to these modes. In this work, we focus our attention on the IR absorption signals from the vibrational modes of *p*-mercaptoaniline (*p*MA) and show how they can be enhanced using coupled SRR-bar nanostructures.

6.4.1 Static Structures for Surface-Enhanced Spectroscopy

First, we use arrays of coupled Au SRR-bar resonators on Si with unit cell widths of 500 nm and coupling distances from 40 to 140 nm. This static structure emulates the behavior that can be induced mechanically by attaching the resonators to a compliant substrate as the resonant frequency shifts from 6.0 to 6.3 μm over this range of coupling distances. The surface of the coupled resonators is functionalized with a monolayer of *p*MA by leaving the sample in a 10 mM ethanolic solution overnight.

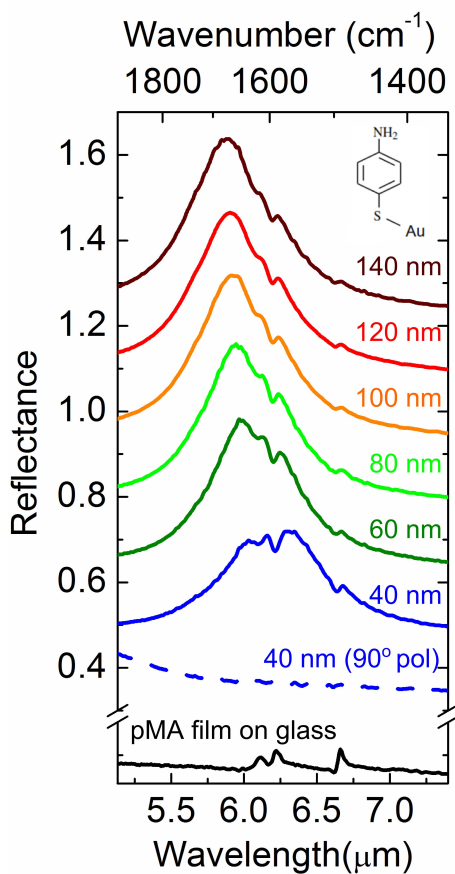


Figure 6.5. FTIR reflection spectra data are shown for arrays of resonators on Si. The coupling distance is indicated in the labels. The dotted line shows cross-polarized data for the array at 40 nm coupling distance. The black line is the spectrum for an 800 nm thick film of *p*MA on glass. The structure of the *p*MA molecule is shown as an inset to the figure. The data are offset for clarity.

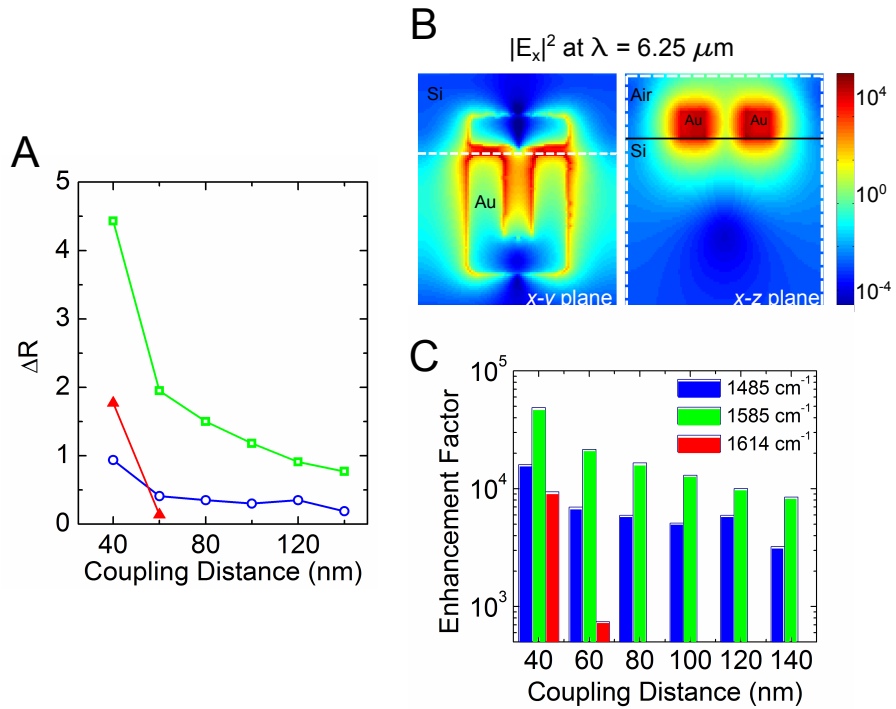


Figure 6.6. A. Change in reflection, ΔR , for each vibrational mode as a function of coupling distance. B. Electric field intensity at the resonant wavelength ($\lambda_{res} = 6.25 \mu\text{m}$) for the 40 nm coupled resonator system is plotted. The simulated data for both the xy plane (left) and the xz plane (right) are shown. The xz plane is taken at the point indicated by the dotted line on the xy plane panel. C. The enhancement factor values for each vibrational mode signal are graphed as a function of coupling distance.

Table 6.2. IR Peak Assignments of *p*MA

(ν stands for stretch and δ stands for bend)		
Peak	Wavenumber (cm ⁻¹)	Assignment
(a)	1485	νCC + δCH
(b)	1585	νCC
(c)	1614	δNH

The thiol group on the *p*MA binds preferentially to the Au and a monolayer is formed. The sample is then thoroughly rinsed with ethanol prior to measuring to ensure that only a monolayer remains bound to the surface of the Au. The reflectance spectra after *p*MA functionalization are reported for each coupling distance (Fig. 6.6A). We identify three peaks in the data corresponding to the δN-H mode at 6.20 μm (1614 cm⁻¹), the νC-C mode at 6.31 μm (1585 cm⁻¹), and the νC-C and δC-H vibrational modes at 6.73 μm (1485 cm⁻¹) (Ref. [93]), as indicated in Table 6.2. As the coupling distance changes, the resonant peak shifts through these frequencies and the overlap of the metamaterial resonance with each vibrational mode results in pronounced dips in the reflection spectra.

The enhancement of the vibrational mode signals can be calculated relative to an 800 nm thick reference film of *p*MA (Fig. 6.6A black line) and is dependent on the local field enhancement at the resonant peak. We first quantify the dip in the reflection spectra as the difference, ΔR_{SRR} , between the maximum and the minimum value of reflectance at each vibrational frequency (Fig. 6.6). We find maxima of 4.5% for the C-C stretch bond at 1585 cm⁻¹, 1.7% for the N-H delta mode, and 1% for the mode at 1485 cm⁻¹. In order to confirm that the observed signals are due to enhanced electromagnetic fields at the metamaterial resonance, the cross-polarized reflectance spectra for the $d = 40$ nm SRR-bar (Fig. 6.6A blue dotted line) is also reported. This is corroborated by measurements (not shown here) of functionalized planar Au surfaces and arrays with resonant frequencies far from these vibrational modes where

there is also no detectable *p*MA signal. The electric field intensity at 6.25 μm (1600 cm^{-1}) for both the *x*-*y* plane and the *x*-*z* plane of the $d = 40$ nm SRR-bar is shown in Fig. 6.6B. The *x*-*z* plane cut is taken at a point just beyond the tips of the SRR arms, where the field intensity is highest (dotted white line). We note that the near-field enhancement is strongest through the gap and along the sides of the SRR and choose all regions with $|\mathbf{E}_x|^2$ greater than 10^3 to determine the electromagnetic hot spot region. The path length of the high intensity region is multiplied by the thickness of the Au, 100 nm, to give a surface area of 0.087 μm^2 . We assume monolayer coverage of *p*MA to the resonators and a molecular cross section on Au of 0.3 nm^2 (Ref. [116]), yielding approximately 4.4×10^8 active *p*MA molecules per SRR. The number of molecules contributing to the signal from the 800 nm thick *p*MA reference film is 1.2×10^{13} molecules. The signal enhancement factor (*EF*) for each vibrational mode is determined by comparing the ratios of the resonantly enhanced signals to the signals from the neat *p*MA according to Equation (6.1).

$$EF = \frac{\Delta R_{SRR}/N_{SRR}}{\Delta R_{Ref}/N_{Ref}} \quad (6.1)$$

Here, N_{SRR} is the number of molecules adsorbed in the high intensity region of all SRRs in the illuminated region, N_{ref} is the number of molecules contributing to the signal from the *p*MA film, and ΔR_{ref} is the signal for each vibrational mode. The EF values for the vibrational modes at each coupling distance are reported in Fig. 6.6C. For the $d = 40$ nm SRR-bar array, we find SEIRA enhancement factors for all modes on the order of 10^4 which is the same as other high performing nanostructured geometries [91, 93]. The high enhancement factors and adaptability of the approach to any particular set of vibrational modes indicates that metamaterial designs may be of particular interest to the development of new SEIRA, as well as SERS, substrates.

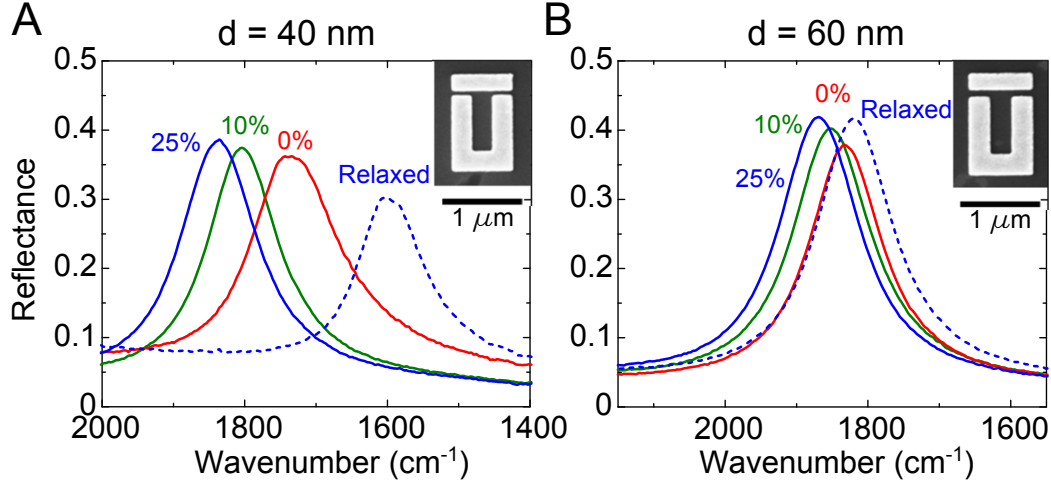


Figure 6.7. FTIR reflection spectra for arrays of resonators on PDMS with coupling distances of 40 nm and 60 nm are shown.

6.4.2 Post-Fabrication Tuning of a Metamaterial Resonance for Surface-Enhanced Spectroscopy

Although the enhancement factors for resonators on Si are high, this approach lacks the *in situ* tunability that may be possible with active metamaterial components. We also evaluate the coupled resonator metamaterials on PDMS as a potential SEIRA substrate. A major concern for this system, however, is the relatively low electric field intensity that is attainable. The electric field intensity observed for the SRRs on Si (Fig. 6.6B) is an order of magnitude higher than that observed for the resonators on PDMS (Fig. 6.1C) due to the much higher refractive index contrast of the Si with respect to the environment. The attractiveness of the PDMS system is the tunability of the resonant response post-fabrication, and we have previously shown that the metamaterial resonance can be tuned by a full linewidth via mechanical distortion of the substrate [114].

Following the discussion in Chapter 5, we use plastic deformation of the PDMS at the nanoscale to tune a resonator to the correct resonant frequency. As previously reported, we have designed resonators that operate over a wide range of frequencies, and for this work we must choose resonators that are in the same operating regime as the vibrational modes of interest. Figure 6.7 shows the FTIR spectra for two different

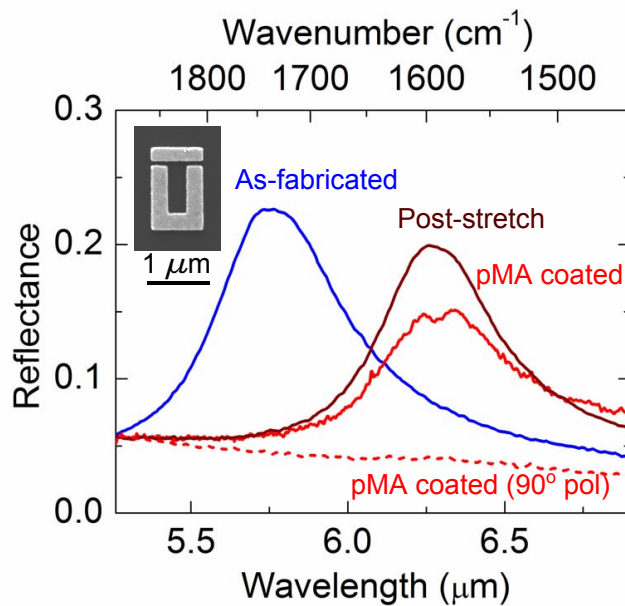


Figure 6.8. FTIR reflection spectra for an array of resonators on PDMS with a coupling distance of 40 nm are shown. The “as-fabricated” response for the resonator array is shown in blue, the dark red line shows the spectrum for the array of resonators after stretching to the appropriate resonance, and the red line indicates the response for the array after functionalizing with *p*MA. The dotted line shows the cross-polarized measurement for the functionalized array.

arrays of resonators with $w = 800$ nm. The resonators have coupling distances of 40 and 60 nm and we note that the extent of tunability of the $d = 40$ nm resonator is significantly greater than for the $d = 60$ nm. This allows us to tune the resonance so that it overlaps with the particular vibrational mode of interest. We select this SRR-bar coupled resonator geometry which has an initial resonant frequency of 5.78 μm (Figure 6.7 red line). The sample is stretched 25% parallel to the SRR arms, pulling the bar away from the SRR. The resonance at various degrees of strain are reported in Fig. 6.7A. When the sample is relaxed, the PDMS between the resonators contracts causing the coupling distance to decrease from the initial value. The resonant wavelength is permanently redshifted to 6.27 μm , which is evident from the FTIR reflection spectrum (Fig. 6.7 dotted blue line). The new resonance coincides with the vibrational mode of interest in *p*MA at 1585 cm^{-1} , demonstrating how sensors with customizable responses can be designed with post-fabrication tunability.

The *p*MA is adsorbed to the surface of the PDMS in a manner similar to that used in microcontact printing [117]. A drop of 10 mM ethanolic solution of *p*MA is placed on the surface of the PDMS and allowed to dry. The sample is measured after drying and an obvious dip is present in the center of the resonant peak (Fig. 6.8 red line) with a ΔR of 0.9%. For reference, the initial resonant peak and post-stretch peak are also shown (Fig. 6.8 blue line and dark red line, respectively). The cross-polarized data are also reported (red dashed line) and show that the molecular signal is due to the overlap of the metamaterial resonance and the *p*MA vibrational modes. The *p*MA signal was also not readily apparent on bare patches of the PDMS or on arrays whose resonances do not overlap the vibrational modes. We assume that a number of molecules, those adhered to the Au and those between the SRR and bar, contribute to the signal. We do not report an enhancement factor for the vibrational modes of *p*MA on PDMS-based resonators as it is unclear exactly how many molecules contribute to the signal and will depend on the diffusion of *p*MA through the PDMS. Nevertheless, the observed signal for the *p*MA-coated sample is the first report of SEIRA from a compliant substrate and suggests that polymeric-based metamaterials could be useful platforms for sensing given both their *in situ*

tunability and the potential for integration with polymeric-based devices, such as microfluidic cells. The signal from these types of sensors could be increased by using higher index polymeric substrates, making this approach a promising step forward in the design of flexible, tunable metamaterial-based sensors.

6.5 Summary and opportunities

The resonant frequency of nanostructured resonators is largely fixed at the time of fabrication and a number of different resonators must be patterned in order to create structures with different resonant properties. We have shown that compliant metamaterials can be used to sense changes in refractive index at a number of resonant frequencies with FOM values of up to 10.1. We have shown that resonator size can be used to tune the resonant frequency through the IR and achieve sensitivities of 3370 nm/RIU (120 meV/RIU) for large resonators at long wavelengths and 1190 nm/RIU (500 meV/RIU) for small resonators in the near IR. We have also demonstrated that by coupling the metamaterial resonance to particular vibrational modes, we can enhance a vibrational mode signal with coupled Au resonators on Si by a factor of 10^4 . Resonators on a compliant substrate can be stretched and mechanically deformed in order to optimize the alignment of a vibrational mode with the metamaterial resonant frequency post-fabrication, and we note that vibrational modes at frequencies more than a linewidth distance from the as-fabricated resonance could be accessed by inducing substrate strain. Exploiting and tailoring the mechanical deformation of these metamaterial systems opens the door to the possibility of creating a new class of *in situ* customizable sensing surfaces. For example, we could design sensors capable of concurrent sensing of vibrational mode enhancement and refractive index shift. Fig. 6.9 shows the change in resonant response for a resonator in three different optical matching fluids. The peaks in the resonant response show the vibrational modes of the optical fluids and prove that both types of sensing can be achieved on a single sensing platform.

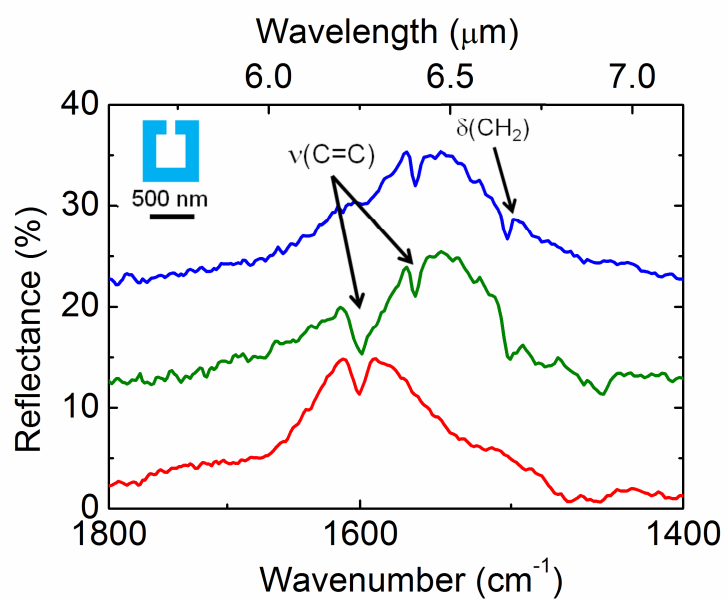


Figure 6.9. Concurrent refractive index sensing and vibrational mode spectroscopy with an array of SRRs on PDMS.

Chapter 7

Summary and Outlook

Metamaterials are composites consisting of subwavelength structures designed to exhibit particular responses to an incident electromagnetic wave. In general, the properties of a metamaterial are fixed at the time of fabrication by the dimensions of each unit cell and the materials used. Incorporating dynamic components into a metamaterial system enables the design of tunable resonant responses. In this thesis, we have investigated passive structures in an attempt to understand the underlying coupling mechanisms that can be used to enhance tunability. We have demonstrated how thermal actuation of a phase transition material can be used to create dynamically tunable metamaterials. We have also demonstrated that mechanical deformation of a compliant substrate can be used to achieve linewidth tunability in split-ring resonator (SRR)-based metamaterials and we have explored some of the consequences of this large tunability. In addition to the importance of a tunable response, the flexibility of the compliant system represents a departure from traditional hard, brittle substrates and enables the incorporation of metamaterials into new types of devices, including the flexible sensors we have discussed in this work. A significant portion of this thesis was devoted to developing an understanding of the mechanics of compliant metamaterials and investigating how the elastomeric nature of these materials could be exploited.

The active metamaterial world opens up a whole range of possibilities for device design and forces us to think about material properties in an entirely new way. While obvious extensions to the work in this thesis have been included in the relevant chapters, here we take the opportunity to outline new areas for research that incorporate broader elements of the work described.

1. **Integrate active metamaterials into telecommunication devices.** We were able to design and demonstrate metamaterials operating at 1550 nm and, as an example, Fig. 7.1 shows the behavior for a small resonator on PDMS with an initial resonance of 1.42 μm . In an optical matching fluid with $n = 1.47$, the resonance is shifted over a full linewidth to 2 μm . While this example demonstrates refractive index sensitivity, the resonance near 1.55 μm shows that these materials could be useful as modulators or filters for telecommunications. We can envision incorporating a single unit cell or small array of resonators onto a chip and dynamically tuning their response with a thermal, optical, electrical, or mechanical input. This could lead to either frequency tuning or amplitude modulation of the incoming signal. Similarly, we could design on-chip resonators for sensing and use an incident beam to both excite and probe the properties of the analyte-resonator ensemble. In these types of on-chip assemblies, the amount of power lost to the metallic structure would have to be monitored to avoid over heating and signal loss or noise. Using the simulation technique outlined in Chapter 2 for tracking power absorption in solar cells would be critical to the optimization of appropriate low-loss designs.
2. **Engineering strain in three dimensions.** The work described in this thesis is primarily focused on the design of metamaterial surfaces. If we start to think about designing structures with three-dimensional features, a wide variety of devices and applications become feasible. The first, most obvious, route is to add corrugation to the PDMS substrate. Adding corrugation, or in this example a simple air channel, gives us an additional tool for engineering the strain in a compliant metamaterial system. In Figure 7.2A, we show the results from an FEM model of a slab of PDMS with an SRR-bar resonator attached. In this model, the top surface of the PDMS (in the y -direction) is fixed and a force is applied to the bottom face of the PDMS. This mimics the actual experiments that were shown in Chapter 5 where the bar is being stretched away from the SRR. The arrows in this image indicate the direction of displacement and the

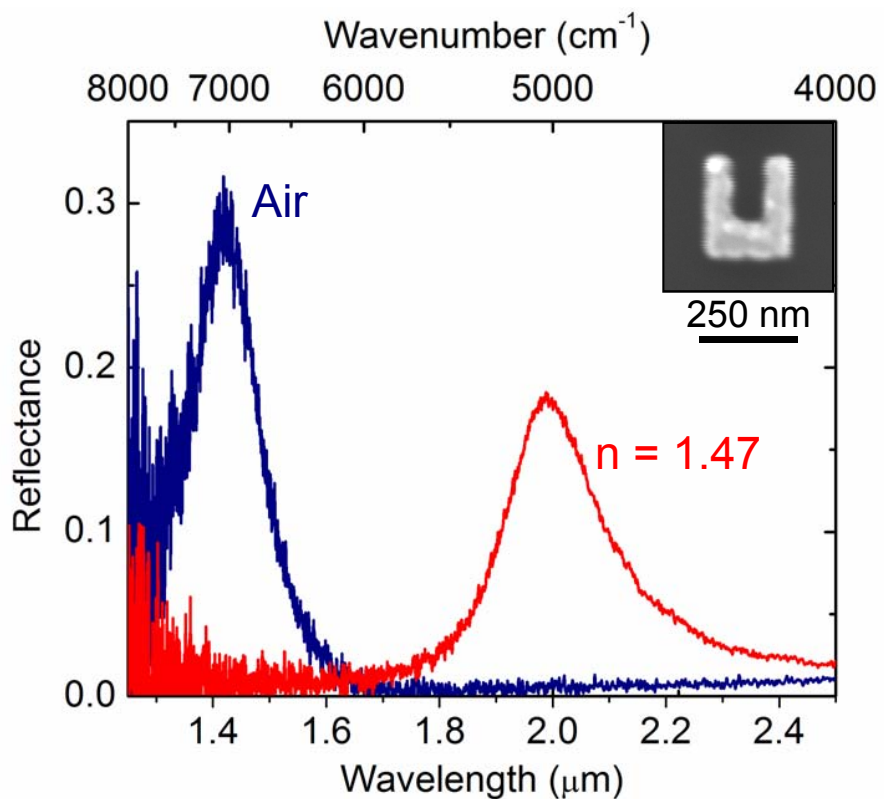


Figure 7.1. The reflectance spectra shown here are for a small SRR on PDMS (shown in inset) in both an ambient environment (navy line) and in an optical matching fluid with $n = 1.47$ (red line).

amount of global strain induced corresponds to about 10%, resulting in a gap distance change of 5 nm. The simulated reflection spectra for this system both before and after stretching are shown in the right-hand panel and match the previous experiments well. Figure 7.2B shows the corresponding results for when an air channel is introduced between the SRR and the bar. We notice that for the same amount of applied force, much more significant distortion is achieved. Interestingly, there is now a displacement gradient through the PDMS, which leads to distribution of the stress through the PDMS rather than localizing the stress at the PDMS/Au interface, as in Fig. 7.2A. In this case, the SRR is essentially decoupled from the bar in this example leading to a gap distance change of 25 nm. The resulting change in the simulated reflection spectra is shown in the left panel. The original resonances are different in the two cases because the air channel affects the dielectric environment of the resonator. Also, with the addition of an air channel, linewidth tunability can now be achieved for a force corresponding to only 10% global strain.

Incorporating a third dimension also opens up an interesting avenue for understanding what happens when antennas or resonators are brought very slowly into contact. Ideally, we want to investigate the physics of a single unit cell and probe the optical interactions at the nanoscale as these resonators go from being independent to contacting. Top-down fabrication constraints limit our ability to fabricate structures with smaller than 10 nm gaps and bottom-up approaches do not give adequate control over the appropriate parameters. The hard/soft nanolithographic transfer technique developed in this thesis for creating compliant metamaterials combined with engineering the material properties in the third dimension offers an approach for taking a single sample and probing how the resonance changes as the structures are brought closer together. For the example described above without air channel, the amount of force required to bring the resonators together results in microscale tears in the PDMS between resonators. For the substrate with air channel, however, the channel is forced to contract and the resonators are brought into contact as a force is applied in

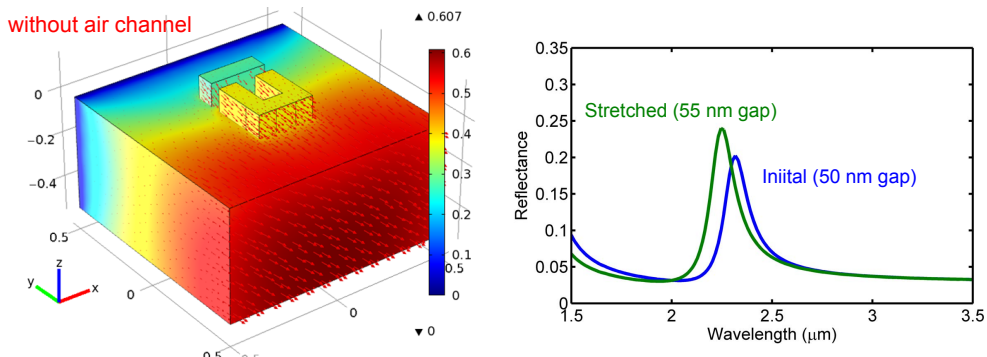
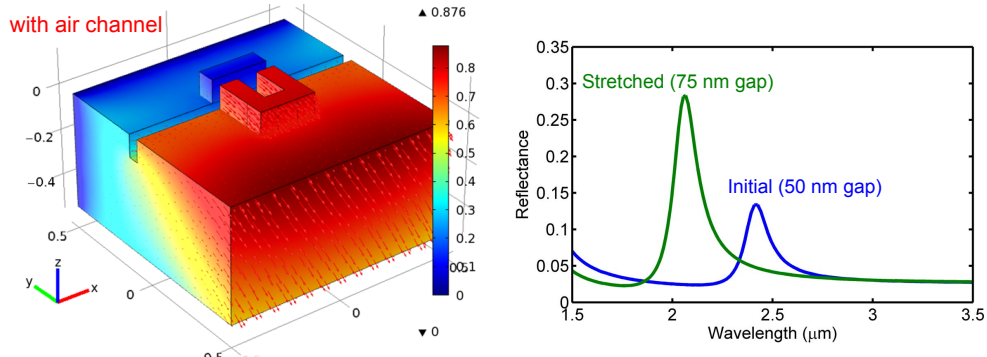
A**B**

Figure 7.2. A. FEM simulation of a PDMS slab with SRR-bar resonator attached is shown in the left panel. A force is applied in the y -direction to induce a global strain of 10% in the material. In the left panel, we show the resonant response of an array of structures calculated via full-field simulation. B. The same data are shown for a structure with added air channel in the PDMS.

the x - (as opposed to the y -) direction.

3. Structural metamaterials and negative Poisson's ratio materials. In a more conceptual vein, this work forces us to think about material design in a new way. An interesting branch of research that has remained somewhat unexplored at the nanoscale are negative Poisson's ratio materials. Referring to the definitions in Appendix A, a material with positive Poisson's ratio will contract in one dimension when stretched in another. Negative Poisson's ratio materials, on the other hand, will expand in the second dimension. This leads to interest-

ing phenomena, particularly when we combine this effect with electromagnetics. As a simple example, we consider a Au cylindrical antenna. In Fig. 7.3A, we calculate the extinction coefficients for varying degrees of applied force. The force distorts the shape of the nanoscale Au antenna such that the antenna is elongated in the axial direction and contracts in the radial direction. As the resonance depends strongly on the d/L ratio, the shape distortion results in a redshift of the antenna extinction. For the same example, but with a negative Poisson's ratio (Fig. 7.3B), the resonance is largely unaffected by the applied force. This is because the ratio of d/L is changing much more slowly than for the real Au. The applied force necessary to distort Au this significantly is very large and we cannot fabricate "negative Au", however this example illustrates the possibility of creating materials that when strained do not experience a shift in resonance. One possible future research project could be the design of a polymeric substrate with metallic inclusions that resonate at the same frequency no matter how much they are strained or distorted. A starting point for this work would be to examine the foams and collapsing honeycomb structures that have been demonstrated previously at much larger length scales.

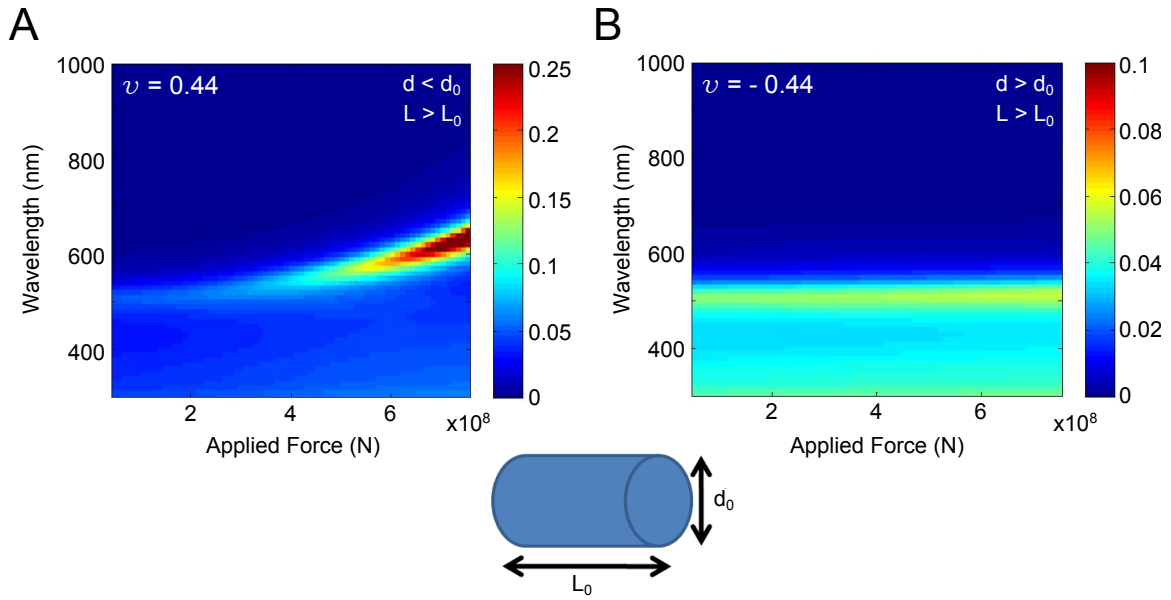


Figure 7.3. A. This panel shows the anticipated extinction coefficient for a “normal” Au cylindrical antenna under varying amounts of applied force. B. The extinction coefficient made of a negative Poisson’s ratio material. Here we have used the negative value of the Poisson’s ratio of Au. As the force is applied, both the diameter of the cylinder and the length of the cylinder will increase.

Appendix A

Modeling Metamaterial Mechanics Using COMSOL

COMSOL offers the ability to understand the deformation of materials and structures under loads and thus provided the perfect simulation environment for analyzing our compliant metamaterials. The approach that we used to evaluate the resonant structures was fairly straightforward and used the stationary solution solver. More complex solving routines could be implemented for simultaneous solution of the electromechanical properties; however, this would require a significant increase in computing time. Instead, we chose to decouple the electromechanics part of the problem and have developed a routine using MATLAB to couple the deformation solution found in COMSOL with full field electromechanical simulation using Lumerical. In this appendix, we will review the continuum mechanics that are used in the COMSOL routine to find solutions for the deformed structures and we will outline how to build a model for analyzing a basic split-ring resonator on PDMS.

For our calculations, we use the solid mechanics interface within the COMSOL Multiphysics primary module. As with any COMSOL model, it is necessary to first define the geometry of the system. For our preliminary calculations, we defined our structures on a single plane in the 2D environment. The 3D environment, however, provided some interesting perspective on the deformation and strain in the metamaterial both near and far from the metal/PDMS interface. In addition, the ability to create more interesting three dimensional structure in the material allowed us to begin to design some of the more interesting metamaterial examples included in the last chapter of the thesis.

A.1 Review of Key Material Properties

As a starting point, and in particular because of our colloquial (mis)use of the words "strain" and "stress", we begin by defining the relationships that exist in materials subjected to an applied force. The way that a material responds and contorts in the face of an applied force defines its mechanical properties. We consider as a simple example the uniaxial elongation of a material. For a slab whose length goes from l_0 to l as the result of an applied force, F , we define stress, σ , as

$$\sigma = F/A. \quad (\text{A.1})$$

Strain, ϵ , is defined as the change in length of the slab:

$$\epsilon = \Delta l/l_0. \quad (\text{A.2})$$

These two properties are related by a constant, which is obtained from Hooke's Law.

$$\sigma = E\epsilon \quad (\text{A.3})$$

Here, E is Young's modulus. For most materials, a uniaxial extension in one direction is accompanied by contraction in another and for the case of our slab we can write

$$\frac{\Delta w}{w_0} = -\nu \frac{\Delta l}{l_0}. \quad (\text{A.4})$$

Here, ν is Poisson's ratio. For homogeneous, isotropic materials, Young's modulus and Poisson's ratio are the only constants that we need to describe the elastic behavior of a material. For polymers this holds true for only small amounts of force. As we showed in the experiments in Chapter 5, the resonant behavior and presumably the PDMS bulk have an elastic response for a global strain of up to 10%. Therefore, in our calculations we assume that the PDMS can be treated as a material with constant properties as a model for understanding the deformation for small degrees of strain.

A.2 Relevant Solid Mechanics Theory

We will now describe the solid mechanics theory that is relevant for understanding the required COMSOL inputs. This is merely a summary, however, of some key concepts and governing equations and for a more thorough dissertation on continuum mechanics, there are a number of useful texts.

A.2.1 The Coordinate Systems of Continuum Mechanics

In continuum mechanics theory, there are two sets of coordinates used in order to describe both the actual position of an object in space and also the deformation of a point in the object relative to other points. This second set of coordinates is referred to as the material coordinates of an object. Understanding the difference between these two sets of variables is useful for extracting information about the deformation from COMSOL to other programs. As an example, for a particle that is deformed by some external force,

$$\mathbf{x}_{\mathbf{X}, t} = \mathbf{X} + \mathbf{u}_{\mathbf{X}, t}. \quad (\text{A.5})$$

Here, \mathbf{x} is the position of the particle in spatial coordinates, \mathbf{X} is the material coordinate of the particle, and \mathbf{u} is the displacement vector that moves the particle from its initial to its final position. In some cases, it is useful to export the deformation vectors and the initial spatial coordinates from COMSOL.

A.2.2 Governing Equations

The governing equation for a linear elastic material is the relationship between the strain tensor and the displacement gradient, which can be written:

$$\boldsymbol{\epsilon} = \frac{1}{2} [\nabla \mathbf{u} + (\nabla \mathbf{u})^T]. \quad (\text{A.6})$$

Hooke's Law is the constitutive equation which relates stress and strain. While we used a simplified version of Hooke's Law for the slab example described above,

the general equation, ignoring initial stresses and strains and thermal expansion, is

$$\sigma = \mathbf{C} : \boldsymbol{\epsilon}. \quad (\text{A.7})$$

Here, \mathbf{C} is the stiffness or elasticity tensor and depends on Young's modulus and Poisson's ratio.

Loads are defined either at a point, an edge, a face, or across an entire body. For our purposes we apply a force at an edge and change the force until the deformation matches the deformation that is induced experimentally. Once the study is set up with appropriate material parameters and applied forces, COMSOL uses the principle of virtual work to solve for the stress and strain through the system. The principle of virtual work states the work from internal strains must equal the work from external loads.

A.3 Steps for Creating a COMSOL Model

There are number of considerations that should be taken into account when building a COMSOL model. In particular, symmetry should be used as often as possible as this will significantly reduce the simulation run time. The following guidelines are an attempt to outline some basic considerations for building the types of mechanical calculations that we have done and, in this illustration, we use the simple example of square split-ring resonator (SRR).

1. **Define the geometry.** The geometry of the structure can be defined in the CAD window, either in 2D or 3D environment. In the simulation shown in Figure A.1, the objects were created in the 2D CAD environment and then extruded to the 3D multiphysics window. One can also directly create objects in the 3D window or import objects from other CAD software, e.g. SolidWorks. In the version of COMSOL used for our simulations it was not possible to import any given image, which limited a direct comparison with our fabricated structures. The red outlined box in Fig. A.1 shows where in the model builder

the geometry is defined. Here, composite object 1 is the PDMS slab and object 2 is the Au resonator (highlighted in blue in the image).

2. **Input material properties.** In particular the Young's modulus, Poisson's ratio, and density for the materials used in the model should be input. A useful approach is to use predefined materials and then adjust the properties as necessary. In this model, the properties of Al were adjusted to reflect the actual properties of Au and acrylic plastic was used a base for the PDMS properties. The green highlighted box in Fig. A.1 shows that the material constants were changed for this model (indicated by green check marks).
3. **Select appropriate fixed conditions and boundary loads.** Two approaches have been used in this work to define the forces on the material. The first is to fix one plane of the material and apply a uniaxial load to the opposite face. The second approach is to apply a load to opposing faces of the PDMS. It should be noted, however, that this latter approach can cause numerical instabilities if not implemented correctly. These values are input directly to the 'Solid Mechanics' interface of COMSOL and is outlined in red in Fig A.2.
4. **Define the mesh.** In the latest version of COMSOL (4.1), the user can optimize the mesh for the physics. This is evident in Fig. A.2 where the mesh size is smaller around the split-ring gap. In most of the studies that were run, we used either a normal or fine mesh. In some cases, the finer mesh setting was used, although this was only necessary for rounded features which are inherently difficult to mesh. It is good practice to check the meshed structure before running the simulation.
5. **Set up the study type.** For our calculations, we used the stationary study settings to find a steady state solution for the deformation.
6. **Analyze the results.** A slice plot of the local strain at the plane that intersects the interface of the PDMS and the metal are used throughout this thesis and shown in Fig. A.3, an arrow plot at $x = 0$ is typically also included to show

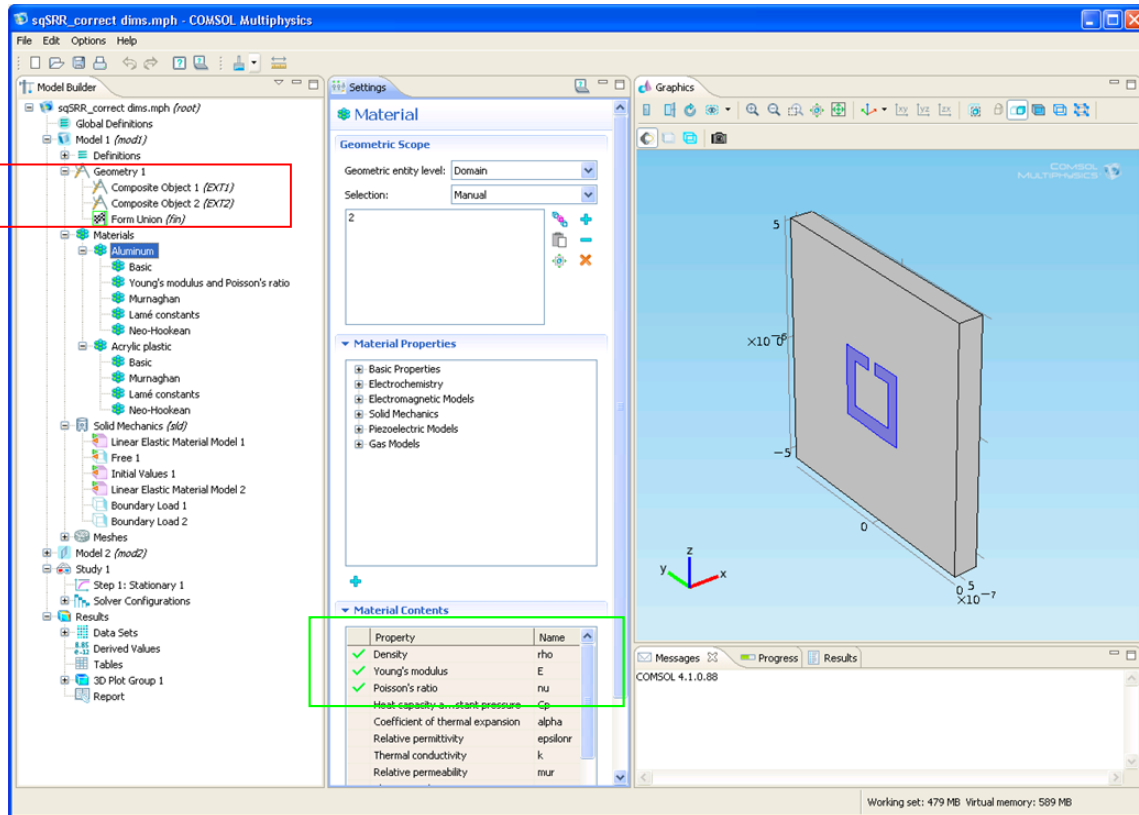


Figure A.1. This screenshot shows how the geometry of a simulation is defined and how the material parameters can be adjusted.

the direction of the deformation. COMSOL also gives options for adjusting the data range and color schemes, as evident in the center panel.

7. **Export data.** This is useful for integration with other software or plotting the data in an external program and can be found under the red highlighted box in the “Report” tab.

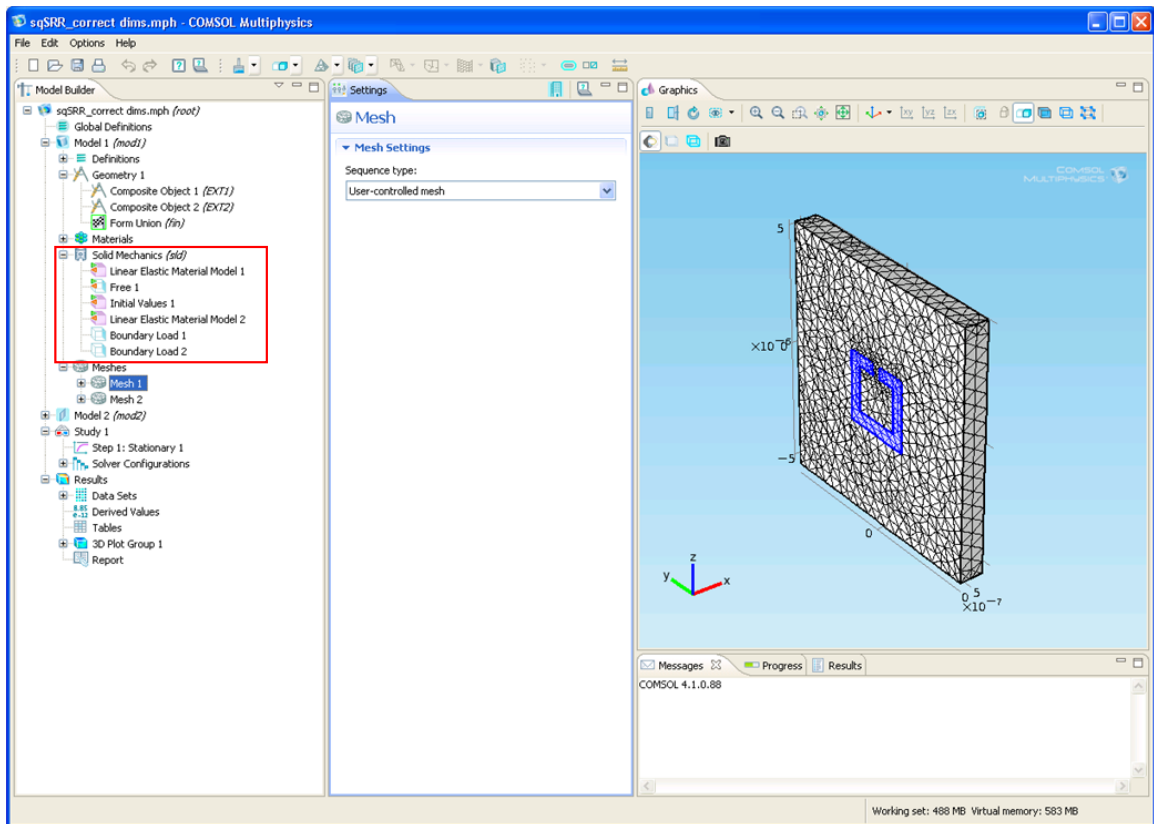


Figure A.2. This screenshot shows how the a structure can be meshed in COMSOL. The red outlined box shows where the specifics, i.e., the face loads, fixed boundaries, etc., of the solid mechanics model are input.

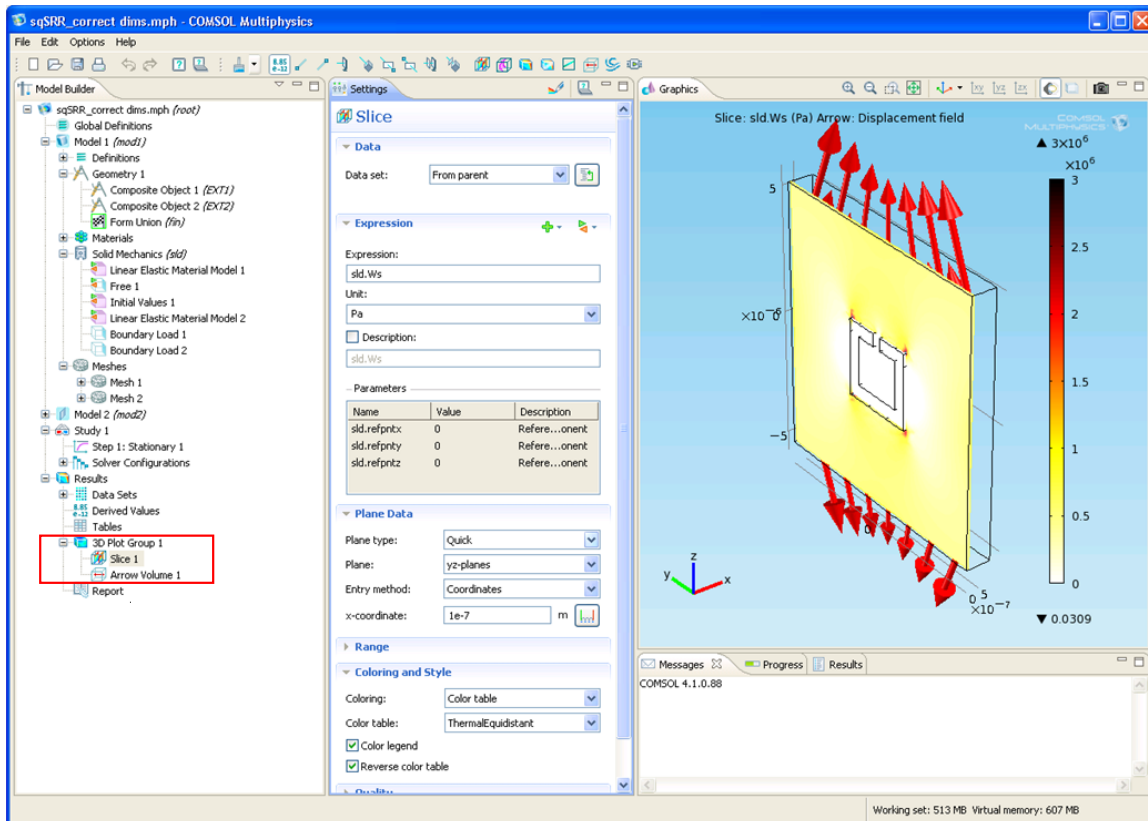


Figure A.3. This screenshot shows how two different plots can be overlaid in COMSOL. As outlined by the red box on the left, both a slice plot and an arrow plot are shown.

Appendix B

Fabrication of Metal Nanoparticle Arrays Using Anodic Alumina Templates

Anodic aluminum oxide (AAO) templates are used in this thesis to deposit nanoparticles on solar cells (Chapter 2). In this appendix, we outline the steps for fabrication of these templates. This process has been adapted from the one originally developed by Keisuke Nakayama [41].

1. AAO fabrication

(a) *Cut and degrease Al.*

Cut 4N Al sheet (0.5 mm thick) into strips (7.5 x 1.7 cm²). This can be done at the machine shop to achieve uniform sized sheets with smooth edges. The more uniform the sheets, the more predictable the anodization process will be. Degrease the Al in acetone in an ultrasonic bath for 5 min. The acetone can be used for about 20 sheets, it should then be replaced.

(b) *Electropolish Al.*

The Al sheets are electropolished to achieve an electrochemically flat surface. The electrolyte consists of H₂O (80 mL), H₃PO₄ (330 mL), H₂SO₄ (75 mL), and ethylene glycol (15 mL). Electropolishing is carried out with the Al sheet serving as the anode and a glassy carbon plate serving as the cathode at a constant current density of 250 mA/cm² (about 20-30 V) at 70°C for 5 min. Bubbles will form on the surface of the Al sheet in the first stage of electropolishing. This causes irregularities in the AAO templates and can be avoided by tapping the anode clip for the first minute

Table B.1. Anodization conditions for various operating voltages

Voltage (V)	Spacing (nm)	Electrolyte	Time (h)
25	63	0.3 M H ₂ SO ₄	8
40	100	0.3 M oxalic acid	4
80	200	0.3 M oxalic and malonic acid (50:50)	1
120	300	0.3 M malonic acid	2

of the process. Then rinse the Al sheet with water and acetone and store in fresh acetone.

(c) *First anodization.*

The first anodization makes the ordered hole structure in the Al sheet. Prior to anodizing, dip the Al sheet in an 8% NaOH solution for 40 sec. The anodization is carried out at constant voltage with stirring. A different Al cathode is used for each electrolyte (a different electrolyte is required for each voltage as shown in the table below). The temperature of the anodization is kept below 15°C by running the process in a water/ice bath. After anodization, rinse the Al sheet thoroughly with water.

(d) *Remove AAO layer.*

Remove the rough first AAO layer on the surface of the Al by leaving the sheet in chromic acid solution (6 g of CrO₃, 20 g of H₃PO₄, and 300 g of H₂O) at 50°C overnight. This solution should be replaced every 10 sheets or so.

(e) *Second anodization.*

The second anodization makes the pores straight and the time determines their depth, i.e. the AAO thickness. The same electrolyte solutions should be used as for the first anodization. The anodization times to achieve 700

nm thick membranes are 7 min for the 40 V solution, 3 min for the 80 V solution, and 120 V for the 120 V solution.

2. Through-pore etch

(a) *Mechanically remove back side of AAO template.*

Cover the better looking side of the template with a layer of clear nail polish. Also paint around the border of each membrane. Typically, four membranes can be made from each sheet and they should have a border of about 2 mm around the edge. The back side of the AAO template can either be removed using a box cutter and scraping off the surface of the Al. Alternatively, the Al can be etched using 8% NaOH solution. The NaOH should be dropped on the center of the template and left for 60 sec and then rinsed with water.

(b) *Chemical removal of Al sheet.*

Put the etched Al sheet into a mixture of iodine and methanol (30 g/30 g). The reaction takes about an hour and is highly exothermic. When the solution returns to room temperature, the reaction is finished. The AAO should then be carefully rinsed with acetone. The membranes will separate in the methanol solution and care must be taken to avoid breaking one membrane with another. Discard most of the iodine solution from the container (do not discard all of it as the membranes will dry out) and rinse with copious amounts of acetone. Remove each membrane carefully from the solution and rinse again with acetone.

(c) *Chemical etch of the bottom Al layer.*

Coat the border of the AAO template with nail polish and place the membrane in the center of a fluoroware lid. Place the lid in a water bath set to 30°C. Preheat the 5% H₃PO₄ etch solution in the water bath. Place a drop of the solution in the center of the membrane. To achieve

the dimensions shown in Table B.1, the etch times are 40 min for the 40 V AAO template, 65 min for the 80 V AAO template, and 90 min for the 120 V AAO template. The etch times can be increased to achieve larger pore sizes, but this will also reduce the mechanical robustness of the membrane and the etch time should be monitored carefully. After etching, rinse the template with water and let it dry.

3. Metal evaporation

(a) *Adhere AAO template to the substrate.*

Place a drop of water on the substrate and float the AAO on top of it. The bottom side of the AAO template is flatter and should be the side in direct contact with the substrate. Using the corner of a texwipe, slowly draw the water off the surface from around the outside of the membrane. The membrane should be pulled by capillary forces into contact with the substrate. Then cut the AAO out of the Al frame using a razor blade.

(b) *Evaporate metal through AAO template.*

Position the substrate in the evaporator directly above the evaporation source. This is important given the high aspect ratio of the AAO templates and off-angle evaporation will not result in nanoparticle deposition.

(c) *Remove AAO template from substrate.*

Use scotch tape to remove the AAO from the substrate surface. Peel off the AAO template slowly.

(d) *Annealing nanoparticles.*

In some cases, annealing of the nanoparticles is necessary and improves solar cell performance. For Ag nanoparticles, this should be done at 200°C for 30 min in a 5% H₂/N₂ environment.

Bibliography

- [1] Vladimir M. Shalaev. Optical negative-index metamaterials. *Nature Photonics*, 1(1):41–48, January 2007. ISSN 1749-4885. doi: 10.1038/nphoton.2006.49. URL <http://www.nature.com/doifinder/10.1038/nphoton.2006.49>. 1, 8, 9, 50, 66, 94
- [2] D R Smith, J B Pendry, and M C K Wiltshire. Metamaterials and Negative Refractive Index. *Science*, 305(August):788–792, 2004. 1, 50, 66, 94
- [3] Yongmin Liu and Xiang Zhang. Metamaterials: a new frontier of science and technology. *Chemical Society Reviews*, 40:2494–2507, January 2011. ISSN 1460-4744. doi: 10.1039/c0cs00184h. URL <http://www.ncbi.nlm.nih.gov/pubmed/21234491>. 1, 7
- [4] Stefan Linden, Christian Enkrich, Martin Wegener, Jiangfeng Zhou, Thomas Koschny, and Costas M Soukoulis. Magnetic response of metamaterials at 100 terahertz. *Science*, 306(5700):1351–1353, November 2004. ISSN 1095-9203. doi: 10.1126/science.1105371. URL <http://www.ncbi.nlm.nih.gov/pubmed/15550664>. 1, 8, 50, 94
- [5] T J Yen, W J Padilla, N Fang, D C Vier, D R Smith, J B Pendry, D N Basov, and X Zhang. Terahertz magnetic response from artificial materials. *Science*, 303(5663):1494–1496, March 2004. ISSN 1095-9203. doi: 10.1126/science.1094025. URL <http://www.ncbi.nlm.nih.gov/pubmed/15001772>. 1, 50

- [6] Carsten Rockstuhl and Weili Zhang. Terahertz phase modulator. *Nature Photonics*, 3:130–131, 2009. ISSN 00135194. doi: 10.1049/el:20000837. URL <http://link.aip.org/link/ELLEAK/v36/i13/p1156/s1&Agg=doi>. 1
- [7] X. G. Peralta, M. C. Wanke, C. L. Arrington, J. D. Williams, I. Brener, A. Strikwerda, R. D. Averitt, W. J. Padilla, E. Smirnova, A. J. Taylor, and J. F. O’Hara. Large-area metamaterials on thin membranes for multilayer and curved applications at terahertz and higher frequencies. *Applied Physics Letters*, 94:16113, 2009. doi: 10.1063/1.3114416. 1
- [8] D J Shelton, K R Coffey, and G D Boreman. Experimental demonstration of tunable phase in a thermochromic infrared-reflectarray metamaterial. *Optics Express*, 18(2):1330–1335, 2010. 1
- [9] Matthew J Dicken, Koray Aydin, Imogen M Pryce, Luke A Sweatlock, Elizabeth M Boyd, Sameer Walavalkar, James Ma, and Harry A Atwater. Frequency tunable near-infrared metamaterials based on VO₂ phase transition. *Optics Express*, 17(20):18330–9, September 2009. ISSN 1094-4087. URL <http://www.ncbi.nlm.nih.gov/pubmed/19907624>. 1, 66
- [10] J. B. Pendry. Negative refraction makes a perfect lens. *Physical Review Letters*, 85(18):3966–3969, October 2000. ISSN 1079-7114. URL <http://www.ncbi.nlm.nih.gov/pubmed/11041972>. 2, 50
- [11] Nicholas Fang, Hyesog Lee, Cheng Sun, and Xiang Zhang. Sub-diffraction-limited optical imaging with a silver superlens. *Science (New York, N.Y.)*, 308(5721):534–7, April 2005. ISSN 1095-9203. doi: 10.1126/science.1108759. URL <http://www.ncbi.nlm.nih.gov/pubmed/15845849>. 2
- [12] J B Pendry, D Schurig, and D R Smith. Controlling electromagnetic fields. *Science (New York, N.Y.)*, 312(5781):1780–2, June 2006. ISSN 1095-9203. doi: 10.1126/science.1125907. URL <http://www.ncbi.nlm.nih.gov/pubmed/16728597>. 2, 50

[13] Wenshan Cai, Uday K Chettiar, Alexander V Kildishev, and Vladimir M Shalaev. Optical cloaking with metamaterials. *Nature Photonics*, 1(April):224–227, 2007. doi: 10.1038/nphoton.2007.28. 2, 50

[14] D Schurig, J J Mock, B J Justice, S A Cummer, J B Pendry, A F Starr, and D R Smith. Metamaterial electromagnetic cloak at microwave frequencies. *Science*, 314(5801):977–980, November 2006. ISSN 1095-9203. doi: 10.1126/science.1133628. URL <http://www.ncbi.nlm.nih.gov/pubmed/17053110>. 2, 50

[15] Nathan Kundtz and David R Smith. Extreme-angle broadband metamaterial lens. *Nature Materials*, 9(2):1–4, 2009. ISSN 1476-1122. doi: 10.1038/nmat2610. URL <http://dx.doi.org/10.1038/nmat2610>. 2

[16] C. F. Bohren and D. R. Huffman. *Absorption and Scattering of Light by Small Particles*. Wiley, New York, NY, 1983. 2, 14

[17] J. D. Jackson. *Classical Electrodynamics*. John Wiley and Sons, New York, NY, 3rd edition, 1999. 2, 3, 6

[18] Viktor G Veselago. The electrodynamics of substances with simultaneously negative values of ϵ and μ . *Soviet Physics Uspekhi*, 10(4):509–514, April 1968. ISSN 0038-5670. doi: 10.1070/PU1968v010n04ABEH003699. URL <http://stacks.iop.org/0038-5670/10/i=4/a=R04?key=crossref.49e6b8a483029417bb518fd3889a3ed3>. 3, 50

[19] J.B. Pendry, A.J. Holden, D.J. Robbins, and W.J. Stewart. Magnetism from conductors and enhanced nonlinear phenomena. *IEEE Transactions on Microwave Theory and Techniques*, 47(11):2075–2084, 1999. ISSN 00189480. doi: 10.1109/22.798002. URL <http://ieeexplore.ieee.org/lpdocs/epic03/wrapper.htm?arnumber=798002>. 5, 7

[20] Jb Pendry, Aj Holden, Wj Stewart, and I Youngs. Extremely low frequency plasmons in metallic mesostructures. *Physical review letters*, 76(25):4773–4776,

June 1996. ISSN 1079-7114. URL <http://www.ncbi.nlm.nih.gov/pubmed/10061377>. 5

- [21] Shumin Xiao, Uday K. Chettiar, Alexander V. Kildishev, Vladimir Drachev, I. C. Khoo, and Vladimir M. Shalaev. Tunable magnetic response of metamaterials. *Applied Physics Letters*, 95(3):033115, 2009. ISSN 00036951. doi: 10.1063/1.3182857. URL <http://link.aip.org/link/APPLAB/v95/i3/p033115/s1&Agg=doi>. 8, 66
- [22] Stefan Linden, Christian Enkrich, Gunnar Dolling, Matthias W Klein, Jiangfeng Zhou, Thomas Koschny, Costas M Soukoulis, Sven Burger, Frank Schmidt, and Martin Wegener. Photonic Metamaterials : Magnetism at Optical Frequencies. *IEEE Journal of Selected Topics in Quantum Electronics*, 12(6):1097–1105, 2006. 8
- [23] Costas M Soukoulis, Stefan Linden, and Martin Wegener. Negative refractive index at optical wavelengths. *Science*, 315:47–49, June 2007. ISSN 1094-4087. doi: 10.1126/science.1136481. 8, 9
- [24] G Dolling, M Wegener, C M Soukoulis, and S Linden. Negative-index metamaterial at 780 nm wavelength. *Optics Letters*, 32(1):53–55, January 2007. ISSN 0146-9592. URL <http://www.ncbi.nlm.nih.gov/pubmed/17167581>. 8, 9, 50, 94
- [25] Uday K Chettiar, Alexander V Kildishev, Hsiao-kuan Yuan, Wenshan Cai, Shumin Xiao, Vladimir P Drachev, and Vladimir M Shalaev. Dual-band negative index metamaterial : double negative at 813 nm and single negative at 772 nm. *Optics Letters*, 32(12):1671–1673, 2007. 8
- [26] Vladimir M Shalaev, Wenshan Cai, Uday K Chettiar, Hsiao-kuan Yuan, Andrey K Sarychev, Vladimir P Drachev, and Alexander V Kildishev. Negative index of refraction in optical metamaterials. *Optics Letters*, 30(24):3356–3358, 2005. 9, 50

[27] Uday K Chettiar, Alexander V Kildishev, Thomas A Klar, and Vladimir M Shalaev. Negative index metamaterial combining magnetic resonators with metal films. *Optics Express*, 14(17):7872–7, August 2006. ISSN 1094-4087. URL <http://www.ncbi.nlm.nih.gov/pubmed/19529154>. 9

[28] Jiangfeng Zhou, Lei Zhang, Gary Tuttle, Thomas Koschny, and Costas Soukoulis. Negative index materials using simple short wire pairs. *Physical Review B*, 73(4):1–4, January 2006. ISSN 1098-0121. doi: 10.1103/PhysRevB.73.041101. URL <http://link.aps.org/doi/10.1103/PhysRevB.73.041101>. 9

[29] Jason Valentine, Shuang Zhang, Thomas Zentgraf, Erick Ulin-Avila, Dentcho A Genov, Guy Bartal, and Xiang Zhang. Three-dimensional optical metamaterial with a negative refractive index. *Nature*, 455(7211):376–379, September 2008. ISSN 1476-4687. doi: 10.1038/nature07247. URL <http://www.ncbi.nlm.nih.gov/pubmed/18690249>. 9, 50

[30] Na Liu and Harald Giessen. Three-dimensional optical metamaterials as model systems for longitudinal and transverse magnetic coupling. *Optics Express*, 16(26):21233–8, December 2008. ISSN 1094-4087. URL <http://www.ncbi.nlm.nih.gov/pubmed/19104553>. 9, 34

[31] Na Liu, Thomas Weiss, Martin Mesch, Lutz Langguth, Ulrike Eigenthaler, Michael Hirscher, Carsten Sönnichsen, and Harald Giessen. Planar metamaterial analogue of electromagnetically induced transparency for plasmonic sensing. *Nano Letters*, 10(4):1103–7, April 2010. ISSN 1530-6992. doi: 10.1021/nl902621d. URL <http://www.ncbi.nlm.nih.gov/pubmed/20017551>. 9, 34, 82, 94, 95, 101

[32] Hou-tong Chen, Willie J Padilla, Joshua M O Zide, Arthur C Gossard, Antoinette J Taylor, and Richard D Averitt. Active terahertz metamaterial devices. *Nature*, 444(November):597–600, 2006. doi: 10.1038/nature05343. 9, 50, 66

[33] Hou-tong Chen, John F O’Hara, Abul K Azad, Antoinette J Taylor, Richard D Averitt, David B Shrekenhamer, and Willie J Padilla. Experimental demonstration of frequency-agile terahertz metamaterials. *Nature Photonics*, 2:295–298, 2008. doi: 10.1038/nphoton.2008.52. 10, 50, 66

[34] K R Catchpole and A Polman. Design principles for particle plasmon enhanced solar cells. *Applied Physics Letters*, 93(19):191113, 2008. doi: 10.1063/1.3021072. URL <http://link.aip.org/link/?APL/93/191113/1>. 14

[35] S Pillai, K R Catchpole, T Trupke, and M A Green. Surface plasmon enhanced silicon solar cells. *Journal of Applied Physics*, 101(9):93105, 2007. doi: 10.1063/1.2734885. URL <http://link.aip.org/link/?JAP/101/093105/1>. 14

[36] K R Catchpole and S Pillai. Absorption enhancement due to scattering by dipoles into silicon waveguides. *Journal of Applied Physics*, 100(4):44504, 2006. doi: 10.1063/1.2226334. URL <http://link.aip.org/link/?JAP/100/044504/1>. 14

[37] S Pillai, K R Catchpole, T Trupke, G Zhang, J Zhao, and M A Green. Enhanced emission from Si-based light-emitting diodes using surface plasmons. *Applied Physics Letters*, 88(16):161102, 2006. doi: 10.1063/1.2195695. URL <http://link.aip.org/link/?APL/88/161102/1>. 14

[38] D Derkacs, S H Lim, P Matheu, W Mar, and E T Yu. Improved performance of amorphous silicon solar cells via scattering from surface plasmon polaritons in nearby metallic nanoparticles. *Applied Physics Letters*, 89(9):093103, 2006. doi: 10.1063/1.2336629. URL <http://link.aip.org/link/?APL/89/093103/1>. 14

[39] Vivian E Ferry, Luke A Sweatlock, Domenico Pacifici, and Harry A Atwater. Plasmonic nanostructure design for efficient light coupling into solar cells. *Nano Letters*, 8(12):4391–7, December 2008. ISSN 1530-6984. URL <http://www.ncbi.nlm.nih.gov/pubmed/19367883>. 14, 25

[40] Howard R Stuart and Dennis G Hall. Island size effects in nanoparticle-enhanced photodetectors. *Applied Physics Letters*, 73(26):3815–3817, 1998. doi: 10.1063/1.122903. URL <http://link.aip.org/link/?APL/73/3815/1>. 14

[41] Keisuke Nakayama, Katsuaki Tanabe, and Harry A Atwater. Plasmonic nanoparticle enhanced light absorption in GaAs solar cells. *Applied Physics Letters*, 93(12):121904, 2008. doi: 10.1063/1.2988288. URL <http://link.aip.org/link/?APL/93/121904/1>. 14, 17, 131

[42] Patrick Campbell and Martin A Green. Light trapping properties of pyramidal textured surfaces. *Journal of Applied Physics*, 62(1):243–249, 1987. doi: 10.1063/1.339189. URL <http://link.aip.org/link/?JAP/62/243/1>. 14

[43] J Wu. Universal bandgap bowing in group-III nitride alloys. *Solid State Communications*, 127(6):411–414, August 2003. ISSN 00381098. doi: 10.1016/S0038-1098(03)00457-5. URL <http://linkinghub.elsevier.com/retrieve/pii/S0038109803004575>. 15

[44] J Wu, W Walukiewicz, K M Yu, W Shan, III Ager, J W, E E Haller, Hai Lu, William J Schaff, W K Metzger, and Sarah Kurtz. Superior radiation resistance of In_{1-x}Ga_xN alloys: Full-solar-spectrum photovoltaic material system. *Journal of Applied Physics*, 94(10):6477–6482, 2003. doi: 10.1063/1.1618353. URL <http://link.aip.org/link/?JAP/94/6477/1>. 15, 16

[45] X. Chen, K. D. Matthews, D. Hao, W. J. Schaff, and L. F. Eastman. Growth, fabrication, and characterization of InGaN solar cells. *Physica Status Solidi (a)*, 205(5):1103–1105, May 2008. ISSN 18626300. doi: 10.1002/pssa.200778695. URL <http://doi.wiley.com/10.1002/pssa.200778695>. 16

[46] Omkar Jani, Ian Ferguson, Christiana Honsberg, and Sarah Kurtz. Design and characterization of GaNInGaN solar cells. *Applied Physics Letters*, 91(13):132117, 2007. ISSN 00036951. doi: 10.1063/1.2793180. URL <http://link.aip.org/link/APPLAB/v91/i13/p132117/s1&Agg=doi>. 16

[47] Ray-Hua Horng, Shih-Ting Lin, Yu-Li Tsai, Mu-Tao Chu, Wen-Yih Liao, Ming-Hsien Wu, Ray-Ming Lin, and Yuan-Chieh Lu. Improved Conversion Efficiency of GaN/InGaN Thin-Film Solar Cells. *IEEE Electron Device Letters*, 30(7):724–726, January 2009. ISSN 1361-6528. doi: 10.1109/LED.2009.2021414. 16

[48] A. C. Schmitz, A. T. Ping, M. Asif Khan, Q. Chen, J. W. Yang, and I. Adesida. Metal contacts to n-type GaN. *Journal of Electronic Materials*, 27(4):255–260, April 1998. ISSN 0361-5235. doi: 10.1007/s11664-998-0396-5. URL <http://www.springerlink.com/index/10.1007/s11664-998-0396-5>. 23, 24

[49] Yow-Jon Lin. Nonalloyed Ohmic Formation for p-Type AlGaN with p-Type GaN Capping Layers Using Ohmic Recessed Technique. *Japanese Journal of Applied Physics*, 45(No. 3):L86–L88, January 2006. ISSN 0021-4922. doi: 10.1143/JJAP.45.L86. URL <http://jjap.ipap.jp/link?JJAP/45/L86/>. 23

[50] Vivian E Ferry, Marc A Verschuuren, Hongbo B T Li, Ewold Verhagen, Robert J Walters, Ruud E I Schropp, Harry A Atwater, and Albert Polman. Light trapping in ultrathin plasmonic solar cells. *Optics Express*, 18 Suppl 2(102):A237–45, June 2010. ISSN 1094-4087. URL <http://www.ncbi.nlm.nih.gov/pubmed/20588593>. 25

[51] E Prodan, C Radloff, N J Halas, and P Nordlander. A hybridization model for the plasmon response of complex nanostructures. *Science (New York, N.Y.)*, 302(5644):419–22, October 2003. ISSN 1095-9203. doi: 10.1126/science.1089171. URL <http://www.ncbi.nlm.nih.gov/pubmed/14564001>. 33

[52] Hui Wang, Yanpeng Wu, Britt Lassiter, Colleen L Nehl, Jason H Hafner, Peter Nordlander, and Naomi J Halas. Symmetry breaking in individual plasmonic nanoparticles. *Proceedings of the National Academy of Sciences of the United States of America*, 103(29):10856–60, July 2006. ISSN 0027-8424. doi: 10.1073/pnas.0604003103. URL <http://www.ncbi.nlm.nih.gov/pmc/articles/PMC1544138/>. 33

[53] V. Fedotov, M. Rose, S. Prosvirnin, N. Papasimakis, and N. Zheludev. Sharp Trapped-Mode Resonances in Planar Metamaterials with a Broken Structural Symmetry. *Physical Review Letters*, 99(14):5–8, October 2007. ISSN 0031-9007. doi: 10.1103/PhysRevLett.99.147401. URL <http://link.aps.org/doi/10.1103/PhysRevLett.99.147401>. 33, 40, 60, 82

[54] Basudev Lahiri, Ali Z Khokhar, Richard M De La Rue, Scott G McMeekin, and Nigel P Johnson. Asymmetric split ring resonators for optical sensing of organic materials. *Optics Express*, 17(2):1107–15, January 2009. ISSN 1094-4087. URL <http://www.ncbi.nlm.nih.gov/pubmed/19158928>. 33

[55] Ranjan Singh, Carsten Rockstuhl, Falk Lederer, and Weili Zhang. Coupling between a dark and a bright eigenmode in a terahertz metamaterial. *Physical Review B*, 79(8):1–4, February 2009. ISSN 1098-0121. doi: 10.1103/PhysRevB.79.085111. URL <http://link.aps.org/doi/10.1103/PhysRevB.79.085111>. 33

[56] Niels Verellen, Yannick Sonnefraud, Heidar Sobhani, Feng Hao, Victor V Moshchalkov, Pol Van Dorpe, Peter Nordlander, and Stefan A Maier. Fano resonances in individual coherent plasmonic nanocavities. *Nano Letters*, 9(4):1663–7, April 2009. ISSN 1530-6992. doi: 10.1021/nl9001876. URL <http://www.ncbi.nlm.nih.gov/pubmed/19281254>. 33, 67, 85

[57] Shuang Zhang, Dentcho Genov, Yuan Wang, Ming Liu, and Xiang Zhang. Plasmon-Induced Transparency in Metamaterials. *Physical Review Letters*, 101(4):1–4, July 2008. ISSN 0031-9007. doi: 10.1103/PhysRevLett.101.047401. URL <http://link.aps.org/doi/10.1103/PhysRevLett.101.047401>. 33, 50, 67, 85

[58] Feng Hao, Yannick Sonnefraud, Pol Van Dorpe, Stefan A. Maier, Naomi J. Halas, and Peter Nordlander. Symmetry breaking in plasmonic nanocavities: subradiant LSPR sensing and a tunable Fano resonance. *Nano Letters*, 8(11):

3983–3988, November 2008. ISSN 1530-6984. doi: 10.1021/nl802509r. URL <http://www.ncbi.nlm.nih.gov/pubmed/18831572>. 33, 94

[59] P. Tassin, Lei Zhang, Th. Koschny, E. Economou, and C. Soukoulis. Low-Loss Metamaterials Based on Classical Electromagnetically Induced Transparency. *Physical Review Letters*, 102(5):6–9, February 2009. ISSN 0031-9007. doi: 10.1103/PhysRevLett.102.053901. URL <http://link.aps.org/doi/10.1103/PhysRevLett.102.053901>. 34

[60] N. Papasimakis, V. Fedotov, N. Zheludev, and S. Prosvirnin. Metamaterial Analog of Electromagnetically Induced Transparency. *Physical Review Letters*, 101(25):2–5, December 2008. ISSN 0031-9007. doi: 10.1103/PhysRevLett.101.253903. URL <http://link.aps.org/doi/10.1103/PhysRevLett.101.253903>. 34

[61] Na Liu, Lutz Langguth, Thomas Weiss, Jürgen Kästel, Michael Fleischhauer, Tilman Pfau, and Harald Giessen. Plasmonic analogue of electromagnetically induced transparency at the Drude damping limit. *Nature Materials*, 8(9):758–62, September 2009. ISSN 1476-1122. doi: 10.1038/nmat2495. URL <http://www.ncbi.nlm.nih.gov/pubmed/19578334>. 34, 85, 94

[62] Hongcang Guo, Na Liu, Liwei Fu, Todd P Meyrath, Thomas Zentgraf, Heinz Schweizer, and Harald Giessen. Resonance hybridization in double split-ring resonator metamaterials. *Optics Express*, 15(19):12095–12101, September 2007. ISSN 1094-4087. URL <http://www.ncbi.nlm.nih.gov/pubmed/19547574>. 42, 45, 62

[63] R A Shelby, D R Smith, and S Schultz. Experimental verification of a negative index of refraction. *Science*, 292(5514):77–79, April 2001. ISSN 0036-8075. doi: 10.1126/science.1058847. URL <http://www.ncbi.nlm.nih.gov/pubmed/11292865>. 50

[64] Hou-tong Chen, Willie J Padilla, Michael J Cich, Abul K Azad, Richard D Averitt, and Antoinette J Taylor. A metamaterial solid-state terahertz

phase modulator. *Nature Photonics*, 3(March):148–151, 2009. doi: 10.1038/NPHOTON.2009.3. 50

[65] T. Driscoll, S. Palit, M. M. Qazilbash, M. Brehm, F. Keilmann, Byung-Gyu Chae, Sun-Jin Yun, Hyun-Tak Kim, S. Y. Cho, N. Marie Jokerst, D. R. Smith, and D. N. Basov. Dynamic tuning of an infrared hybrid-metamaterial resonance using vanadium dioxide. *Applied Physics Letters*, 93(2):024101, 2008. ISSN 00036951. doi: 10.1063/1.2956675. URL <http://link.aip.org/link/APPLAB/v93/i2/p024101/s1&Agg=doi>. 50, 51

[66] J Goodenough. The two components of the crystallographic transition in VO₂. *Journal of Solid State Chemistry*, 3(4):490–500, November 1971. ISSN 00224596. doi: 10.1016/0022-4596(71)90091-0. URL <http://linkinghub.elsevier.com/retrieve/pii/0022459671900910>. 50

[67] F. J. Morin. Oxides which show a metal-to-insulator transition at the Neel temperature. *Physical Review Letters*, 3(1):34–36, 1959. 50

[68] A. Cavalleri, Th. Dekorsy, H. H. W. Chong, J. C. Kieffer, and R. W. Schoenlein. Evidence for a structurally-driven insulator-to-metal transition in VO₂: A view from the ultrafast timescale. *Physical Review B*, 70(16):161102(R), October 2004. ISSN 1098-0121. doi: 10.1103/PhysRevB.70.161102. URL <http://link.aps.org/doi/10.1103/PhysRevB.70.161102>. 50

[69] A. Cavalleri, Cs. Tóth, C. Siders, J. Squier, F. Ráksi, P. Forget, and J. Kieffer. Femtosecond Structural Dynamics in VO₂ during an Ultrafast Solid-Solid Phase Transition. *Physical Review Letters*, 87(23):237401, November 2001. ISSN 0031-9007. doi: 10.1103/PhysRevLett.87.237401. URL <http://link.aps.org/doi/10.1103/PhysRevLett.87.237401>. 50

[70] G. Stefanovich, A. Pergament, and D. Stefanovich. Electrical switching and Mott transition in VO₂. *J. Phys.: Condens. Matter*, 12:8837–3345, 2000. 50

[71] R. Lopez, L. C. Feldman, and R. Haglund. Size-Dependent Optical Properties of VO₂ Nanoparticle Arrays. *Physical Review Letters*, 93(17):177403, October 2004. ISSN 0031-9007. doi: 10.1103/PhysRevLett.93.177403. URL <http://link.aps.org/doi/10.1103/PhysRevLett.93.177403>. 51, 57

[72] Eugenii U Donev, Rene Lopez, Leonard C Feldman, and Richard F Haglund. Confocal Raman microscopy across the metal-insulator transition of single vanadium dioxide nanoparticles. *Nano Letters*, 9(2):702–706, February 2009. ISSN 1530-6984. doi: 10.1021/nl8031839. URL <http://www.ncbi.nlm.nih.gov/pubmed/19199760>. 51

[73] J. Y. Suh, E. U. Donev, R. Lopez, L. C. Feldman, and R. F. Haglund. Modulated optical transmission of subwavelength hole arrays in metal-VO₂ films. *Applied Physics Letters*, 88(13):133115, 2006. ISSN 00036951. doi: 10.1063/1.2190463. URL <http://link.aip.org/link/APPLAB/v88/i13/p133115/s1&Agg=doi>. 51

[74] M M Qazilbash, M Brehm, Byung-Gyu Chae, P-C Ho, G O Andreev, Bong-Jun Kim, Sun Jin Yun, A V Balatsky, M B Maple, F Keilmann, Hyun-Tak Kim, and D N Basov. Mott transition in VO₂ revealed by infrared spectroscopy and nano-imaging. *Science*, 318(5857):1750–1753, December 2007. ISSN 1095-9203. doi: 10.1126/science.1150124. URL <http://www.ncbi.nlm.nih.gov/pubmed/18079396>. 57

[75] Ryan M Briggs, Imogen M Pryce, and Harry A Atwater. Compact silicon photonic waveguide modulator based on the vanadium dioxide metal-insulator phase transition. *Optics Express*, 18(11):11192–201, May 2010. ISSN 1094-4087. URL <http://www.ncbi.nlm.nih.gov/pubmed/20588978>. 64

[76] A. V. Rogacheva, V. A. Fedotov, A. S. Schwancke, and N. I. Zheludev. Giant Gyrotropy due to Electromagnetic-Field Coupling in a Bilayered Chiral Structure. *Physical Review Letters*, 97(17):1–4, October 2006. ISSN 0031-9007. doi:

10.1103/PhysRevLett.97.177401. URL <http://link.aps.org/doi/10.1103/PhysRevLett.97.177401>. 66

[77] Justyna K Gansel, Michael Thiel, Michael S Rill, Manuel Decker, Klaus Bade, Volker Saile, Georg von Freymann, Stefan Linden, and Martin Wegener. Gold helix photonic metamaterial as broadband circular polarizer. *Science (New York, N.Y.)*, 325(5947):1513–5, September 2009. ISSN 1095-9203. doi: 10.1126/science.1177031. URL <http://www.ncbi.nlm.nih.gov/pubmed/19696310>. 66

[78] Hu Tao, A C Strikwerda, K Fan, W J Padilla, X Zhang, and R D Averitt. Reconfigurable Terahertz Metamaterials. *Phys Rev Lett*, 147401(OCTOBER):1–4, 2009. doi: 10.1103/PhysRevLett.103.147401. 66

[79] Z. L. Samson, K. F. MacDonald, F. De Angelis, B. Gholipour, K. Knight, C. C. Huang, E. Di Fabrizio, D. W. Hewak, and N. I. Zheludev. Metamaterial electro-optic switch of nanoscale thickness. *Applied Physics Letters*, 96(14):143105, 2010. ISSN 00036951. doi: 10.1063/1.3355544. URL <http://link.aip.org/link/APPLAB/v96/i14/p143105/s1&Agg=doi>. 66

[80] John a Rogers, Takao Someya, and Yonggang Huang. Materials and mechanics for stretchable electronics. *Science (New York, N.Y.)*, 327(5973):1603–7, March 2010. ISSN 1095-9203. doi: 10.1126/science.1182383. URL <http://www.ncbi.nlm.nih.gov/pubmed/20339064>. 66

[81] Fumin Huang and Jeremy J Baumberg. Actively tuned plasmons on elastomerically driven Au nanoparticle dimers. *Nano Letters*, 10(5):1787–92, May 2010. ISSN 1530-6992. doi: 10.1021/nl1004114. URL <http://www.ncbi.nlm.nih.gov/pubmed/20408552>. 66, 95

[82] Selim Olcum, Askin Kocabas, Gulay Ertas, Abdullah Atalar, and Atilla Aydinli. Tunable surface plasmon resonance on an elastomeric substrate. *Optics Express*, 17(10):8542–7, May 2009. ISSN 1094-4087. URL <http://www.ncbi.nlm.nih.gov/pubmed/19434187>. 66

[83] Rohat Melik, Emre Unal, Nihan Kosku Perkgoz, Christian Puttlitz, and Hilmi Volkan Demir. Flexible metamaterials for wireless strain sensing. *Applied Physics Letters*, 95(18):181105, 2009. ISSN 00036951. doi: 10.1063/1.3250175. URL <http://link.aip.org/link/APPLAB/v95/i18/p181105/s1&Agg=doi>. 67

[84] Hu Tao, C. Bingham, a. Strikwerda, D. Pilon, D. Shrekenhamer, N. Landy, K. Fan, X. Zhang, W. Padilla, and R. Averitt. Highly flexible wide angle of incidence terahertz metamaterial absorber: Design, fabrication, and characterization. *Physical Review B*, 78(24):2–5, December 2008. ISSN 1098-0121. doi: 10.1103/PhysRevB.78.241103. URL <http://link.aps.org/doi/10.1103/PhysRevB.78.241103>. 67

[85] Hu Tao, A. C. Strikwerda, K. Fan, C. M. Bingham, W. J. Padilla, Xin Zhang, and R. D. Averitt. Terahertz metamaterials on free-standing highly-flexible polyimide substrates. *Journal of Physics D: Applied Physics*, 41(23):232004, December 2008. ISSN 0022-3727. doi: 10.1088/0022-3727/41/23/232004. URL <http://stacks.iop.org/0022-3727/41/i=23/a=232004?key=crossref.14a5760411cb9ab2427ef46d614b80b8>. 67

[86] J. A. Fan, C. Wu, K. Bao, J. Bao, R. Bardhan, N. J. Halas, V. N. Manoharan, P. Nordlander, G. Shvets, and F. Capasso. Self-Assembled Plasmonic Nanoparticle Clusters. *Science*, 328(5982):1135–1138, May 2010. ISSN 0036-8075. doi: 10.1126/science.1187949. URL <http://www.sciencemag.org/cgi/doi/10.1126/science.1187949>. 67, 85

[87] Yannick Sonnenaud, Niels Verellen, Heidar Sobhani, Guy A E Vandenbosch, Victor V Moshchalkov, Pol Van Dorpe, Peter Nordlander, and Stefan A Maier. Experimental realization of subradiant, superradiant, and fano resonances in ring/disk plasmonic nanocavities. *ACS Nano*, 4(3):1664–70, March 2010. ISSN 1936-086X. doi: 10.1021/nn901580r. URL <http://www.ncbi.nlm.nih.gov/pubmed/20155967>. 67, 85

[88] Koray Aydin, Imogen M Pryce, and Harry A Atwater. Symmetry breaking and strong coupling in planar optical metamaterials. *Optics Express*, 18(13):13407–17, June 2010. ISSN 1094-4087. URL <http://www.ncbi.nlm.nih.gov/pubmed/20588471>. 67, 75, 94, 97

[89] Ivana Sersic, Martin Frimmer, Ewold Verhagen, and A. Femius Koenderink. Electric and Magnetic Dipole Coupling in Near-Infrared Split-Ring Metamaterial Arrays. *Physical Review Letters*, 103(21):1–4, November 2009. ISSN 0031-9007. doi: 10.1103/PhysRevLett.103.213902. URL <http://link.aps.org/doi/10.1103/PhysRevLett.103.213902>. 67

[90] Na Liu, Hongcang Guo, Liwei Fu, Heinz Schweizer, Stefan Kaiser, and Harald Giessen. Electromagnetic resonances in single and double split-ring resonator metamaterials in the near infrared spectral region. *Physica Status Solidi (B)*, 244(4):1251–1255, April 2007. ISSN 03701972. doi: 10.1002/pssb.200674514. URL <http://doi.wiley.com/10.1002/pssb.200674514>. 80

[91] Rostislav Bukasov and Jennifer S Shumaker-Parry. Silver nanocrescents with infrared plasmonic properties as tunable substrates for surface enhanced infrared absorption spectroscopy. *Analytical Chemistry*, 81(11):4531–5, June 2009. ISSN 1520-6882. doi: 10.1021/ac900477p. URL <http://www.ncbi.nlm.nih.gov/pubmed/19408957>. 82, 93, 94, 108

[92] T. R. Jensen, R. P. Van Duyne, S. A. Johnson, and V. A. Maroni. Surface-Enhanced Infrared Spectroscopy: A Comparison of Metal Island Films with Discrete and Nondiscrete Surface Plasmons. *Applied Spectroscopy*, 54(3):371–377, March 2000. ISSN 00037028. doi: 10.1366/0003702001949654. URL <http://openurl.ingenta.com/content/xref?genre=article&issn=0003-7028&volume=54&issue=3&spage=371>. 82, 94

[93] Janardan Kundu, Fei Le, Peter Nordlander, and Naomi J. Halas. Surface enhanced infrared absorption (SEIRA) spectroscopy on nanoshell aggregate substrates. *Chemical Physics Letters*, 452(1-3):115–119, February 2008.

ISSN 00092614. doi: 10.1016/j.cplett.2007.12.042. URL <http://linkinghub.elsevier.com/retrieve/pii/S0009261407016533>. 82, 94, 107, 108

[94] Fei Le, Daniel W Brandl, Yaroslav A. Urzhumov, Hui Wang, Janardan Kundu, Naomi J. Halas, Javier Aizpurua, and Peter Nordlander. Metallic nanoparticle arrays: a common substrate for both surface-enhanced Raman scattering and surface-enhanced infrared absorption. *ACS Nano*, 2(4):707–18, April 2008. ISSN 1936-086X. doi: 10.1021/nn800047e. URL <http://www.ncbi.nlm.nih.gov/pubmed/19206602>. 82, 94

[95] Hui Wang, Janardan Kundu, and Naomi J. Halas. Plasmonic nanoshell arrays combine surface-enhanced vibrational spectroscopies on a single substrate. *Angewandte Chemie (International ed. in English)*, 46(47):9040–4, January 2007. ISSN 1521-3773. doi: 10.1002/anie.200702072. URL <http://www.ncbi.nlm.nih.gov/pubmed/17957664>. 82, 94

[96] Surbhi Lal, Nathaniel K Grady, Janardan Kundu, Carly S. Levin, J. Britt Las-siter, and Naomi J. Halas. Tailoring plasmonic substrates for surface enhanced spectroscopies. *Chemical Society Reviews*, 37(5):898–911, May 2008. ISSN 0306-0012. doi: 10.1039/b705969h. URL <http://www.ncbi.nlm.nih.gov/pubmed/18443675>. 82, 93, 94

[97] Ertugrul Cubukcu, Shuang Zhang, Yong-Shik Park, Guy Bartal, and Xiang Zhang. Split ring resonator sensors for infrared detection of single molecular monolayers. *Applied Physics Letters*, 95(4):043113, 2009. ISSN 00036951. doi: 10.1063/1.3194154. URL <http://link.aip.org/link/APPLAB/v95/i4/p043113/s1&Agg=doi>. 82, 94, 95

[98] Frank Neubrech, Annemarie Pucci, Thomas Cornelius, Shafqat Karim, Aitzol García-Etxarri, and Javier Aizpurua. Resonant Plasmonic and Vibrational Coupling in a Tailored Nanoantenna for Infrared Detection. *Physical Review Letters*, 101(15):2–5, October 2008. ISSN 0031-9007. doi:

10.1103/PhysRevLett.101.157403. URL <http://link.aps.org/doi/10.1103/PhysRevLett.101.157403>. 82, 94

[99] A. Lee Smith and Dennis R. Anderson. Vibrational Spectra of Me₂SiCl₂, Me₃SiCl, Me₃SiOSiMe₃, (Me₂SiO)₃,(Me₂SiO)₄,(Me₂SiO)_x, and Their Deuterated Analogs. *Applied Spectroscopy*, 38(6):822–834, 1984. 83

[100] Rostislav Bukasov, Tamer A. Ali, Peter Nordlander, and Jennifer S. Shumaker-Parry. Probing the plasmonic near-field of gold nanocrescent antennas. *ACS Nano*, 4(11):6639–6650, November 2010. ISSN 1936-086X. doi: 10.1021/nn101994t. URL <http://www.ncbi.nlm.nih.gov/pubmed/21038885>. 93

[101] Zheng-Gao Dong, Hui Liu, Jing-Xiao Cao, Tao Li, Shu-Ming Wang, Shi-Ning Zhu, and X. Zhang. Enhanced sensing performance by the plasmonic analog of electromagnetically induced transparency in active metamaterials. *Applied Physics Letters*, 97(11):114101, 2010. ISSN 00036951. doi: 10.1063/1.3488020. URL <http://link.aip.org/link/APPLAB/v97/i11/p114101/s1&Agg=doi>. 94

[102] Adam D. McFarland and Richard P. Van Duyne. Single Silver Nanoparticles as Real-Time Optical Sensors with Zeptomole Sensitivity. *Nano Letters*, 3(8):1057–1062, August 2003. ISSN 1530-6984. doi: 10.1021/nl034372s. URL <http://pubs.acs.org/doi/abs/10.1021/nl034372s>. 94

[103] Colleen L. Nehl, Hongwei Liao, and Jason H Hafner. Optical properties of star-shaped gold nanoparticles. *Nano Letters*, 6(4):683–8, April 2006. ISSN 1530-6984. doi: 10.1021/nl052409y. URL <http://www.ncbi.nlm.nih.gov/pubmed/16608264>. 94

[104] Sylvia Underwood and Paul Mulvaney. Effect of the Solution Refractive Index on the Color of Gold Colloids. *Langmuir*, 10(10):3427–3430, October 1994. ISSN 0743-7463. doi: 10.1021/la00022a011. URL <http://pubs.acs.org/doi/abs/10.1021/la00022a011>. 94

[105] Felicia Tam, Cristin Moran, and Naomi Halas. Geometrical Parameters Controlling Sensitivity of Nanoshell Plasmon Resonances to Changes in Dielectric Environment. *The Journal of Physical Chemistry B*, 108(45):17290–17294, November 2004. ISSN 1520-6106. doi: 10.1021/jp048499x. URL <http://pubs.acs.org/doi/abs/10.1021/jp048499x>. 94

[106] Feng Hao, Peter Nordlander, Yannick Sonnefraud, Pol Van Dorpe, and Stefan A Maier. Tunability of subradiant dipolar and fano-type plasmon resonances in metallic ring/disk cavities: implications for nanoscale optical sensing. *ACS Nano*, 3(3):643–52, March 2009. ISSN 1936-086X. doi: 10.1021/nn900012r. URL <http://www.ncbi.nlm.nih.gov/pubmed/19309172>. 94

[107] Wakana Kubo and Shigenori Fujikawa. Au Double Nanopillars with Nanogap for Plasmonic Sensor. *Nano Letters*, 11:8–15, November 2011. ISSN 1530-6992. doi: 10.1021/nl100787b. URL <http://www.ncbi.nlm.nih.gov/pubmed/21114297>. 94, 101

[108] J P Kottmann, O J Martin, D R Smith, and S Schultz. Non-regularly shaped plasmon resonant nanoparticle as localized light source for near-field microscopy. *Journal of microscopy*, 202(Pt 1):60–5, April 2001. ISSN 0022-2720. URL <http://www.ncbi.nlm.nih.gov/pubmed/11298871>. 94

[109] T. Klar, M. Perner, S. Grosse, G. von Plessen, W. Spirk, and J. Feldmann. Surface-Plasmon Resonances in Single Metallic Nanoparticles. *Physical Review Letters*, 80(19):4249–4252, May 1998. ISSN 0031-9007. doi: 10.1103/PhysRevLett.80.4249. URL <http://link.aps.org/doi/10.1103/PhysRevLett.80.4249>. 94

[110] Masatoshi Osawa, Ken-Ichi Ataka, Katsumasa Yoshii, and Yuji Nishikawa. Surface-Enhanced Infrared Spectroscopy: The Origin of the Absorption Enhancement and Band Selection Rule in the Infrared Spectra of Molecules Adsorbed on Fine Metal Particles. *Applied Spectroscopy*, 47(9):1497–1502, 1993. 94

[111] Shuming Nie and Steven R. Emory. Probing Single Molecules and Single Nanoparticles by Surface-Enhanced Raman Scattering. *Science*, 275(5303):1102–1106, February 1997. ISSN 00368075. doi: 10.1126/science.275.5303.1102. URL <http://www.sciencemag.org/cgi/doi/10.1126/science.275.5303.1102>. 94

[112] Hongxing Xu, Erik Bjerneld, Mikael Käll, and Lars Börjesson. Spectroscopy of Single Hemoglobin Molecules by Surface Enhanced Raman Scattering. *Physical Review Letters*, 83(21):4357–4360, November 1999. ISSN 0031-9007. doi: 10.1103/PhysRevLett.83.4357. URL <http://link.aps.org/doi/10.1103/PhysRevLett.83.4357>. 94

[113] Katrin Kneipp, Yang Wang, Harald Kneipp, Lev Perelman, Irving Itzkan, Ramachandra Dasari, and Michael Feld. Single Molecule Detection Using Surface-Enhanced Raman Scattering (SERS). *Physical Review Letters*, 78(9):1667–1670, March 1997. ISSN 0031-9007. doi: 10.1103/PhysRevLett.78.1667. URL <http://link.aps.org/doi/10.1103/PhysRevLett.78.1667>. 94

[114] Imogen M. Pryce, Koray Aydin, Yousif A. Kelaita, Ryan M. Briggs, and Harry A. Atwater. Highly Strained Compliant Optical Metamaterials with Large Frequency Tunability. *Nano Letters*, 10(10):4222–4227, September 2010. ISSN 1530-6984. doi: 10.1021/nl102684x. URL <http://pubs.acs.org/doi/abs/10.1021/nl102684x>. 95, 97, 109

[115] Leif J. Sherry, Rongchao Jin, Chad A. Mirkin, George C. Schatz, and Richard P. Van Duyne. Localized surface plasmon resonance spectroscopy of single silver triangular nanoprisms. *Nano Letters*, 6(9):2060–5, September 2006. ISSN 1530-6984. doi: 10.1021/nl061286u. URL <http://www.ncbi.nlm.nih.gov/pubmed/16968025>. 100

[116] Nobuyuki Mohri, Satoru Matsushita, Morimasa Inoue, and Kenichi Yoshikawa. Desorption of 4-Aminobenzenethiol Bound to a Gold Surface. *Langmuir*, 14

(9):2343–2347, April 1998. ISSN 0743-7463. doi: 10.1021/la9707639. URL <http://pubs.acs.org/doi/abs/10.1021/la9707639>. 108

[117] Amit Kumar and George M. Whitesides. Features of gold having micrometer to centimeter dimensions can be formed through a combination of stamping with an elastomeric stamp and an alkanethiol ink followed by chemical etching. *Applied Physics Letters*, 63(14):2002, 1993. ISSN 00036951. doi: 10.1063/1.110628. URL <http://link.aip.org/link/APPLAB/v63/i14/p2002/s1&Agg=doi.111>